



Klitis, Charalambos (2018) *Polarisation selective integrated silicon photonic devices*. PhD thesis.

<http://theses.gla.ac.uk/8725/>

Copyright and moral rights for this work are retained by the author

A copy can be downloaded for personal non-commercial research or study, without prior permission or charge

This work cannot be reproduced or quoted extensively from without first obtaining permission in writing from the author

The content must not be changed in any way or sold commercially in any format or medium without the formal permission of the author

When referring to this work, full bibliographic details including the author, title, awarding institution and date of the thesis must be given

Enlighten:Theses
<http://theses.gla.ac.uk/>
theses@ gla.ac.uk



University
of Glasgow

UNIVERSITY OF GLASGOW

Polarisation Selective Integrated silicon photonic devices

by

Charalambos Klitis

A thesis submitted in partial fulfilment for the
degree of Doctor of Philosophy

in the

Electronic and Nanoscale Engineering
School of Engineering

February 2018

Declaration of Authorship

I, Charalambos Klitis, declare that this thesis titled, ‘Polarisation Selective Integrated silicon photonic devices’ and the work presented in it are my own. I confirm that:

- This work was done wholly or mainly while in candidature for a research degree at this University.
- Where any part of this thesis has previously been submitted for a degree or any other qualification at this University or any other institution, this has been clearly stated.
- Where I have consulted the published work of others, this is always clearly attributed.
- Where I have quoted from the work of others, the source is always given. With the exception of such quotations, this thesis is entirely my own work.
- I have acknowledged all main sources of help.
- Where the thesis is based on work done by myself jointly with others, I have made clear exactly what was done by others and what I have contributed myself.

Signed:

Date:

"If we knew what we were doing, it wouldn't be called research."

Albert Einstein

Abstract

The main objective of this thesis was the development of polarisation selective gratings in silicon-on-insulator (SOI) technology. These devices can find numerous applications in the design of highly performing optical filters and, more in general, in all those devices that require on-chip manipulation of the polarisation state. The development of these devices was preceded by the optimisation of several fabrication processes, such as lithography and dry etching, and the re-design of a number of key components such as inverse polymer tapers and metallic heaters for thermal tuning. This activity culminated into a very robust process flow for SOI devices, with repeatable propagation losses in the order of 1 dB/cm, heaters with a very high tuning efficiency of 12 mW per π phase shift and 2dB and 1dB waveguide-to-optical fibre coupling losses for the TE and TM polarised mode, respectively. The grating designs developed in this thesis consisted of periodic holes etched onto the top surface of the silicon optical waveguide. Such geometry overlaps strongly with the TM polarised mode only and does not introduce additional losses to the TE mode. The benefit and the additional functionalities provided by the top grating geometry was assessed on two different polarisation sensitive devices. The first consisted in a microring resonator with integrated gratings for the emission of optical vortex beams, for which the top gratings provided a route to engineer the polarisation state of the emitted beam. The second device was a Bragg grating filter, where the top grating allowed the demonstration of extinction ratio values as high as 60dB by filtering the residual TM mode generated by the strong polarisation scattering.

Acknowledgements

First and foremost, I will like to thank my supervisor, Prof. Marc Sorel, for having believed and invested in me from the start, for his great support during my PhD and his informal and friendly approach. His continuous suggestions, advice, and psychological support during these four years constituted an immeasurable value for me.

The EPSRC for funding this PhD project and the European projects BBOI and ROAM which under part of this work has taken place.

Thanks to Dr Michael Strain and Dr Barry Holmes for the useful discussions and teaching over the years. Also thanks to Dr Laura Meriggi and Dr Antonio Samarelli, for the great help and training in the labs. All four have significantly helped me during this project, not only during working time but as friends as well.

To all the members, present and past, of the Optoelectronic Group who have shared with me the joys and pains of fabrication. Thanks, in order of appearance, to Graham, Christine, Stuart, Lourdes, Ross, George and Kleanthis.

To all the staff of the JWNC and Engineering Department for making the magic of fabrication possible and for creating the fantastic environment of a big family. Especially Dr Stephen Thomson and Dr William Ward for the continued help and support.

And last but not least, to my family and friends which make this possible. Without their continues mental support and help, this will be an impossible task to complete.

Contents

Declaration of Authorship	i
Abstract	iii
Acknowledgements	iv
Publications	ix
List of Figures	xiii
List of Tables	xviii
Abbreviations	xix
Physical Constants	xxii
Symbols	xxiii
1 Introduction	1
1.1 Silicon Photonics	1
1.2 Polarisation in silicon photonics	4
1.3 Motivation	7
1.4 Thesis outline	8
2 Fabrication	10
2.1 Material	11
2.2 Fabrication Process	13
2.3 Electron Beam Lithography (e-beam)	14
2.4 Resists	21
2.4.1 HSQ	22
2.4.2 ZEP-520A	25
2.4.3 PMMA	26
2.4.4 SU8	28

2.5	Dry Etching	29
2.5.1	Silicon dry etching	31
2.5.1.1	STS etching	31
2.5.1.2	Estrelas etching	33
2.5.2	PECVD Silica Deposition	37
2.5.3	ICP-CVD Silicon Nitride Deposition	38
2.6	Conclusion	38
3	Component Design	40
3.1	Thermal tuning of silicon devices	41
3.1.1	Introduction	41
3.1.2	Thermo-optic effects in silicon	41
3.1.3	Heater configuration	42
3.1.4	Upper cladding design	44
3.1.5	Heating element geometry	45
3.1.6	Mach Zehnder Interferometer (MZI) tuning	48
3.2	Inverse tapers couplers	50
3.2.1	Introduction	50
3.2.2	Polymer Waveguide Geometry	52
3.2.3	Inverse taper	54
3.2.4	Experimental data	56
3.3	Waveguide Geometries	59
3.3.1	Slot Waveguides	59
3.3.1.1	Effective Index and Phase matching	60
3.3.1.2	Taper design	62
3.3.2	Sub-wavelength waveguides	64
3.4	Conclusion	67
4	Polarisation Selective Filters	69
4.1	Introduction	69
4.2	Side-wall grating Bragg filters	70
4.2.1	Design	70
4.2.2	Experimental results	73
4.3	TM filter	76
4.3.1	Metallic TM filter	78
4.3.2	Top grating Bragg filters	79
4.3.2.1	Design	79
4.3.2.2	Experimental results	82
4.4	TE/TM Bragg filter	84
4.5	Conclusion	87
5	Optical Vortex Emitters with Arbitrary Polarisation	88
5.1	Introduction	89
5.1.1	Phase-matching condition	90
5.1.2	States of Polarisation of the emitted optical field	94

5.2	Device Design	94
5.3	Experimental work	96
5.3.1	Experimental set-up	97
5.3.2	Measurements	98
5.4	Conclusion	104
6	Conclusion	105
6.1	Fabrication techniques	105
6.2	Components Design	106
6.3	Polarisation selective devices	108
A	Origin and Extraction of Optical Losses	109
A.1	The origin of optical losses	109
A.1.1	Scattering Losses	109
A.1.2	Absorption Losses	110
A.1.3	Radiation Losses	111
A.2	Extraction of Propagation losses	111
A.2.1	Cut-back Technique	111
A.2.2	Fabry-Perot method	112
A.3	Optical set-up	112
B	Simulation Techniques	114
B.1	Solvers	114
	Finite-Difference Eigenmode (FDE)	114
	Beam Propagation Method (BPM)	115
	2/3D Finite-Difference Time-Domain (FDTD)	115
	2.5 FDTD (varFDTD)	116
	Eigenmode Expansion (EME)	116
	Finite Element Method (FEM)	117
B.2	Boundary conditions	118
	Perfectly matched layer (PML)	118
	Metal	118
	Periodic	118
	Bloch	118
	Perfect Magnetic Conductor (PMC)	118
	Symmetric / Anti-Symmetric	119
C	Silicon Waveguides for Second Harmonic Generation	120
C.1	Introduction	120
C.2	Non-Linear Optics	121
C.2.1	Second-Harmonic Generation	122
C.2.2	Straight waveguides	123

Bibliography

Publications

Journals

1. Charalambos Klitis, Giuseppe Cantarella, Michael J. Strain, and Marc Sorel, "High-extinction-ratio TE/TM selective Bragg grating filters on silicon-on-insulator", *Opt. Lett.* 42, 3040-3043 (2017)
2. Qingsheng Xiao, Charalambos Klitis, Shimao Li, Yueyang Chen, Xinlun Cai, Marc Sorel, and Siyuan Yu, "Generation of photonic orbital angular momentum superposition states using vortex beam emitters with superimposed gratings", *Opt. Express* 24, 3168-3176 (2016)
3. Jun Liu, Shimao Li, Jing Du, Charalambos Klitis, Cheng Du, Qi Mo, Marc Sorel, Siyuan Yu, Xinlun Cai, and Jian Wang, "Performance evaluation of analog signal transmission in an integrated optical vortex emitter to 3.6-km few-mode fiber system", *Opt. Lett.* 41, 1969-1972 (2016)
4. Mirco Scaffardi, Muhammad Nouman Malik, Emma Lazzeri, Gianluca Meloni, Francesco Fresi, Luca Pot, Nicola Andriolli, Isabella Cerutti, Charalambos Klitis, Laura Meriggi, Ning Zhang, Marc Sorel, and Antonella Bogoni, "A Silicon Microring Optical 2 x 2 Switch Exploiting Orbital Angular Momentum for Interconnection Networks up to 20 Gbaud", *J. Lightwave Technol.* 35, 3142-3148 (2017)
5. Stefano Grillanda, Ruiqiang Ji, Francesco Morichetti, Marco Carminati, Giorgio Ferrari, Emanuele Guglielmi, Nicola Peserico, Andrea Annoni, Alberto Ded, Danilo Nicolato, Antonello Vannucci, Charalambos Klitis, Barry

- Holmes, Marc Sorel, Shengmeng Fu, Jiangwei Man, Li Zeng, Marco Sampietro, and Andrea Melloni, "Wavelength Locking of Silicon Photonics Multiplexer for DML-Based WDM Transmitter", *J. Lightwave Technol.* 35, 607-614 (2017)
6. Giuseppe Cantarella, Charalambos Klitis, Marc Sorel, and Michael J. Strain, "Silicon photonic filters with high rejection of both TE and TM modes for on-chip four wave mixing applications", *Opt. Express* 25, 19711-19720 (2017)
 7. Mirco Scaffardi, Ning Zhang, Muhammad Nouman Malik, Emma Lazzeri, Charalambos Klitis, Martin Lavery, Marc Sorel, Antonella Bogoni, Interconnection network architectures based on integrated orbital angular momentum emitters, *Optics Communications*, September 2017
 8. Mirco Scaffardi, Muhammad N. Malik, Emma Lazzeri, Charalambos Klitis, Laura Meriggi, Ning Zhang, Marc Sorel, and Antonella Bogoni, "33 optical switch by exploiting vortex beam emitters based on silicon microrings with superimposed gratings", *Opt. Lett.* 42, 3749-3752 (2017)

Conferences

1. C. Klitis, G. Cantarella, M. J. Strain and M. Sorel, "Integrated TE/TM grating filters with high extinction ratio", 2016 Photonics North (PN), Quebec City, QC, 2016, pp. 1-1.
2. C. Klitis, G. Cantarella, M. J. Strain and M. Sorel, "Polarisation selective Bragg filters on silicon-on-insulator", 2015 11th Conference on Ph.D. Research in Microelectronics and Electronics (PRIME), Glasgow, 2015, pp. 353-356.
3. J. Liu et al., "Demonstration of few mode fiber transmission link seeded by a silicon photonic integrated optical vortex emitter", 2015 European Conference on Optical Communication (ECOC), Valencia, 2015, pp. 1-3.
4. F. Morichetti et al., "Electrochemical optical actuators: Controlling the light through ions", 2016 18th International Conference on Transparent Optical Networks (ICTON), Trento, 2016, pp. 1-4.

5. S. Grillanda et al., "Wavelength locking platform for DML-based multichannel transmitter on a silicon chip", 2016 Optical Fiber Communications Conference and Exhibition (OFC), Anaheim, CA, 2016, pp. 1-3.
6. J. Liu et al., "Experimental performance evaluation of analog signal transmission system with photonic integrated optical vortex emitter and 3.6 km few-mode fiber link", 2016 Optical Fiber Communications Conference and Exhibition (OFC), Anaheim, CA, 2016, pp. 1-3.
7. . Scaffardi, N. Zhang, M. N. Malik, E. Lazzeri, C. Klitis, M. Lavery, M. Sorel, and A. Bogoni, "Two-layer interconnection network architectures based on integrated concentric orbital angular momentum emitters", in Advanced Photonics 2017 (IPR, NOMA, Sensors, Networks, SPPCom, PS), OSA Technical Digest (online) (Optical Society of America, 2017), paper PM2D.2.
8. M. Scaffardi, M. N. Malik, E. Lazzeri, C. Klitis, L. Meriggi, N. Zhang, M. Sorel, and A. Bogoni, "A 3x3 Switch Exploiting an Optical Vortex Beam Emitter based on a Silicon Three-Grating Microring", in Conference on Lasers and Electro-Optics, OSA Technical Digest (online) (Optical Society of America, 2017), paper STu1M.2.
9. Q. Xiao et al., "A coaxially integrated photonic orbital angular momentum beam multiplexer", 2016 IEEE 13th International Conference on Group IV Photonics (GFP), Shanghai, 2016, pp. 114-115.
10. S. Li, C. Klitis, Z. Nong, S. Gao, M. Sorel, S. Yu, and X. Cai, "Orbital Angular Momentum Mode Multiplexer Based on Multimode Micro-Ring Resonator with Angular Gratings", in Conference on Lasers and Electro-Optics, OSA Technical Digest (2016) (Optical Society of America, 2016), paper STh3E.5.
11. G. Cantarella, C. Klitis, M. Sorel and M. J. Strain, "Integrated microrings for on-chip filtering and efficient FWM generation", 2016 Photonics North (PN), Quebec City, QC, 2016, pp. 1-1.
12. S. Fu et al., "4 x 10 Gbit/s L-band WDM transmitter with automatic control of silicon photonic channel multiplexer and carver", 2016 IEEE Optical Interconnects Conference (OI), San Diego, CA, 2016, pp. 118-119.
13. A. Annoni, D. Oliveira De Aguiar, A. Melloni, E. Guglielmi, M. Carminati, G. Ferrari, a. Buchheit, H.-D. Wiemhfer, M. Muoz-Castro, C. Klitis,

M. Sorel, and F. Morichetti, Noninvasive monitoring and control in silicon photonics, Proc. SPIE - Int. Soc. Opt. Eng., vol. 10249, 2017.

List of Figures

1.1	The market forecast for silicon photonics between 2012 - 2024. Source David Thomson et al.	3
1.2	The total electric field and density profile (top) and the electric field profiles for the x, y and z direction (bottom) for the TE mode. . . .	5
1.3	The total electric field and density profile (top) and the electric field profiles along the x, y and z direction (bottom) for the TM mode. . .	6
2.1	Schematic of the Smart Cut process for the production of Silicon on Insulator wafers.	11
2.2	Schematic of the basic fabrication process for a silicon waveguide on an SOI material platform.	13
2.3	Schematic of the VB6 electron beam machine (courtesy of Dr. S. Thoms, e-beam notes).	16
2.4	Graphical view of the effect of the choice of the BSS and SS. From top to bottom, the BSS is linearly increased. There is a value of BSS after which the line edge roughness becomes a problem as shown in the bottom of the picture (courtesy of Dr S. Thoms, e-beam notes).	17
2.5	Stitching error on a coupled optical waveguide system on the axis parallel to the waveguides.	18
2.6	Stitching error on an optical waveguide system on the axis perpendicular to the waveguide. Figure reproduce from M. Gnan et al. . .	19
2.7	The simulated spectra of multiple rings in a single bus waveguide. . .	20
2.8	The optical spectra of a single (blue line) and 64 (green line) identical rings for the evaluation of fabrication process robustness. . . .	20
2.9	Schematic of the exposure and development of a negative (top) and positive resist (bottom).	21
2.10	The chemical structure of HSQ; (a)Cage form and (b) network form.	22
2.11	The thickness of the HSQ mask against the exposure dose.	24
2.12	(a)Schematic of the process steps for the definition of an HSQ layer with a sloped profile (b) SEM image of a ring resonator with sloped HSQ profile on the edges.	24
2.13	Schematic of the process steps for the definition of the guiding layer structures with ZEP resist.	26
2.14	Schematic of the processing steps for the definition of the metallic layer structures with PMMA resist.	27
2.15	(a) Optical image of over exposed SU8 waveguides and (b) Optical image of properly exposed SU8 waveguides.	28

2.16	SEM images of (a) the profile of an etched waveguide, (b) the sidewall of the waveguide and (c) the gap clearance of the etching process using the STS.	32
2.17	Dependence of the etching depth vs gap dimension in the HSQ resist mask.	33
2.18	SEM images of the first etching on the Estrelas using the original recipe from STS	34
2.19	SEM images of (a) the profile of an etched waveguide, (b) the sidewall of the waveguide and (c) the gap clearance of the etching process using the Estrelas tool.	35
3.1	Schematic of a heater integrated on the arm of a silicon Mach Zehnder Interferometer. (a) 3D view, (b) Top view and (c) side view . . .	43
3.2	Simulations of the thermal and optical behaviour of a silicon waveguide with an integrated metallic heater as a function of the upper cladding thickness. (a) The temperature of the silicon waveguide against the height of the cladding, with a heater constant temperature of 75 °C and (b) the optical losses of the TE and TM mode due to the presence of a metallic layer against the thickness of the upper cladding.	45
3.3	Temperature profile for the cross section of the device for a $w_h=900$ nm wide and (a) 30 nm and (b) 50 nm thick heater when a constant current is applied.	46
3.4	Waveguide temperature for different values of heater thickness and width, and for a constant temperature of the heater. Silicon waveguide temperature without any HSQ on the top of the heater (green line) and with HSQ on the top (purple line) for the same heater thickness.	47
3.5	Tuning efficiency dependence on the heater thickness and width. As for the previous simulations the presence of HSQ on the top of the heater has a negligible effect.	48
3.6	The output signal of a MZI for both the bar and the cross outputs as a function of the heater power	49
3.7	Heater tuning efficiency as a function on the heater width, without (blue line) and with (green line) HSQ on the top.	49
3.8	Heater tuning efficiency as a function of the heater offset from the waveguide, for theoretical (blue line) and experimental (green line) results.	50
3.9	SEM image of a cleaved SU8 polymer waveguide.	51
3.10	Schematic illustration of a polymer coupler with an inverse taper (a) 3D view, (b) Top view and (c) side view.	52
3.11	The fundamental TE mode of the polymer waveguide with a width of 2.5 μm and height 2 μm	53
3.12	The effective index of the fundamental TE mode against the width of the polymer waveguide and for different heights.	53

3.13	The optical losses of the fundamental (a) TE and (b) TM mode against the width of the polymer waveguide and for different heights.	54
3.14	Simulation results of the transmitted power against the length of the taper for constant polymer height and different polymer widths for the (a) TE and (b) TM mode.	54
3.15	Simulation results of the optical losses against the misalignment between the inverse taper and the polymer waveguide for the TE (blue line) and TM (green line) mode.	55
3.16	The optical losses of the TE (blue line) and TM (green line) mode against the width of the polymer waveguide.	56
3.17	The optical losses against the misalignment of the inverse taper with respect to the polymer waveguide for the TE (blue line) and TM (green line) mode.	57
3.18	Poincaré sphere for the (a) TE and (b) TM mode, for 0 to 2 μm misalignment between the inverse taper and the polymer waveguide with a step of 250 nm.	58
3.19	The nano-taper used for coupling between a straight and a slot waveguide (a) 3-D view, (b) Top-View, (c) side-view with the straight waveguide as an input and (b) side-view with the slot waveguide as an input.	60
3.20	The effective index against the width of the slot waveguide, for wavelengths of $\lambda=1.5\mu\text{m}$ and $\lambda=3\mu\text{m}$, with a fixed gap width of 100 nm.	61
3.21	The losses at a wavelength of $3\mu\text{m}$ against the width of the slot waveguide for different gap widths.	61
3.22	The coupling efficiency against the taper length between a straight waveguide with a $1.3\mu\text{m}$ width and a slot waveguide with a 980 nm waveguide width and a 100 nm gap at $\lambda=3\mu\text{m}$.	62
3.23	(a) The electric field for a 300 μm long taper as shown in Figure 3.19. (b) The input mode of TE_{00} for a straight waveguide with width of 300 nm. (c-e) The mode profiles for the TE_{00} , TE_{02} and TE_{04} in a slot waveguide with a waveguide width of 980 nm and 100 nm gap.	63
3.24	The coupling efficiency against the taper length between a straight waveguide of 300 nm width and a slot waveguide of 980 nm width and 100 nm gap at $\lambda=1.5\mu\text{m}$.	64
3.25	Schematic of a sub-wavelength grating waveguide.	65
3.26	The effective index of a sub-wavelength grating against the width of the waveguides, for a wavelengths of $\lambda=1.5\mu\text{m}$ and $\lambda=3\mu\text{m}$. The SWG have a periodicity of 200 nm and $\alpha = 150$ nm.	66
3.27	SEM images of the fabricated devices. (a) SWGs with coupling taper, (b) Slot waveguide and (c) An inverse taper to slot waveguide transition.	67
4.1	Schematic of a side-wall Bragg grating geometry.	71

4.2	The simulated optical spectrum of side-walls gratings for the TE polarisation as a function the length.	72
4.3	The simulated optical spectrum of side-walls gratings for the TE polarisation as a function the grating amplitude.	73
4.4	The experimental optical spectra of side-wall gratings for the TE polarisation with 5 nm fixed amplitude as a function of their length.	74
4.5	The extinction ratio of side-wall gratings for the TE polarisation as a function the grating amplitude and length.	74
4.6	Poincaré spheres for polarisation rotation measurements for (a) TE and (b) TM mode in a 500 nm width and 220 nm high silicon waveguide.	75
4.7	The profile of the electric field for the (a) TE and (b) TM polarisation in a 500 nm wide and 220 nm high silicon waveguide.	76
4.8	The simulated optical spectra of side-wall gratings for the TM polarisation as a function the grating length.	77
4.9	The simulated optical spectra of side-walla gratings for the TM polarisation as a function the grating amplitude.	77
4.10	The optical spectra of side-walls gratings for the TE polarisation without (blue line) and with (red line) metal on the top of the waveguides.	79
4.11	The extinction ratio of side-walls gratings for the TE polarisation as a function the grating amplitude and length, without (blue dots) and with (red dots) metal on the top of the waveguides.	80
4.12	Schematic of the top Bragg gratings	81
4.13	The simulated optical spectra of top gratings for the TM polarisation as a function of the length for (a) shallow and (b) deep etched gratings for a fixed hole diameter of 80 nm.	81
4.14	The theoretical losses of the (a) TE and (b) TM polarisation as a function of the grating radius and etching depth.	82
4.15	The profile of the electric field for various etching depths of 80 nm diameter hole in a 500 nm wide and 220 nm high silicon waveguide for the TM mode.	82
4.16	The experimental optical spectra of top gratings, with radius of 40 nm, for the TM polarisation as a function of their length.	83
4.17	The transmission spectra of TE propagation for a single TE filter (blue line) and for a dual TE/TM filter (green line).	85
4.18	The transmission spectra of TM propagation for a single TM filter (blue line) and for dual TE/TM filters (green line).	85
4.19	The level of substrate scattering as a function of the distance from the centre of the output waveguide.	86
5.1	Illustration of the device with angular grating patterned along the inner and top wall of a microring resonator that is coupled to an access waveguide for optical input. The radiated beams are emitted orthogonally to the plane of the rings with a helical wavefront that depends on the periodicity of the grating.	89

5.2	Schematic of the cylindrical coordinate framework used in the theoretical analysis presented in this section	90
5.3	Waveguide geometry (top) and simulated field distribution of the transverse electric field E_T and azimuthal electric field E_{az} for the quasi-TE mode in a single mode silicon waveguide at 1550 nm (bottom). A grating placed on the side of the waveguide would produce a predominantly azimuthal polarised emission, whereas a grating placed on the top would produce radially polarised emission. By using both sidewall and top grating, it is, therefore, possible to engineer the SOP of the emitted light.	95
5.4	Schematic illustration of a ring coupled to an access waveguide and with gratings defined on the inner sidewall (a) 3D illustration and (b) top view.	96
5.5	Schematic illustration of a ring with gratings on the top coupled to an access waveguide (a) 3D illustration and (b) top view.	97
5.6	The experimental set-up for measuring the phase structure for the radiated beam from the silicon chip.	98
5.7	Radiation spectrum for a single ring device (blue line) and devices with 30 nm and 40 nm radius top gratings (green and red line). The spectra were shifted downwards for easier reading.	99
5.8	The unpolarised near field profile (top) and the orthogonal linearly polarised field profile for devices with 30 nm radius top gratings at a wavelength of (a) 1520 nm and (b) 1551 nm. At any point the SOP is predominantly radial.	100
5.9	The unpolarised near field profile (top) and the orthogonal linearly polarised field profile for devices with 40 nm radius top gratings at a wavelength of (a) 1515 nm and (b) 1556 nm. At any point the SOP is predominantly radial.	101
5.10	The far field image of the LHCP (top) and RHCP (bottom) for devices with top gratings with radius of 30 nm and wavelengths 1524 nm, 1537 nm (first split), 1537 nm (second split) and 1551 nm from left to right respectively.	102
5.11	The 3D-FDTD simulation results of the intensity patterns for a radiated beam that is scattered by a top grating. When the total intensity (on the left) is decomposed into the two orthogonal linearly polarised beams, the SOP at any point is radial.	103
A.1	Sketch of the experimental set-up employed for the end-fire characterisation of devices fabricated in SOI.	113
A.2	The extinction ratio between the TE and TM measured after the polariser.	113
C.1	(a) Schematic of a second-harmonic generation experiment. (b) Energy-level diagram for second-harmonic generation.	122
C.2	The effective index against the width of the waveguide, for wavelengths of $\lambda=1.5 \mu\text{m}$ and $\lambda=3 \mu\text{m}$	123
C.3	The losses at a $3 \mu\text{m}$ wavelength against the width of the waveguide.	124

List of Tables

2.1	Electron Beam Parameters for the definition of the patterns.	17
2.2	Electron Beam Parameters for the definition of the SU8 polymer waveguides.	29
2.3	Silicon Etching Parameters for the optimal recipe in the STS ICP tool.	33
2.4	Silicon Etching Parameters for the optimum recipe in the PlasmaPro 100 Estrelas.	36
2.5	Silica Deposition Parameters by PECVD.	38
2.6	Silicon nitride Deposition Parameters with ICP-CVD tool.	39
3.1	Thermo-optic and expansion coefficients for Silicon and Silica. A difference of nearly two orders of magnitude is present between the two thermo-optoc coefficients.	42
3.2	Slot waveguide and 1.5 μm wavelength input taper design parameters.	65
4.1	The design parameters of the final grating device.	84

Abbreviations

SOI	Silicon On Insulator
Si	Silicon
InP	Indium Phospite
Ge	Germanium
GaAs	Gallium Arsenide
<i>LiNbO₃</i>	Lithium Niobate
H	Hydrogen
O	Oxygen
<i>SiO₂</i>	Silica (Silicon Dioxide)
IPA	Isopropyl Alcohol (2-propanol)
HSQ	Hydrogen Silequioxen
TMAH	Tetra Methyl Ammonium Hydroxide
MIBK	Methyl Isobutyl Ketone
PMMA	Poly(Methyl Methacrylate)
Au	Gold
Ti	Titanium
NiCr	Nichrome
JWNC	James Watt Nanofabrication Centre
PIC	Photonic Integrated Circuit
ICT	Information Communication Technology
CMOS	Complementary Metal Oxide Semiconductor
EBL	Electron Beam Lithography
BSS	Beam Step Size
BS	Beam Size

MFS	Minimum Feature Size
RIE	Reactive Ion Etching
CCP	Capacity Couple Plasma
ICP	Inductive Couple Plasma
PECVD	Plasma Enhance Chemical Vapour Deposition
LPCVD	Low Pressure Chemical Vapour Deposition
ICP-CVD	Inductive Couple Plasma Chemical Vapour Deposition
ALD	Atomic Layer Deposition
RF	Radio Frequency
HF	High Frequency
LF	Low Frequency
SOP	State Of Polarisation
TE	Transfer Electric
TM	Transfer Magnetic
PM	Polarisation Maintain
WGM	Whispering Gallery Mode
FSR	Free Spectral Range
LHCP	Left Hand Circularly Polarised
RHCP	Right Hand Circularly Polarised
TPA	Two Photon Absorption
FWM	Four Wave Mixing
OAM	Optical Angular Momentum
AWG	Arayed Waveguide Gratings
MMI	Multimode Interference
MZI	Mach Zehnder Interferometer
OV	Optical Vortices
SWG	Sub Wavelength Gratings
ER	Extinction Ratio
SLM	Spatial Light Modulator
SPP	Spiral Phase Plate
ML	Molded Lens

IR	Iris
BS	Beam Splitter
M	Mirror
L	Lens
PD	Photo Diode
IC	Infrared Camera
BEP	Beam Expander
QWP	Quarter Wave Plate
VC	Visible Camera
Col	Collimator
CMT	Coupled Mode Theory
SVA	Slowly Varying Amplitude
FEM	Finite Element Method
FDE	Finite Difference Eigenmode
FDTD	Finite Difference Time Domain
varFDTD	Variational Finite Difference Time Domain
BPM	Beam Propagation Method
PML	Perfect Matched Layer
PEC	Perfect Electric Conductor
PMC	Perfect Magnetic Conductor

Physical Constants

Speed of Light	c	$=$	$2.997 \times 10^8 \text{ ms}^{-1}$
Vacuum Permittivity	ϵ_0	$=$	$8.854 \times 10^{-12} \text{ F/m}$
Elementary Charge	e	$=$	$1.602 \times 10^{-19} \text{ C}$
Plank Constant	h	$=$	$4.135 \times 10^{-15} \text{ eVs}$
Boltzmann Constant	k	$=$	$1.380 \times 10^{-23} \text{ J/K} = 8.617 \times 10^{-5} \text{ eV/K}$
Thermal Energy	$\frac{kT}{q}$	$=$	$25.7 \times 10^{-3} \text{ V}$ at room temperature ($\approx 300K$)

Symbols

α	absorption coefficient	cm^{-1}
α_{exp}	expansion coefficient	K^{-1}
β	propagation constant	cm^{-1}
$\Gamma_{x,y}$	confinement factor	
$\frac{\Delta n}{\Delta \tau}$	thermo optic coefficient	K^{-1}
ϵ	dielectric constant	F/m
η	impedance of the medium	Ω
λ	wavelength	m
Λ	period	m
μ	mobility	cm^2/Vs
ν	frequency	Hz
ν_m	angular propagation constant	cm^{-1}
ρ	resistivity	Ωm
σ	interface roughness	
τ	thermal time constant	
ϕ	phase	
χ^i	i^{th} order susceptibility	pmV^{-1}
ω	angular frequency	Hz
a_G	amplitude	m
d	diameter	m
D_G	duty cycle	
$\mathbf{E}(\mathbf{r}, t)$	Electric field vector	V/m

h	height	m
H	heat capacity	J
I	luminous intensity	J
I	electric current	A
J	Jones vector	
J	maximum current density	A/m^2
k	coupling coefficient	
k_0	free space wavenumber	cm^{-1}
l	quantum number	
L	length	m
m_{ce}	electron mass	Kg
m_{ch}	hole mass	Kg
n	refractive index	
n_{eff}	effective index	
n_g	group index	
N_e	free electron concentration	
N_h	free holes concentration	
P	Power	W
$P(t)$	induce polarisation	
q	topological charge	
R_{orr}	radius	m
R	resistance	Ω
R_G	reflection	
t	thickness	m
t	time	s
T	Temperature	K
u	velocity	ms^{-1}
w	width	m

*To my family and friends
for their continues support*

Chapter 1

Introduction

1.1 Silicon Photonics

Silicon microelectronic technology is a process in continuing development that has been instrumental in supporting the information and communication technology (ICT) revolution of the 20th century. It enables to integrate several millions of components on a single chip at very low cost and with an ever increasing level of functionality. In fact, since the 1960s, the number of transistors per square inch has been doubling each year following the so called Moores law. Although this trend has slowed down in recent years, the growth is still impressive and a number of novel technologies and architectures are continuously being explored in order to sustain this growth. Currently, the main problem is in the very high power consumption required to interconnect the transistors, which is now accounting for more than 80% of the total chip energy consumption [1]. Because the maximum energy that can be consumed by a chip is governed by thermodynamics and cannot indefinitely increase, alternatives to the current copper wiring technology must be found. To this end, the most appealing approach appears to shift to photonic interconnects where electrical wires are replaced by silicon photonic waveguides that offer a large increase in the bandwidth yet maintaining cost low and low power consumption. As a matter of fact, the biggest companies such as IBM and Intel [2] have already made very large investments in integrated photonic devices.

Such large investments from large companies has fuelled a massive growth in research and industrial activities in silicon photonics. Also, with the establishment of initiatives such as multi-project wafer services [3] both the cost and know-how can

be shared amongst several users thus making the development of silicon photonic integrated circuits (PICs) accessible to a very large base of potential users. Besides the high-valued markets of interconnects and datacomms [4] (Figure 1.1), silicon photonics is becoming a platform of great interest for numerous other applications such as spectroscopy, sensors, lab-on-chip for diagnosis, imaging, logic circuits [5]. It is worth noting that historically the PIC landscape has always been fragmented across a variety of material systems that include indium phosphide (InP), germanium (Ge), gallium arsenide (GaAs), lithium niobate ($LiNbO_3$), polymers and glass. Most research has been application driven and this led to a scenario with as many technologies as applications. The shift to fewer generic technologies that can support a larger range of functionalities and decrease the entry cost for users is therefore a very welcome one.

Thanks to more than 50 years of very large investments in microelectronic technology, silicon photonics can benefit from very high quality wafers with negligible level of defects (see Appendix A). In particular, silicon on insulator (SOI) wafers fabricated with the Smart-cut technique [6] offer an excellent material platform for the development of PICs as it is transparent at telecom wavelengths and provides high index contrast waveguides thanks to silicon dioxide cladding. The latter is a key requirement for minimising the waveguide bent radius and to therefore increase the component density.

One of the main advantages of silicon is the compatibility with the metal oxide semiconductor (CMOS) technology, which not only enables the co-integration of silicon photonics and silicon microelectronics but also allows to benefit from one of the most mature technologies ever developed [7]. The fabrication of silicon photonics devices requires photolithography to define the pattern, etching for transferring the pattern to the silicon core, depositions techniques for defining multilayered structures, PIN junctions for fast modulators, metallic layers for electrical connections and tuning. All these fabrication techniques are very well-assessed in any standard CMOS fabrication line and are available on a 12 wafer size. These are the reasons why silicon photonic can offer low cost, large volume and high yield production, and is likely to dominate the integrated photonic landscape for several years to come. [5, 8–13].

As mentioned above, a main advantage of SOI technology lies in the high index contrast of the optical waveguides. In fact, with the refractive index of silicon being $n_{Si} = 3.48$ and silica $n_{SiO_2} = 1.46$ the refractive index contrast for a silicon

photonic waveguide is $\Delta n \approx 2$ allowing the fabrication of very small cross section waveguides and a very tight modal confinement. The standard cross section of 220×500 nm used for single mode operation waveguides [8] provides small bending radii as small as $R = 1.5 \mu\text{m}$ with low propagation and bending losses.

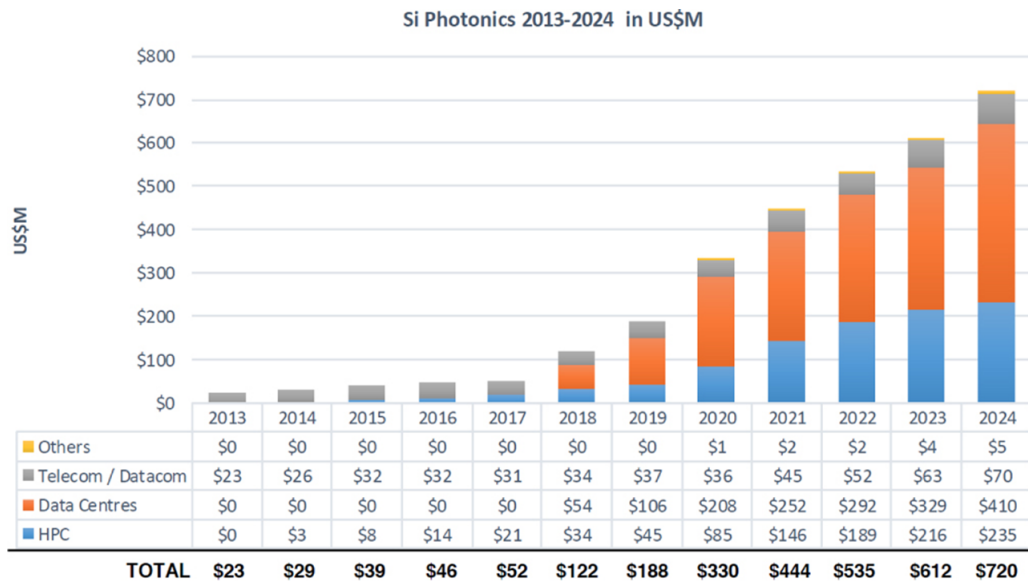


FIGURE 1.1: The market forecast for silicon photonics between 2012 - 2024. Source David Thomson et al. [4].

However, such a large refractive index contrast is also one of the major weaknesses of this technology. A number of problems arise from the large refractive index contrast: a) The small waveguide cross section required for single mode propagation means a high interaction of the mode with the sidewall of the waveguides. As a consequence, any roughness present on the sidewalls induces high propagation losses (i.e. 5 nm of r.m.s. roughness can induce propagation losses as high as 10 dB/cm). With current technology, the lowest propagation losses on a deeply etched single mode waveguide is of the order of 1dB/cm [14]. It is unlikely that this figure will largely decrease in the future unless major changes in the geometry or technology are introduced [15] [16]. b) The small waveguide cross section leads to a large mismatch with the optical fibres that are used to interface the PIC to the external world. Typical losses between optical fibres and silicon waveguides can be as high as 10dB/cm. Either mode adapters in the form of inverse tapers [17] or grating couplers [18] can be used to improve the mode matching and increase the coupling efficiency. However, none of these approaches is ideal in terms of fabrication tolerances, operational bandwidth or polarisation manipulation. c) The high index contrast of silicon photonic waveguides means that small variations of the waveguide dimensions translates into large alterations of the effective modal

index. As such, silicon photonics is a technology very susceptible to fabrication tolerances. d) With increasing index contrast, the field components at the dielectric interfaces of the waveguide are both in the longitudinal and transversal direction. Therefore, the propagating modes are not purely transversely polarised, but can be referred as quasi modes (hybrid modes). The lack of mode purity results into polarisation mismatch between the silicon waveguide and optical fibre mode. e) The high refractive index contrast and the subsequent strong interaction with the sidewall roughness generates a substantial level of light scattering. The first consequence of the scattering is an increase in the propagation losses. However, some of the scattered light is still guided and might become depolarised or uncoherent.

Because most of these issues scale quadratically with the refractive index contrast [19], the consequences they have on the performance of silicon photonic devices can be very substantial. Therefore, a clear understanding on how these effects are related to technology and device design is required in order to minimise their impact. The understanding and mitigation of the polarisation rotation due to scattering form the main motivation for this thesis.

1.2 Polarisation in silicon photonics

In the initial stages of the development of silicon photonic devices, large cross section waveguides were considered due to their low losses [20]. The main characteristics of large SOI waveguides such as the bending losses [21] and birefringence [22–28] have been investigated in detail. Several passive elements have also been developed [29–34], with the first arrayed waveguide grating (AWG) demonstrated by Trinh et al. as early as 1997 [34]. One of the advantages of large ridge SOI waveguides is the good phase control and robustness to fabrication tolerances compared to small cross section SOI waveguides, which has rapidly led to commercial applications. The major drawback is that the bending radius for large ridge waveguides is of the order of 100 to 1000 μm [21].

The need for sharp bending radii as small as 1 to 2 μm [35] and compact microrings [36] or AWG [37, 38] required a shift towards waveguides with stronger modal confinement and smaller cross sectional dimensions. A consequence of the high index contrast between the silicon and the silica in small Si nanowires, is the considerable birefringence the waveguides have. For large SOI ridge waveguides the

birefringence is on the order of 10^{-3} to 10^{-5} , whereas for small waveguides is several orders of magnitude higher [37] and introduce strong polarisation dependence [37].

For the typical waveguide geometry used in this work (500×220 nm) two modes of different polarisation (TE and TM) can propagate, with a very different effective index of $n_{TE} = 2.44$ and $n_{TM} = 1.77$ for the TE and TM polarised mode, respectively. The origin of the strong birefringence can be easily understood by inspecting the field profiles of the modes. Figure 1.2 shows the electric field and density profile (top) of the TE mode in a silicon waveguide with dimensions 500×220 nm and the three different components for the electric field (bottom). The TE mode is mainly propagating in the centre of the waveguide with strong interaction with the lateral sidewalls. As a consequence, it is strongly affected by any roughness on the edges of the waveguide leading to high propagation losses and strong polarisation scattering.

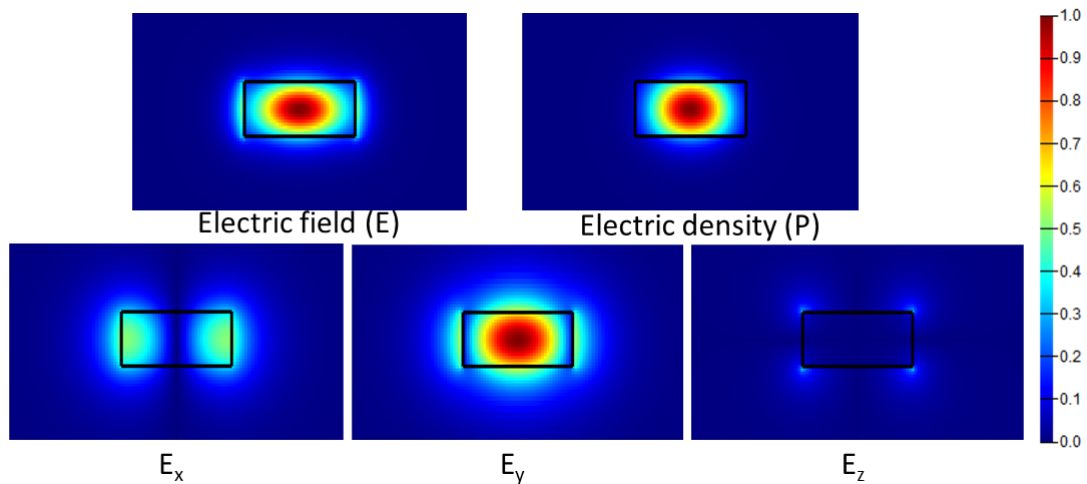


FIGURE 1.2: The total electric field and density profile (top) and the electric field profiles for the x, y and z direction (bottom) for the TE mode.

Similarly, Figure 1.3 shows the total electric field (top) and the individual components (bottom) of the electric field for the TM mode for a waveguide with the same dimensions. While the TE mainly propagates in the middle of the waveguide, the TM is much less confined and stretches in the vertical direction, which justifies the much lower effective refractive index. The TM mode strongly interacts with the upper and lower cladding and, as such, it is more affected by the quality of the silica layer and by any metallic layer that are deposited on the top of the cladding. This feature can become of interest in the design of TM absorbers and will be discussed and analysed in detail in Chapter 4.

In both cases, the electric field profile is the one used to describe the behaviour and the way of propagation of the mode in the waveguide [158].

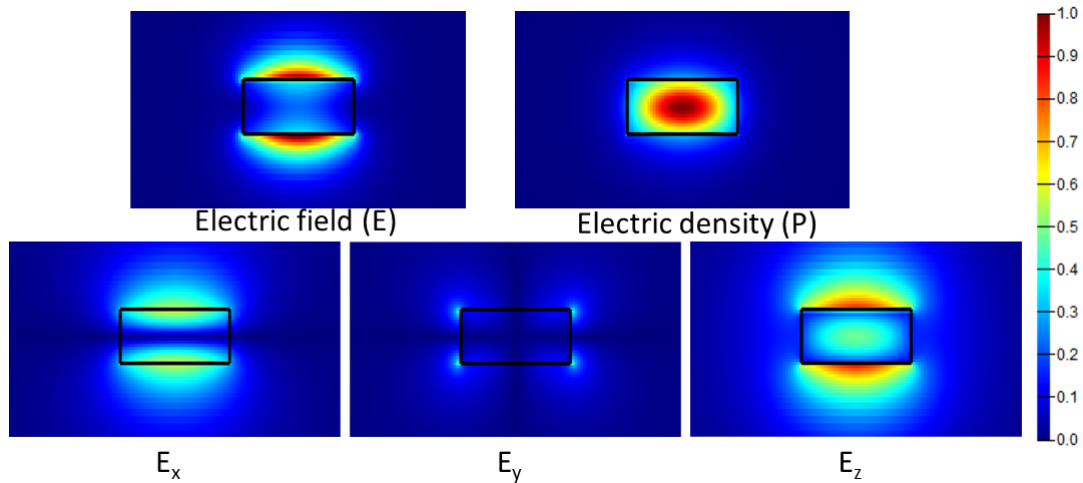


FIGURE 1.3: The total electric field and density profile (top) and the electric field profiles along the x, y and z direction (bottom) for the TM mode.

When light with random polarisation (which is usually the case for fibre optical communications) are coupled to a PIC, components insensitive to polarisation are needed to avoid a degradation of the signal-to-noise ratio. One solution is to optimise the waveguide geometries [22–28, 34] or by controlling the stress of the oxide cladding [27, 28] so as to make the two polarisations degenerate. Also, unique approaches were implemented to reduce the polarisation sensitivity of silicon nanowires in microring resonators, multimode interference (MMI) couplers [39] and AWG de/multiplexers [40, 41]. These solutions are easy to implement on large ridge waveguides, however, for small nanowires, as in our case, the tolerance to fabrication variations becomes very significant. Also, in a scenario with strong scattering, a very strong polarisation coupling occurs between two degenerate polarisations, which has a dramatic impact of the performance of most devices [42].

Another approach is the so called polarisation diversity technology [36]. With the use of a polarisation-selective beam splitter at the input of the chip the two polarisations are first separated (TE and TM polarisation) and then one of the two is converted to the other with a polarisation rotator, in order to obtain two beams with identical polarisation. The two beams propagate into two identical PICs and hence are subject to the same optical transfer function. At the output, the second beam is rotated back to the original polarisation before the two beams are

combined again. Due to the large birefringence of silicon nanowires, it is possible to create compact integrated beam splitters [43] and polarisation rotators [43].

Moreover, an accurate control over the polarisation of the propagating beam is of great importance in non-linear processes. For example four-wave mixing (FWM), which finds a large spectrum of applications such as wavelength multicasting [44], logic gates [45] and wavelength conversion [46], is polarisation sensitive. In fact, the efficiency of the process is strongly dependent on the polarisation state of the incident light [47].

Therefore, in the design of photonic integrated circuits an effective management of the polarisation is of great importance both for independently manipulating the two polarisation states a functionality that is particularly important in telecomm applications or for mitigating the consequences of the strong polarisation scattering.

1.3 Motivation

The need to take pace with Moore's law in future microelectronic circuits has driven the development of silicon photonics to overcome the bottleneck of electrical copper interconnects. In fact, optical interconnects are currently regarded as the most promising approach for increasing the speed of intrachip connections and the integration potential of future electronic chips. Supported by the vast CMOS infrastructure, several design houses and multi-project wafer services, silicon photonics have experienced an explosive growth with the demonstration of chips integrating as many as thousands of different components. Such an increase in the device complexity, however, has also exacerbated a number of issues related to the high refractive index contrast of the SOI platform, such a poor robustness to fabrication tolerances, strong light scattering and high power consumption for component trimming.

The main aim of this research activity is to address some of these issues. The initial part of the thesis deals with the design and fabrication optimisation of a number of basic components such as heaters for trimming, inverse tapers for fibre coupling and sub-wavelength waveguides, with the main aim to improve their losses, power consumption and tolerance to fabrication errors. The second part of the work investigates the impact of the strong polarisation scattering on the

performance of integrated Bragg filters with high extinction ratio. Novel polarisation selective grating geometries are proposed and used to demonstrate filters with superior extinction ratio performance and ring resonators that emit vertical free space beams with arbitrary polarisation.

1.4 Thesis outline

The thesis is organised as follows:

Chapter 2 describes the main fabrication techniques used in this work. Following an initial introduction on the silicon-on-insulator material platform, a detailed analysis is presented on the main process flow to fabricate silicon photonic integrated chips. Particular emphasis is given to the optimisation of the most critical fabrication steps such as e-beam lithography, dry etching of the waveguide and deposition of the dielectric layers.

Chapter 3 discusses the design and fabrication optimisation of a number of basic components that have a substantial impact on the device performance. These include thermal actuators with minimum power consumption, low-loss inverse polymer tapers for optical fibre coupling and sub-wavelength waveguides to enhance non-linear interactions.

Chapter 4 focuses on the development of polarisation selective integrated filters. The work is motivated by the need to improve the extinction ratio of Bragg filters whose performance are limited by the strong polarisation scattering. The first solution investigated consists of a simple TM filter in the form of a metallic strip, followed by a detailed analysis on Bragg gratings for selectively filtering of the TM mode. Experimental results with both design approaches are presented and discussed, showing record extinction ratio figures as high as 60 dB.

Chapter 5 discusses the design of microring resonators integrated with Bragg gratings for free-space vertical emission of vortex beams. The Bragg grating devices presented in Chapter 4 are used to control the output polarisation of the emitted beam. The design and evaluation of emitters with radial and azimuthal polarised light are presented.

The final chapter (Chapter 6) concludes the thesis, summarising the main findings and presenting ideas for future work.

Additional work that provides useful theoretical background to this thesis is reported in four appendices. The first appendix describes the origin of the losses in silicon waveguides and the experimental set up used for most of the optical device characterisation. The second appendix reports on the main simulation methods used in this work such as FDE, BPM and FDTD. The third appendix introduces the design of non-linear waveguides based on the slot and sub-wavelength waveguides presented in Chapter 3.

Chapter 2

Fabrication

In silicon photonic devices, the high index contrast between the silicon core and the silica cladding adds severe demands and constraints to the accuracy of the fabrication process. For example, low-loss and single mode operation require waveguides with sub-micrometer cross-sections and nanometer scale sidewall roughness; misalignments as small as 100 nm between the silicon waveguides and the input/output mode adapters translates into substantial polarisation rotations; a deviation of a few nanometers only in the waveguide dimensions of a ring resonator produces a shift of several 10s of GHz in its resonant peak. These few examples indicate that high quality and accurate fabrication processes need to be developed together with designs that offer robustness against fabrication tolerances.

This chapter will first discuss the fundamental properties and geometry of the silicon-on-insulator (SOI) material platform used in this work. A brief overview of the general fabrication process flow will then be given followed by a detailed explanation of the main processes used for the fabrication of the devices presented in this thesis. Particular emphasis will be given to the optimisation of electron beam lithography and dry etching which represent the most critical fabrication steps. Also, the tolerances and limitations of the overall process will be analysed to guide the designs of the components presented in Chapter 3.

2.1 Material

As discussed in Chapter 1 the material of choice for this work is the silicon-on-insulator (SOI) produced by Soitec [48]. The wafers are fabricated by a UNIBOND process based on the Smart Cut technique, which provides, high-quality crystalline silicon material for the core, low interface roughness and a very accurate thickness of the core layer. A detailed description of the material fabrication process is shown in Figure 2.1 [49].

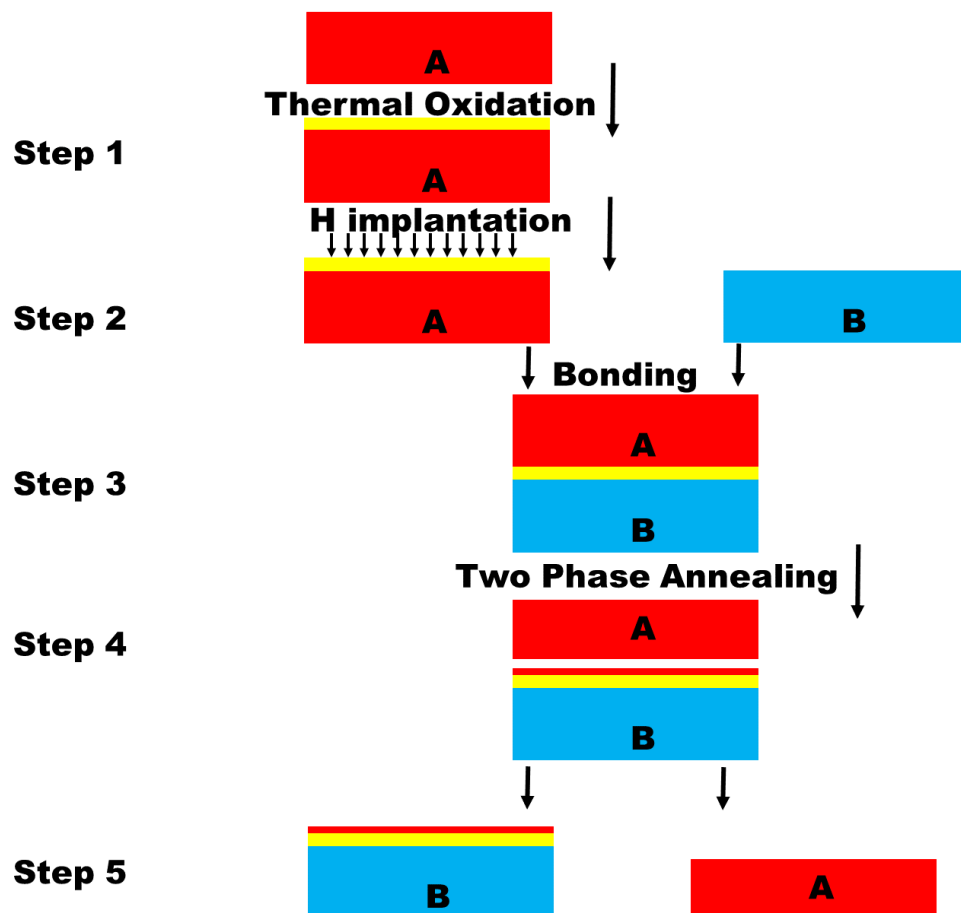


FIGURE 2.1: Schematic of the Smart Cut process for the production of Silicon on Insulator wafers.

The fabrication process for the material of choice for this work shown in Figure 2.1 comprises of five major steps:

1. The first step of the process is to thermally oxidise a silicon wafer (wafer A in Figure 2.1). This oxide layer will become the BOX layer of the final SOI

structure. Wet thermal oxidation is used to obtain a low roughness interface between the silicon and the silica as well as to ensure accurate control over the oxide thickness.

2. The second step is the hydrogen (H) implantation. Through their implanting energy, it is possible to accurately control the exact penetration of the ions into the silicon layer with an accuracy of a few nm across an eight-inch silicon wafer. This penetration depth will define the thickness of the final silicon core layer.
3. The wafer is then chemically cleaned and hydrophilically bonded to a silicon wafer (wafer B in Figure 2.1) by Van Der Waals forces. Wafer B acts as a stiffener and provides the bulk silicon substrate beneath the buried oxide layer.
4. The fourth step consists of two thermal treatments. The first one, at a temperature of 400 - 600 °C, splits wafer A into two parts along the plane previously implanted by H ions. The thin layer of silicon that remains bonded to wafer B completes the SOI structure. The second annealing step is performed at 1100 °C on wafer B to strengthen the chemical bonds of the SOI wafer.
5. The final step is a touch polishing after the splitting to obtain a high-quality surface. The remaining of wafer A can be used as a new wafer B for a subsequent process.

The final SOI wafer used in this work is composed of three layers: a top layer of Silicon (the core), with a nominal thickness of 220 nm. This layer after patterning and etching forms the guiding core for the optical devices. The layer is lightly acceptor doped (Boron), with a value of electrical resistivity of 10 Ωcm , corresponding to a doping concentration of approximately $10^{15} cm^{-3}$ [50]. The optical losses induced by this doping concentration can be considered negligible. The BOX layer (thermal oxide) below the core layer has a nominal thickness of 2 μm and forms the lower cladding of the optical devices. The interface between the silicon and the silica layer is very sharp with a very low level of roughness [49]. Finally, the substrate layer is made of bulk silicon, with an approximate thickness of 730 μm , which gives sufficient mechanical stability to the wafer.

2.2 Fabrication Process

The fabrication of photonic devices can be a challenging and time demanding process, with many steps requiring careful optimisation. The fabrication steps that define the guiding layer are the most important and critical of all as their quality and success will determine the performance and the main optical characteristics of the optical device. As a consequence, extreme care has to be taken to reproduce the device design onto the fabricated chip accurately.

Figure 2.2 summarises the five main fabrication steps for fabricating an optical waveguide on an SOI material. These steps are:

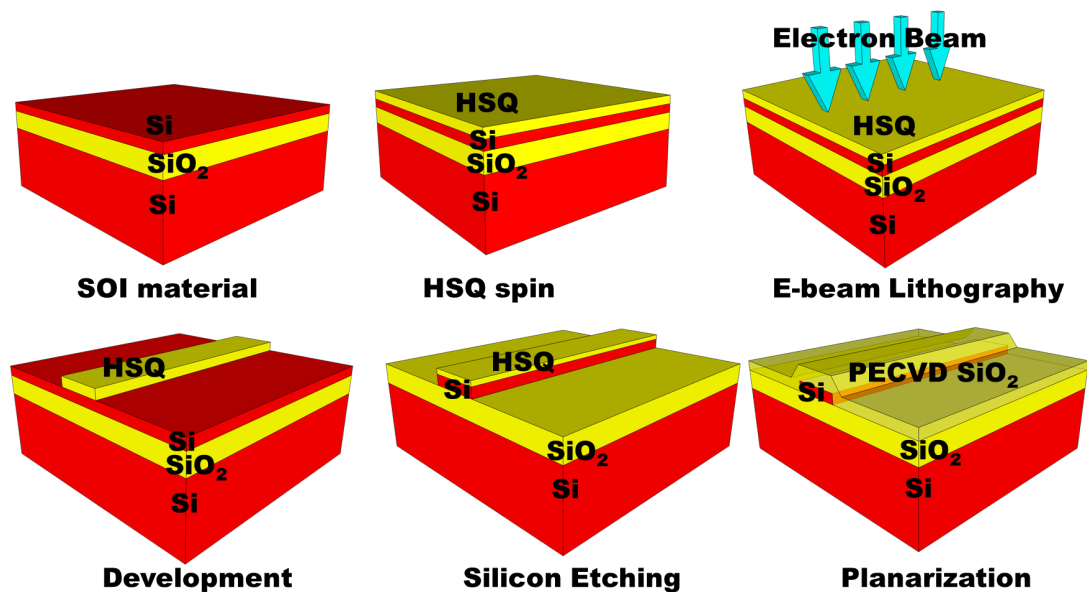


FIGURE 2.2: Schematic of the basic fabrication process for a silicon waveguide on an SOI material platform.

1. Following a chemical cleaning, a thin layer of electron-beam resist is spun on the sample. As will be discussed later, the electron-beam resist used in this work is Hydrogen Silyloxy which combines excellent resolution and low writing times. However, depending on the final devices or applications to be targeted, a number of different electron-beam resist alternatives can be used.
2. The electron-beam resist is patterned by electron beam lithography.

3. Following the electron exposure, the sample is hard baked for an hour at 180 °C, to increase the resist resolution, before being developed in a solution of 25 % TMAH (Tetra-Methyl- Ammonium Hydroxide) at 21 °C.
4. The written pattern is then transferred into the silicon core by ICP reactive ion etching. It is worth noting that upon baking HSQ becomes a silica-like compound and therefore it can be directly used as a hard mask for the etching of the silicon. If softer masks are used, a transfer of the patterns into a hard mask may be required
5. The final step is to deposit a 1 μm thick layer of silica, which protects the waveguides from the external environment (i.e. dust, moisture) and provides a sufficiently thick cladding to avoid any optical loss when metallic layers are deposited on the top of the chip.

In the rest of this chapter, a detail explanation of each step will be given.

2.3 Electron Beam Lithography (e-beam)

Lithography, which literally means stone writing, is a critical step in any nano and microdevice fabrication as it defines a pattern onto a material. There are three main ways currently used for patterning: photolithography, charged beam lithography, and nanoimprinting [51].

Photolithography is a term that includes all those processes in which light radiation is used to impress a photosensitive resist through a photomask that contains the pattern to be transferred [51]. It offers fabrication at a wafer-scale level, which is of great interest for large volume and low-cost production. Its major limitation is the minimum size of the pattern which is limited by the wavelength of the light source (365 nm in our fabrication facility). Furthermore, the fabrication of the photolithography masks can be a lengthy and expensive process that is not particularly suitable for prototyping and chip-level process development. The limitation on the minimum pattern feature size and the limited flexibility at the process and device development stage made this technology unsuitable for this work.

Nanoimprinting is the process in which a pattern is transferred to a soft resist through a reverse mask by pressure and heat [51]. It offers wafer scale fabrication capability without the diffraction limit of the photolithography. On the drawbacks, a negative mask needs to be fabricated, which can be a lengthy and expensive process. Furthermore, the method usually requires high pressures and temperatures, which can deteriorate and damage both the fabricated sample and the negative mask.

Charged electrons beam lithography is a far more suitable process for nanometer-size features and rapid prototyping. Even though e-beam lithography is a costly and time-consuming process, it provides the required flexibility in the design optimisation process together with superior resist patterning resolution.

In order to obtain patterns with electron beam lithography, an initial design has to be generated by a CAD-like software (L-edit is used in this work [52]).

After the pattern is designed with the use of L-edit, an automatic software (Beamer) splits the design in multiple trapezia. The reason for such process arises from the limitation of the moving mechanical system of the machine. The distance and the design of these trapezia will affect the final fabrication, and hence extra care has to be taken in defining the minimum and maximum distance between instances. The software automatically sets the trapezia in a square lattice grid that determines the resolution of the lithographic process. The machine exposes dots with a user-defined size (called Beam Size - BS) separated by a constant gap called the Beam Step Size (BSS). The pattern is therefore fractured into a discrete set of exposed pixels.

The machine available in the James Watt Nanofabrication Centre [53] is a Vistec VB6- UHR-EWF e-beam tool. A schematic of the EBL tool can be seen in Figure 2.3. A filament produces high energy electrons (100 keV) that are then focused by a series of apertures and magnetic fields. This complex lensing system is required to compensate for the tilt and non-uniform height of the substrate. The beam size is selected by the changing diameter of a variable aperture, and the writing spot is determined by the exposing dose of the resist as well as from the BSS.

The selection of the proper dose and BSS is a critical step in the fabrication of photonic devices as it defines the roughness of the optical waveguides edges, which affects the light scattering and propagation losses substantially. Figures 2.4 shows the effect of increasing the BSS. While small BSSs result in long writing times and

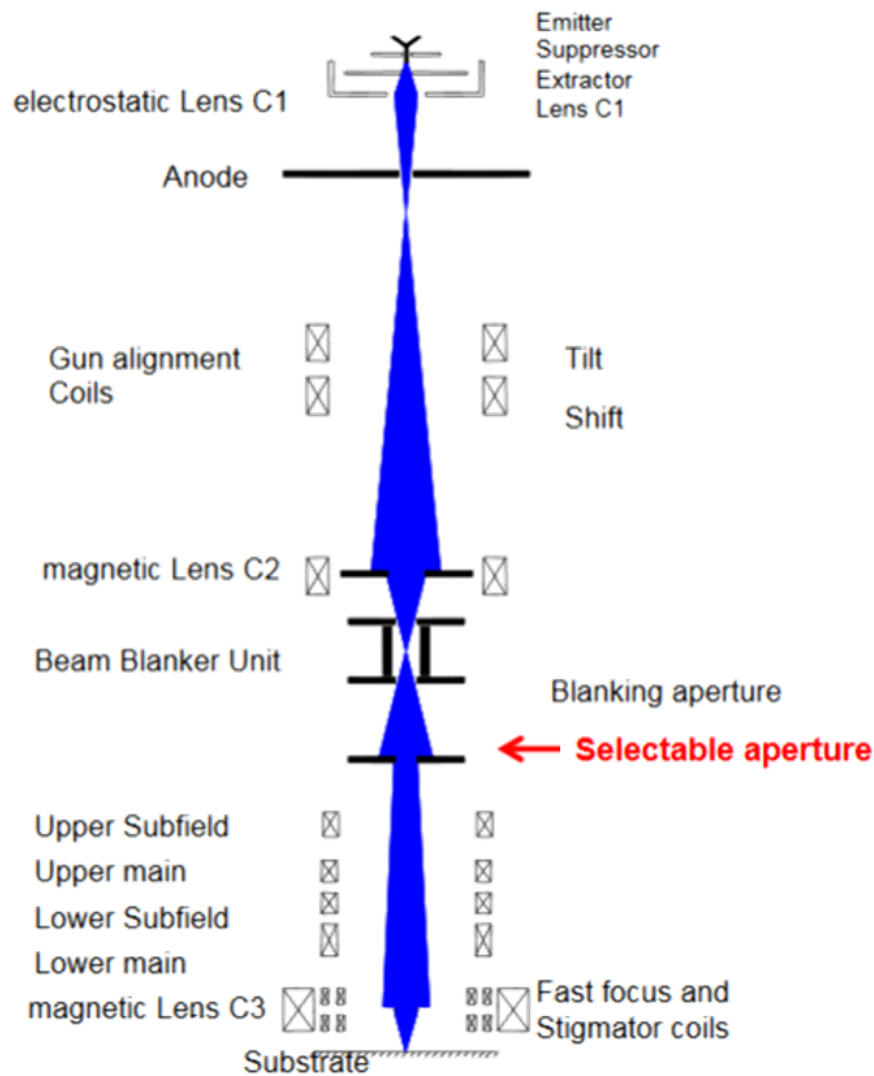


FIGURE 2.3: Schematic of the VB6 electron beam machine (courtesy of Dr. S. Thoms, e-beam notes).

in having the same area exposed multiple times, large BSSs might leave unexposed areas. In particular, there is a critical value of the BSS after which the line edge roughness becomes noticeable.

Based on a number of preliminary tests on the edge roughness, during this work, the value of the BSS was kept half of that of the BS. This value provides a good compromise between edge roughness and writing time. In order to overcome the problem of over-exposure due to multiple dots exposing the same pixel, the dose was optimised through various dose tests. As mentioned above, EBL is an expensive process and hence the writing time needs to be reduced as much as possible.

Parameters	High Resolution	Low Resolution
Resolution (nm)	1	1
Beam Size (nm)	4/6	33/65
Beam Step Size (nm)	2/3	16/32

TABLE 2.1: Electron Beam Parameters for the definition of the patterns.

For this reason, not critical features, where the edge line roughness does not influence the behaviour of the device, were written with a much larger spot. Table 2.1 summarises the parameters of the BSS used during this work.

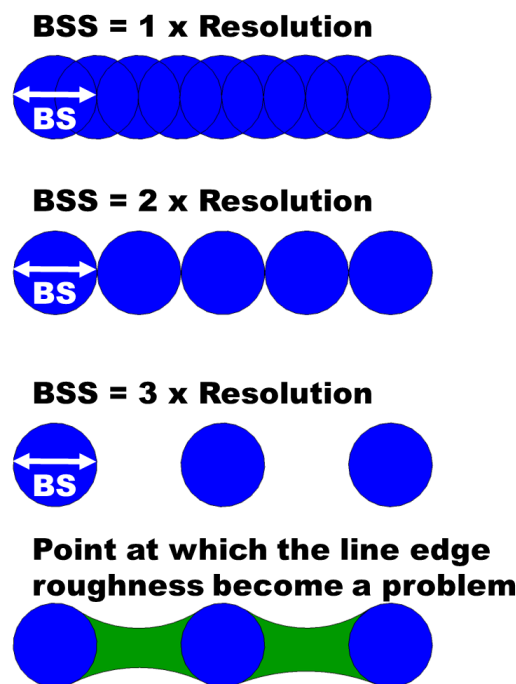


FIGURE 2.4: Graphical view of the effect of the choice of the BSS and SS. From top to bottom, the BSS is linearly increased. There is a value of BSS after which the line edge roughness becomes a problem as shown in the bottom of the picture (courtesy of Dr S. Thoms, e-beam notes).

A significant issue with EBL is that the collisions of the electrons with the atoms of the substrate generate substantial scattering and secondary electrons that can re-expose the resist. This effect is particularly critical in designs with high-density patterns because the scattered electrons coming from adjacent exposed areas tend to over-expose the resist. This problem is known as the proximity effect and can be solved by running a proximity correction software based on Monte Carlo simulations, which re-adjusts the dose depending on the density of the pattern, the type of substrate and the thickness of the resist.

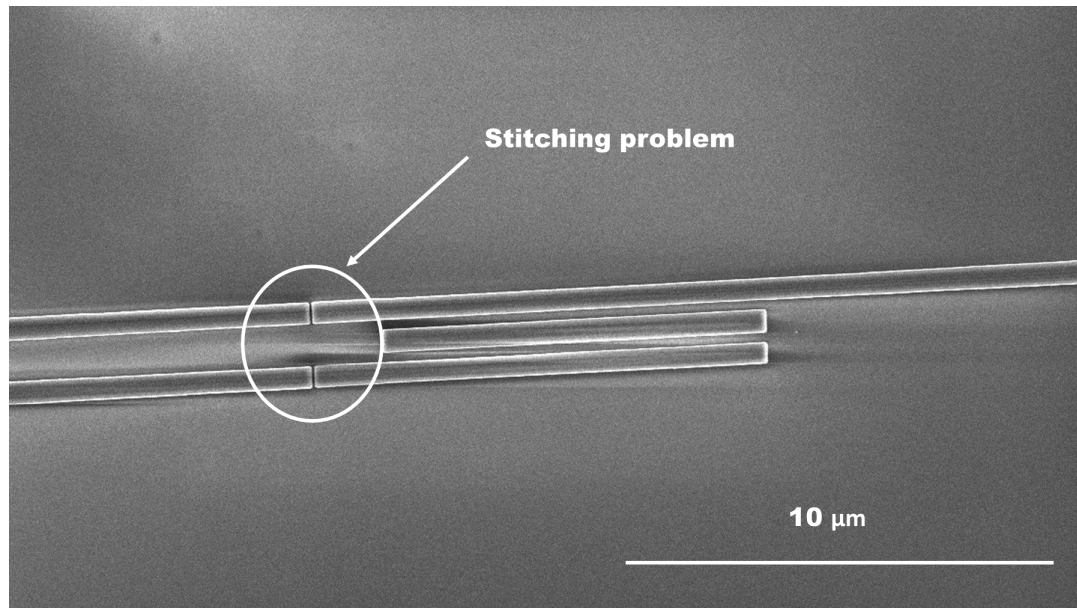


FIGURE 2.5: Stitching error on a coupled optical waveguide system on the axis parallel to the waveguides.

Another important EBL parameter to consider during the lithographic process is the field size of the machine, which corresponds to the area that can be written without having to translate the sample mechanically. For a resolution of 1nm, the field size has a dimension of $1048.576 \times 1048.576 \mu m^2$. This affects the patterns as discontinuities might appear at the boundaries between different fields. Furthermore, due to the long writing times, the machine exhibits a mechanical drifting which was measured to be in the order of 50 nm in the first half hour and 150 nm over 2 hours in both x and y directions. As a result, waveguides present in different fields may present stitching features as those shown in Figure 2.5. In order to address this issue, the dose is increased at the boundaries between fields to mitigate stitching along the waveguide direction (i.e. that of Figure 2.5) and alignment correction is performed every 15 minutes to mitigate stitching perpendicular to the waveguide (i.e. that of Figure 2.6).

The impact of the electron beam stitching on the performance of optical devices has long been investigated in the group [54]. However, even if extreme care is taken in minimising stitching and edge line roughness, the accuracy of the process is limited by a "fabrication noise" that comes from unavoidable non-uniformities in the lithographic and etching processes as well as in the SOI material. In order to validate the robustness of the process a simple experiment as in [55] was performed, which consists of comparing the performance of a single ring coupled to a bus waveguide with 64 identical rings, all of them coupled to the same bus waveguide.

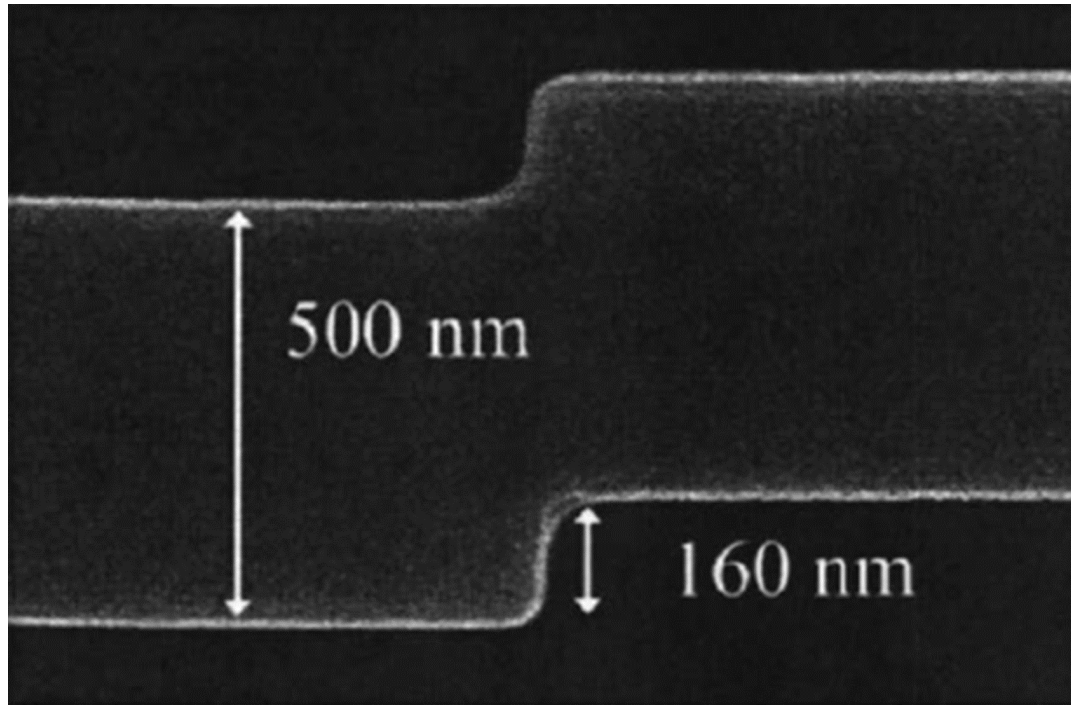


FIGURE 2.6: Stitching error on a coupled optical waveguide system on the axis perpendicular to the waveguide. Figure reproduced from M. Gnan et al. [54].

All the rings being identical, the resonances in the two configurations exhibit the same value of full width half maximum (FWHM), though the 64-ring device shows the typical resonance shape of a higher order filter (i.e. higher extinction ratio and more vertical profile, see Figure 2.7). In a real device, however, any non-uniformity slightly shifts the resonance position of the 64-ring device resulting in a broadening of its resonances. The larger the broadening, the higher the fabrication noise of the process. The measurements of Figure 2.8 clearly show that the resonances broaden from a value of 17.5 GHz for the single-ring to 126.25 GHz for the 64-ring device. This same experiment was repeated several times over the years and always provided similar values of 126 GHz for the resonance broadening, indicating a good stability of our process.

We can use the resonance broadening $\Delta\lambda$ to find the fabrication error through the following formula [55]:

$$\Delta w = 1.16\Delta\lambda - 2.38\Delta t \quad (2.1)$$

Where Δt and Δw are the variation in width and height of the silicon waveguide.

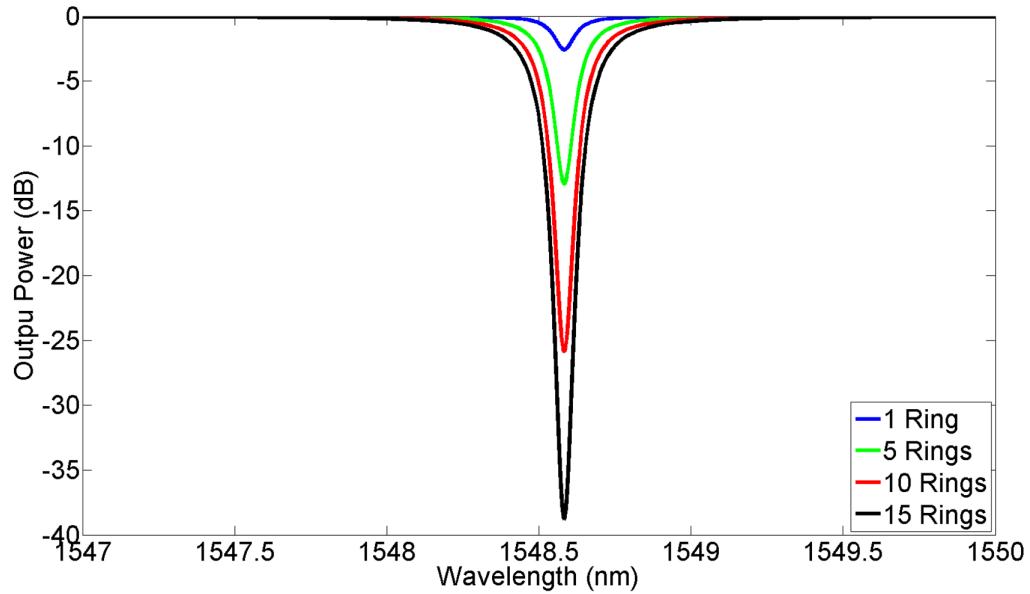


FIGURE 2.7: The simulated spectra of multiple rings in a single bus waveguide.

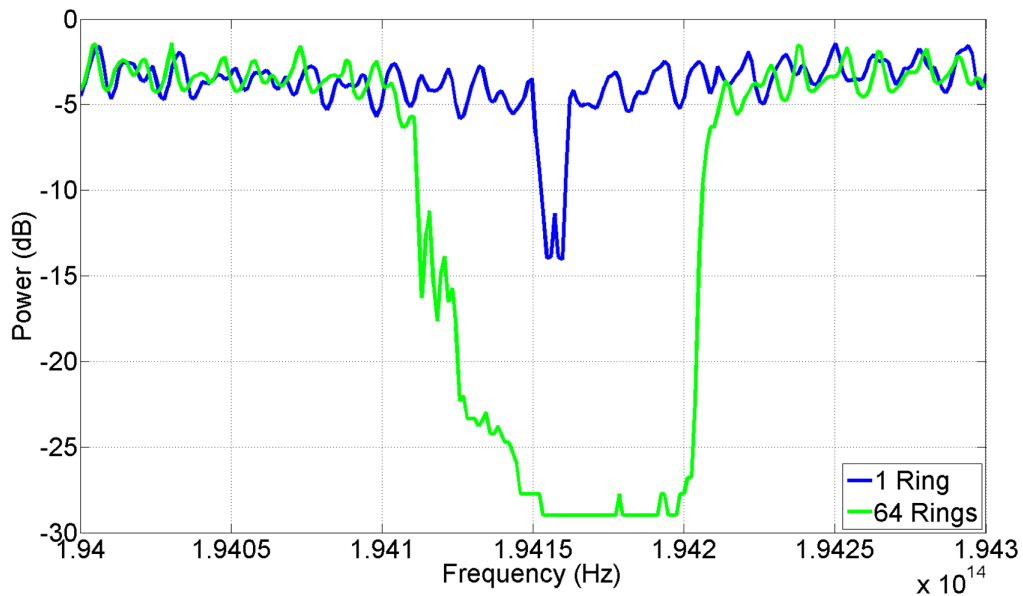


FIGURE 2.8: The optical spectra of a single (blue line) and 64 (green line) identical rings for the evaluation of fabrication process robustness.

Under the assumption that the variation of the thickness (Δt) of the waveguide is negligible due to the proximity of the ring resonators, we can estimate the average variation of the waveguide width (Δw) across the 64 rings. The width variation was found to be ± 0.42 nm, which is value well below the resolution chosen for the fabrication of the optical waveguides (1 nm). A sub-nm value for Δw is probably close to a fundamental limit, and it is therefore unlikely that large improvements will appear in the future.

2.4 Resists

For the definition of the design pattern by EBL, a resist sensitive to electron irradiation is needed. Upon exposure, the chemical structure of the inorganic polymer changes, making it more or less soluble in the developer. Depending on how their solubility change, resists can be classified as negative (top of Figure 2.9) or positive resist (bottom of Figure 2.9).

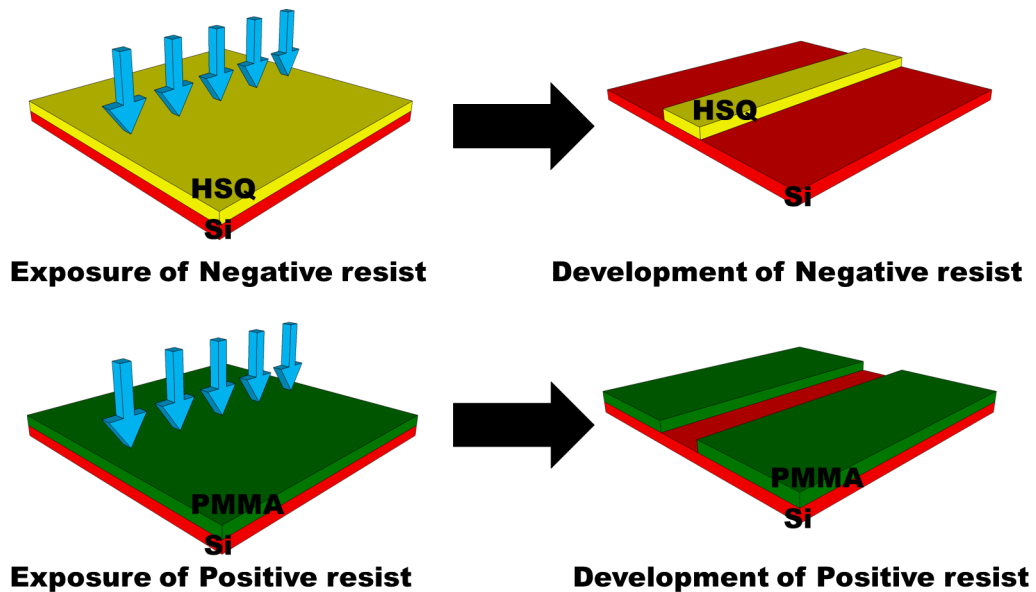


FIGURE 2.9: Schematic of the exposure and development of a negative (top) and positive resist (bottom).

Resists are usually characterised by:

- **Sensitivity:** The amount of radiation needed for a positive resist to clear out or, for a negative resist, to maintain the original thickness following development. The highest the sensitivity the lower the radiation energy needed.
- **Contrast:** The selectivity of the developer between exposed and unexposed resist.

As part of this work, a total of four different resists (two positive and two negatives) have been used with various sensitivities and contrasts. Depending on the requirements of the specific fabrication step, the appropriate resist was used. In the rest of this section, the main features of these resist will be presented.

2.4.1 HSQ

HSQ (Hydrogen Silsesquioxane), also known as FOX16 [56], is a negative e-beam resist with low sensitivity and high contrast. It is widely used for all those patterns that require high resolution and low writing time.

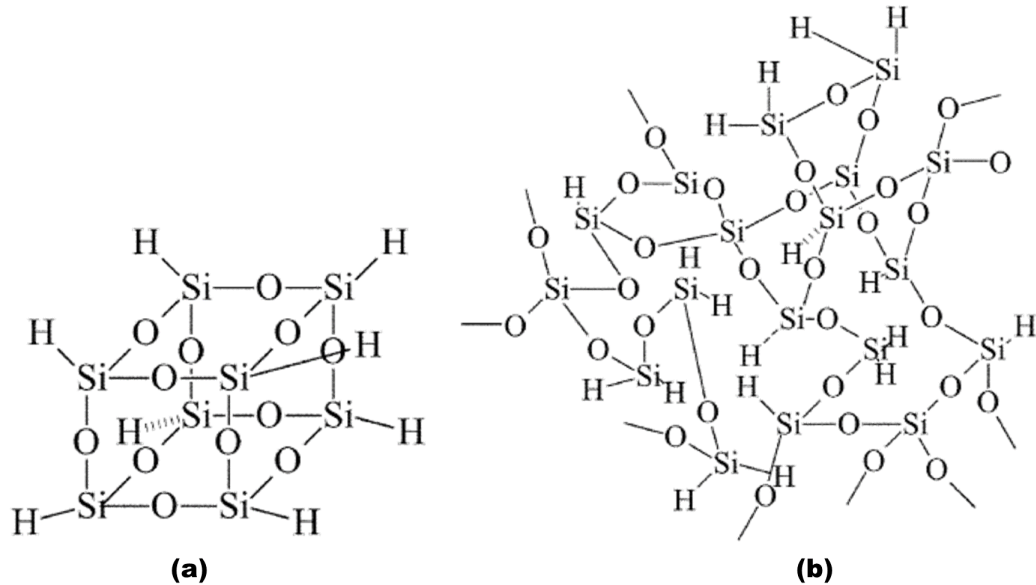


FIGURE 2.10: The chemical structure of HSQ; (a) Cage form and (b) network form.

The HSQ chemical structure can be seen in Figure 2.10 [57]. It has a cage-form chemical structure which mainly consists of Silicon(Si), Hydrogen(H) and Oxygen(O). When the resist is exposed to electron radiation, the Si-H bonds break, and a three-dimensional structure is created similar to that of Silica (SiO_2) [57].

In this work, HSQ was used as a high definition resist to define the silicon waveguides as shown in the fabrication process flow of Figure 2.2. The following procedure was followed:

1. The silicon sample is vigorously cleaned with acetone, 2-propanol (IPA), methanol and RO water. Each cleaning step takes place in an ultrasonic bath for five minutes, followed by drying-out with a nitrogen gun.
2. The initial cleaning is followed by a dehydration step at $180\text{ }^\circ\text{C}$ for five 5 minutes and 2 minutes of oxygen ashing at 100 Watt with a plasmaFab 505 asher.

3. A fresh solution of HSQ and MIBK (Methyl isobutyl ketone) is prepared with equal volumes of the two components.
4. The solution is spun on the sample at a speed of 2000 rpm for 60 seconds.
5. Following the spinning, the sample is baked at 95 °C for 15 minutes before being submitted to e-beam lithography. The parameters used for the e-beam lithography are summarised in table 2.1, while the dose varies depending on the age of the HSQ. The correct dose is found by running a dose test just before the submission of the sample.
6. After the exposure and prior to the development, the sample is baked at 180 °C for one hour. There are a lot of studies on the importance of post-baking before development as this improves the etching selectivity of the HSQ to the silicon [58] and the edge roughness of the mask [59]. During this work, a significant improvement was noticed by using a pre-development baking.
7. The final step is the development of the sample with TMAH at 21 °C for 30 seconds followed by a 1-minute rinsing in RO water and 30 seconds in IPA. Rinsing the sample in RO water is sufficient to remove residuals from the developer, but the additional rinsing in IPA was chosen as the final step due to its smaller surface tension. An optical and SEM inspection of the sample is always performed prior to the etching of the waveguides. The above-described process provides a mask with a height of 220 nm, which is sufficient to etch a silicon core with a thickness up to 400 nm.

The dose of the HSQ can vary depending on its age and the contamination of the bottle. Hence it is necessary to find the correct dose prior to any fabrication because the margin of error is quite small, as an underexposed resist will create a step to the waveguide after etching, while an overexposed resist will create sloppy waveguides. In both cases, both optical losses and light scattering will increase.

In order to obtain the correct dose, a specific pattern was designed that allowed to check various parameters. The main analysis consists of measuring the HSQ thickness following exposure and development. In fact, if the resist is underexposed, its thickness is lower than the spun thickness. With increasing dose, the height also increases until it reaches a maximum height that depends on the dilution, as shown in Figure 2.11. The optimum dose is at the point where the height

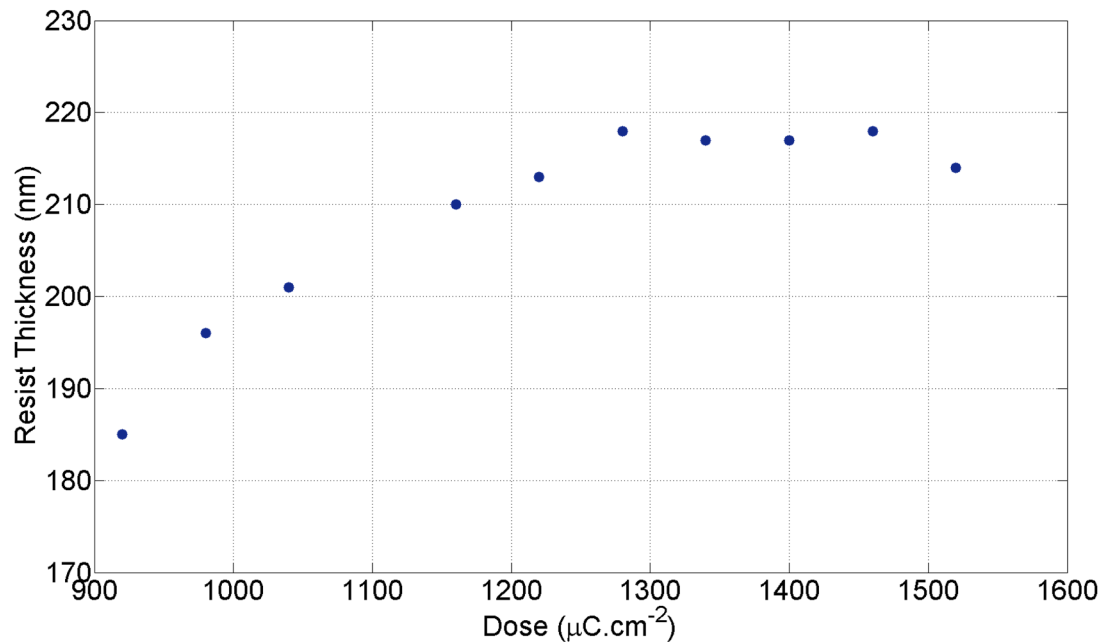


FIGURE 2.11: The thickness of the HSQ mask against the exposure dose.

saturates. Further to the height test, several other features are checked such as the clearing dose in small gaps, in large exposed areas and high-density patterns.

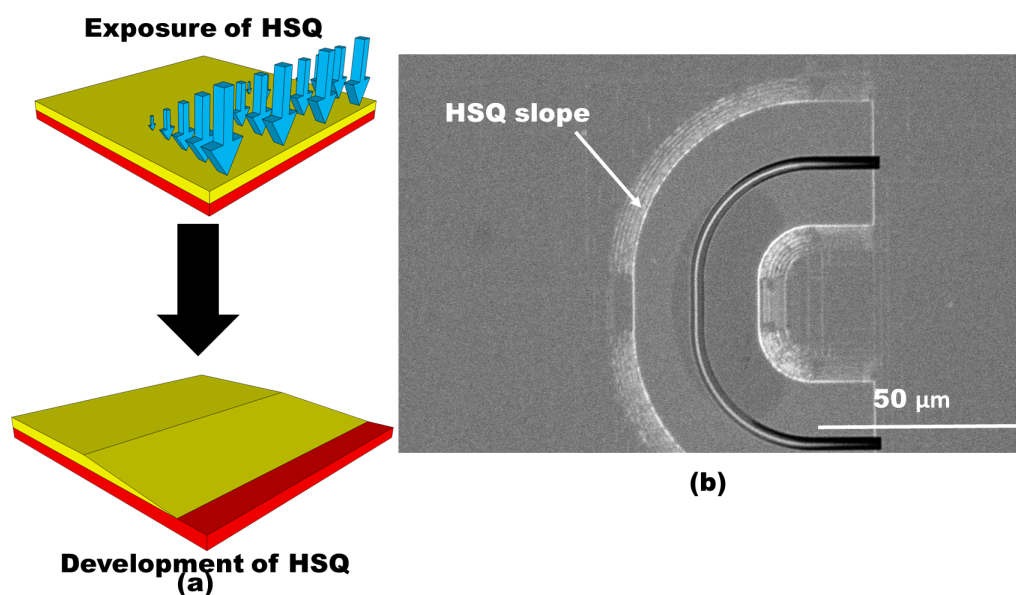


FIGURE 2.12: (a) Schematic of the process steps for the definition of an HSQ layer with a sloped profile (b) SEM image of a ring resonator with sloped HSQ profile on the edges.

The sensitivity of HSQ was used in the course of this project, to create passivation layers with sloped edge profiles (Figure 2.12a). This was achieved by adding a dose gradient on the edges of the patterns. Such passivation layers are of great

importance to provide a smooth profile transition for metallic layers and pads. In fact, a vertical and sharp edge of the passivation layer is not ideal as it might generate cracks in the metal that lead to poor electrical conductivity or a reduced lifetime. An example of a microring resonator with a metallic layer deposited in close proximity to the silicon waveguide is shown in Figure 2.12b. In this device, the metallic layer is partially deposited on the HSQ passivating layer and partially on the BOX cladding layer. The sloped edge profile of the passivating layer ensures the formation of a continuous metallic layer.

HSQ is one of the highest resolutions resists available in the JWNC, and it became one of the preferred options for the fabrication of sub-micrometre features. In particular, its low edge roughness and high verticality make it ideal for the fabrication of silicon optical devices. It is worth noting that photonic devices have a low pattern density and therefore negative resists provide a substantial reduction in the writing time. The main drawbacks of HSQ are its variability due to its receptiveness to ageing and environmental condition as well as its high cost.

Besides its excellent properties as an e-beam resist, HSQ is ideal for planarization as it can fill gaps as small as 3 nm [56] and can, therefore, replace PECVD silica which cannot uniformly fill gaps below 200 nm. When used as an upper cladding, HSQ is typically spun at 2000 rpm for 60 seconds followed by a bake at 180 °C overnight. Along bake at this temperature is necessary to ensure a chemically stable film and to obtain an effective index close to that of silica (i.e. 1.44 as opposed to 1.46). If higher temperatures are used, the refractive index can be lowered significantly [59].

2.4.2 ZEP-520A

ZEP is a high sensitivity and high-resolution positive resist with a high etching resistance. [60]. ZEP, likewise most positive resists, is easy to remove it from the substrate with organic solvents, which makes it ideal for shallow etching fabrication steps or for applications in which the patterns need to be completely uncladded. The basic process for ZEP, which is summarised in Figure 2.13, is as follow:

1. The sample is cleaned following the processes previously described.
2. A solution of ZEP and Anisole with a 2:1 ratio is spun on the sample at 4000 rpm for 60 seconds, followed by baking at 180 °C for 4 minutes.

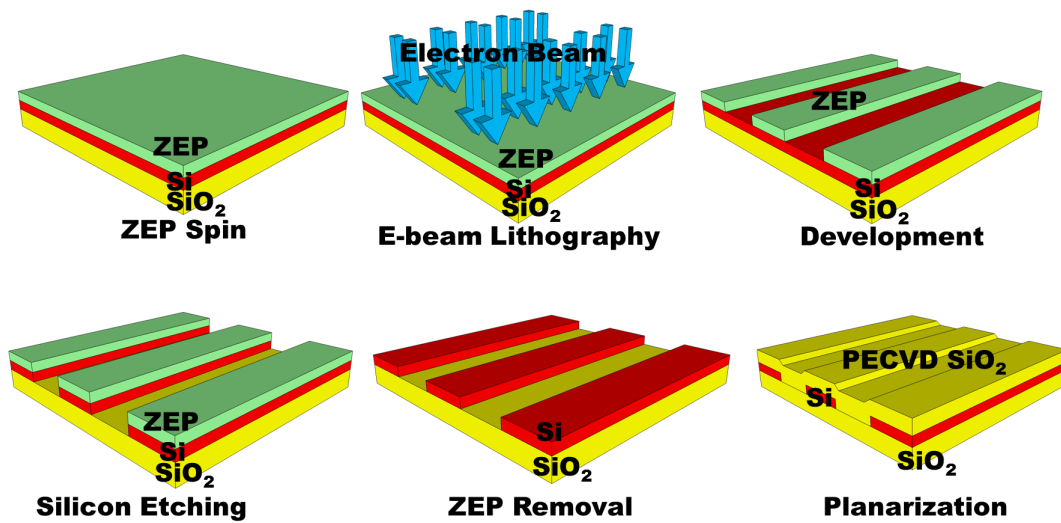


FIGURE 2.13: Schematic of the process steps for the definition of the guiding layer structures with ZEP resist.

3. The e-beam lithography is then performed with the parameters given in table 2.1 and a dose of $250 \mu\text{C}/\text{cm}^2$.
4. The sample is developed in O-xylene at 23°C for 30 seconds followed by a 1-minute rinse in IPA.
5. The sample is etched in an ICP RIE machine as described in Section 2.5.1.1 for the appropriate time depending on the required etching depth.
6. Finally, the mask is removed before further processing. In order to remove the mask, a 7-minute long oxygen ash is required at 150 Watt. To completely remove any residues of ZEP, the sample is left in a beaker with striper 1165 overnight at 50°C .

2.4.3 PMMA

PMMA (Poly(methyl methacrylate)) is a positive, medium sensitivity and low contrast resist [61], used for low-resolution patterns. As part of this work, PMMA was used for the deposition of the metallic layers for the alignment markers and heaters for thermal tuning of the waveguides. All the devices made with PMMA had a minimum feature size of 300 nm in width and spacing of at least $1 \mu\text{m}$ between adjacent features.

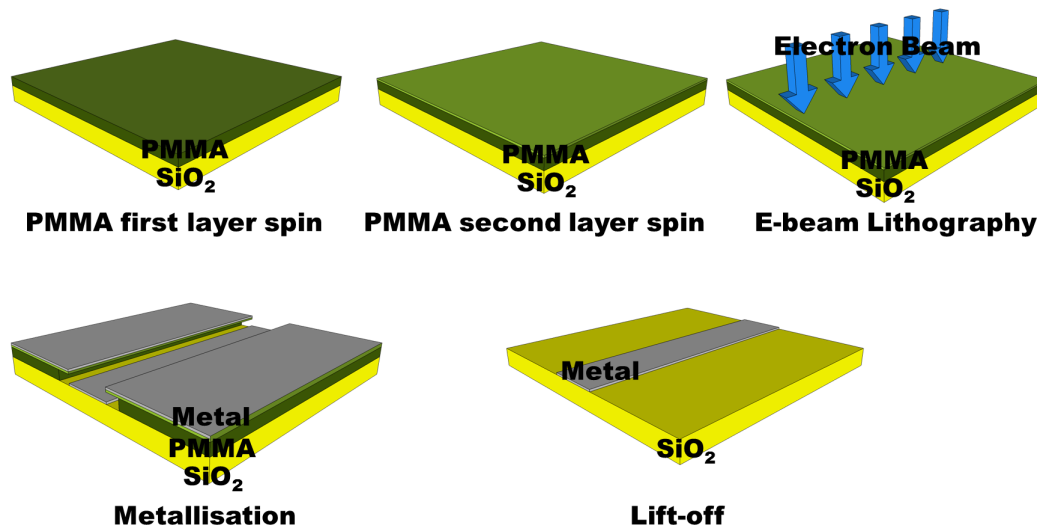


FIGURE 2.14: Schematic of the processing steps for the definition of the metallic layer structures with PMMA resist.

The main fabrication steps for the deposition of metallic layers with PMMA, which are schematically shown in Figure 2.14, are the following:

1. A layer of PMMA 2010 series 15 % is initially spun on the sample followed by a baking of 5 minutes at 150 °C.
2. The first layer is followed by the spinning of the second layer of PMMA 2041 4%, baked for 5 minutes at 150 °C. The difference between the two layers is their sensitivity, with the 2010 series having a greater sensitivity than the 2041 series. As a consequence, an undercut is created after e-beam exposure and development.
3. The sample is e-beam exposed with the parameters shown in table 2.1 and with a dose of 750 $\mu\text{C}/\text{cm}^2$.
4. The resist is developed with a solution of MIBK and IPA with a dilution of 1:1 for 30 seconds at a temperature of 23 °C followed by a 1-minute rinsing in an IPA solution.
5. The metal is deposited by electron metal evaporation, followed by a lift-off in a beaker with acetone at 50 °C for two hours.

2.4.4 SU8

SU8 is a negative photoresist [62], which in this work was used as an e-beam resist for the direct writing of large polymer waveguides. As an e-beam resist, it has very high sensitivity (i.e. a dose as low as $2.5 \mu\text{C}/\text{cm}^2$ is enough to expose the resist). On the other hand, the contrast of SU8 is very low, which poses a number of issues when writing polymer waveguides. An example is shown in Figure 2.15 where a dose of $2.75 \mu\text{C}/\text{cm}^2$ was used to expose the polymer waveguides and, as a result of the higher dose, the surrounding area is exposed as well. Figure 2.15b shows correctly exposed waveguides with a dose of $2.5 \mu\text{C}/\text{cm}^2$. Another disadvantage of the low contrast of the SU8 is the poor verticality of the waveguides if not correctly exposed.

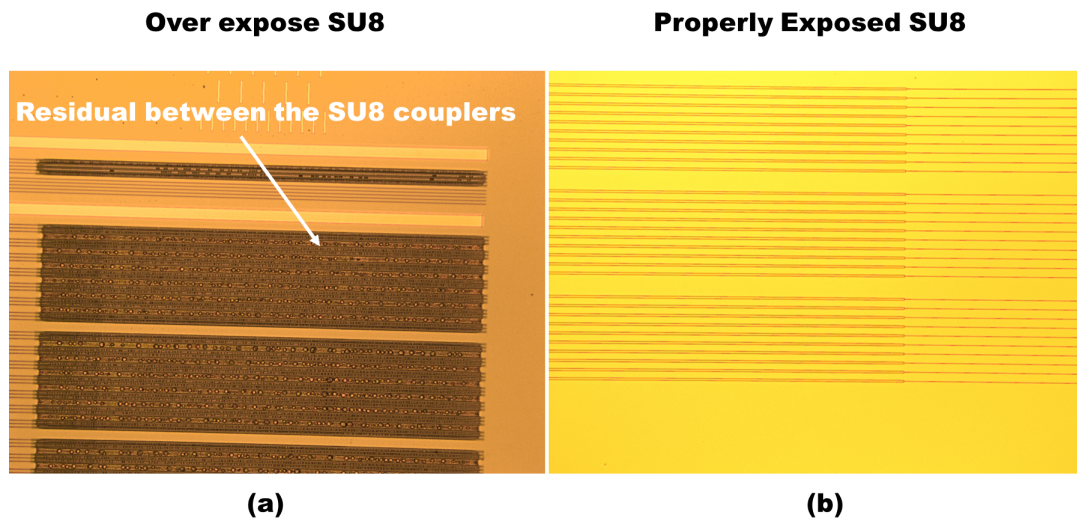


FIGURE 2.15: (a) Optical image of over exposed SU8 waveguides and (b) Optical image of properly exposed SU8 waveguides.

Even if the use of SU8 as an e-beam resist presents serious challenges, its low refractive index ($n_{\text{SU8}}=1.552$ [62]) makes it an ideal candidate for the fabrication of inverse taper polymer couplers, which are extensively used to reduce the coupling losses between the lens fibre and the silicon waveguides (see Section 3.2). The fabrication steps for the polymer waveguides were optimised as described below.

1. The sample is baked for 5 minutes at $180 \text{ }^\circ\text{C}$ as a dehydration procedure before the spinning of the resist.

Parameters	Parameters values
Resolution (nm)	1
Beam Size (nm)	2
Beam Step Size (nm)	40

TABLE 2.2: Electron Beam Parameters for the definition of the SU8 polymer waveguides.

2. A film of SU8 with the required height is spun on the sample at a speed of 7000 rpm for 30 seconds. The speed is increased gradually in order to ensure a uniform thickness of the film across the sample.
3. After the spinning, the sample is baked for 1 minute at 65 °C followed by baking at 95 °C for 2 minutes. A final bake of 1 minute at 65 °C concludes the process.
4. SU8 is e-beam exposed with the settings shown in table 2.2 and a dose of 2.5 $\mu\text{C}/\text{cm}^2$.
5. The sample is developed for 75 seconds in a beaker containing EC solvent and rinsed for 30 seconds in a beaker with IPA.
6. A hard bake of the sample at 180 °C for 2 hours is done as the last step before any further processing.

2.5 Dry Etching

The final step for the fabrication of optical waveguides is to transfer the defined pattern to the silicon core. If properly optimised, dry etching removes the unprotected material and only leaves a silicon layer below the mask which is a faithful replica of the pattern. Dry etching is preferred over wet etching because of the higher anisotropy and accurate control over the etching depth.

The most widely diffused dry etching technique is reactive ion etching (RIE), which accomplishes the removal of material through chemical and physical reactions induced by accelerated ions (radicals [51]). The main steps in a dry etching process are the following [51]:

1. Active gas species are produced from the gasses pumped into the chamber by an RF discharge. This process is driven by electron collisional dissociation and ionisation processes.
2. The active species are transported to the surface of the sample from the bulk plasma by diffusion.
3. Etching step
 - (a) Ion bombardment of the sample surface from the radicals and their adsorption on the surface.
 - (b) The absorbed active species, chemically react with the material to be etched.
4. The volatile byproducts of the etching are pumped out. This step is important since the byproducts can deposit on the sample surface and reduce the etching rate.

Although various RIE techniques have been proposed and implemented, Capacity Couple Plasma (CCP) RIE (relying on parallel plates) and Inductively Couple Plasma (ICP) RIE (relying on an inductive coil [51]) are the most popular. Both are available in the JWNC at Glasgow University.

- **CCP-RIE:** RF power of across two parallel plates which control the etching rate and the energy of the ions impacting on the sample. An increase of the power results in an increase in the etching rate but also increases the damage to the sample and the erosion of the mask (i.e. the selectivity decreases). It is possible to achieve high anisotropy with this technique as well as good selectivity if the recipe is properly tuned.
- **ICP-RIE:** The material damage due to the high ion bombardment energy is avoided with the ICP technique thanks to the use of two different RF powers for independently controlling the plasma density and the ion energy. The plasma is produced in a different chamber by biasing with RF power a copper coil placed around the chamber. The ions are directed towards the sample by a secondary RF power located at the back of the sample mounting, allowing for low ion bombardment energies. With this method, it is possible to achieve high anisotropy and good selectivity, as well as accurate control

over the etching rate by independently changing the RF powers of the two suppliers.

Because of the better performance in etching silicon waveguides with high verticality and low damage, ICP RIE was preferred to CCP-RIE etching. Most of the etching runs presented in this thesis were done with a STS-ICP from Surface Technology Systems (renamed SPTS technologies) [63]. At a later stage, a PlasmaPro 100 Estrelas deep silicon etch system from Oxford Instruments [64] became available in order to replace the obsolescent SPTS tool.

2.5.1 Silicon dry etching

The two most successful chemistries used to etch silicon are SF_6/O_2 [65–67] and SF_6/C_4F_8 [68, 69]. Without O_2 or C_4F_8 the etching is completely isotropic. The addition of oxygen in the first recipe reduces the plasma density, and a passivation layer is formed from the combination of silicon, fluoride and oxygen radicals. This passivation process improves the verticality of the etching profiles, although the etching rate is reduced and the mask suffers faster deterioration. The second chemistry also produces a passivation layer on the sidewalls of the waveguide thanks to the combination of the carbon and fluoride radicals. This reduces the chemical etching, and since no physical etching is taking place on the sidewalls (i.e. the radicals are bombarding the sample vertically), the sidewall damage is low. The main drawback of this chemistry is not in the process itself but on the fact that C_4F_8 is a greenhouse gas and hence its usage has to be limited where possible.

In this work, the SF_6/C_4F_8 chemistry was used on both etching tools and for all the fabricated devices. Some etching runs with SF_6 and O_2 were also performed, but results were not as good regarding verticality and roughness and hence no further development was performed.

2.5.1.1 STS etching

During the course of this work, most of the experimental samples were etched using a STS-ICP machine. The preferred chemistry was a mixed SF_6/C_4F_8 (a variation of the Bosch process [51]), which can offer low etching rates (150 nm/min), a high

selectivity between silicon and the HSQ mask (at least 3:1) and also a vertical profile as shown in Figure 2.16. The etching recipe was developed by previous users, and the etching parameters can be found in table 2.3. The verticality of the etching waveguides is as good as 88° and there is no significant roughness on the sidewall. The latter is of particular significance as an increase of the roughness in a high index contrast waveguide increases both the propagation losses and the polarisation rotation between the TE/TM modes [42]. Thanks to the sub-nm scale roughness and the good verticality, this specific etching recipe can provide record loss values of $< 1\text{dB/cm}$. [68].

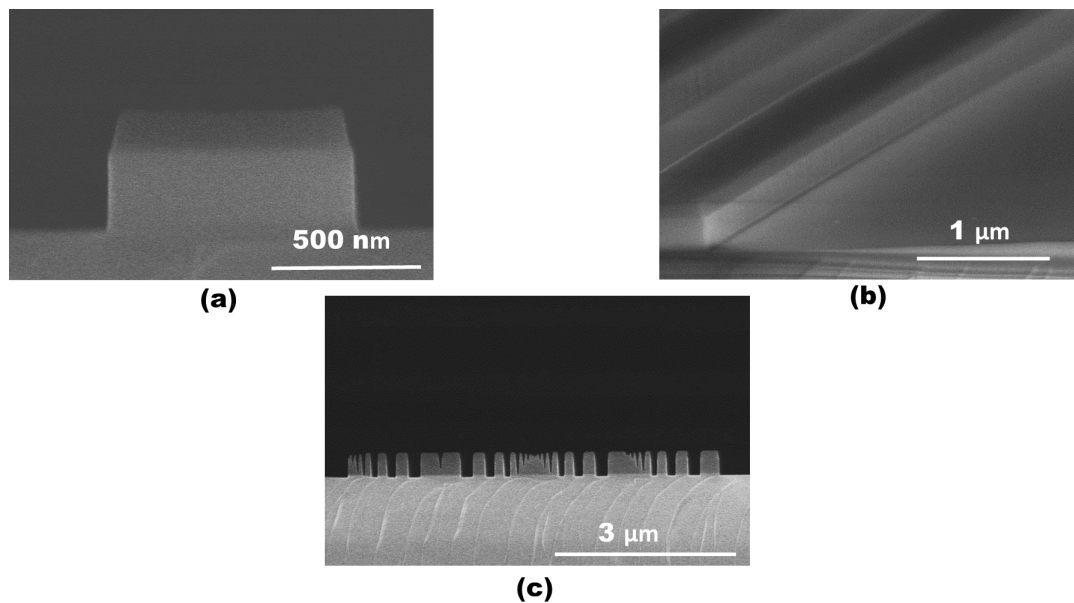


FIGURE 2.16: SEM images of (a) the profile of an etched waveguide, (b) the sidewall of the waveguide and (c) the gap clearance of the etching process using the STS.

A significant effort was devoted to assessing the etching profile and depth in small gaps and dense patterns as shown in Figure 2.16c. In particular, it is important to know the etching rates as a function of the gap size (especially below 100 nm), where the etching rate is reduced. This is particularly relevant to devices such as ring resonators coupled to bus waveguides and Bragg gratings, where the etched profile of 100-200 nm gaps has a significant impact on the performance of the devices. This phenomenon also known as RIE lag [70] - is a consequence of the limited volume of the gap that limits the flow rate of radicals. Hence extra etching time has to be allowed in order to clear the gaps completely. To calibrate the etching time as a function of the size of the structure, several test samples were etched for different times as shown in Figure 2.17.

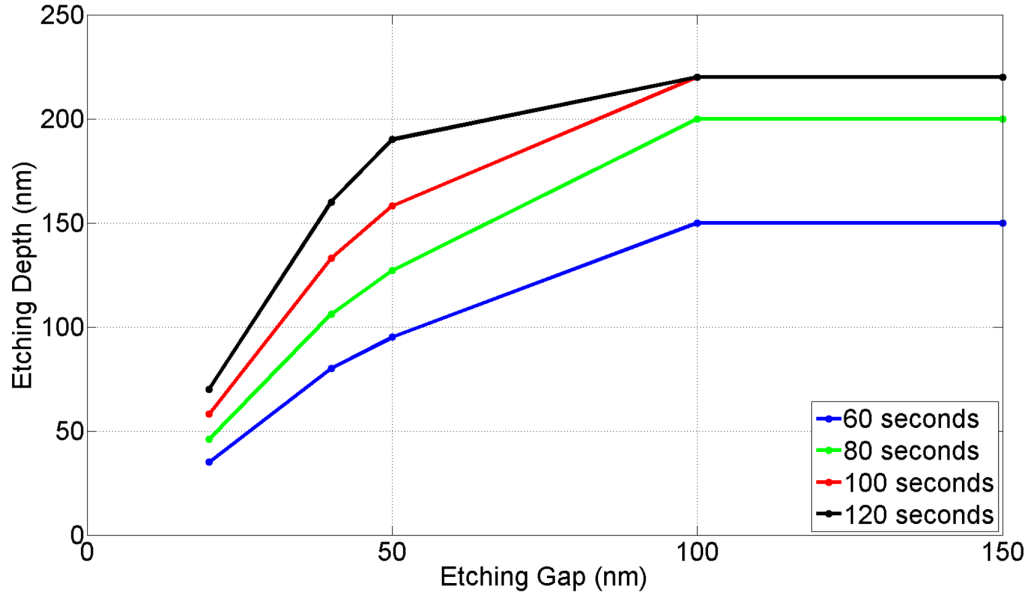


FIGURE 2.17: Dependence of the etching depth vs gap dimension in the HSQ resist mask.

Parameters	Value
Gas	SF_6 C_4F_8
Flow rate (sccm)	30 90
Plate Power (W)	12
Coil Power (W)	600
Pressure (mTorr)	9.8
Etching rate (nm/min)	150

TABLE 2.3: Silicon Etching Parameters for the optimal recipe in the STS ICP tool.

2.5.1.2 Estrelas etching

During the last year of this thesis, an attempt to transfer the silicon etching recipe to the new Oxford Instrument tool [64] was made. This work was motivated by the need for a backup machine for the silicon etching due to the ageing STS-ICP and the additional capabilities (such as the cryo etching) that are available on the Estrelas. Initially, three different etching recipes were investigated. The first was the original recipe developed on the STS with SF_6 / C_4F_8 chemistry, the second and the third were recipes based on SF_6 / O_2 chemistry under room and cryo temperatures (i.e. temperatures around -180 °C). Even though some initial test runs took place on the SF_6 / O_2 chemistry, it was not possible to develop a stable recipe due to time limitations and the unstable performance of the machine.

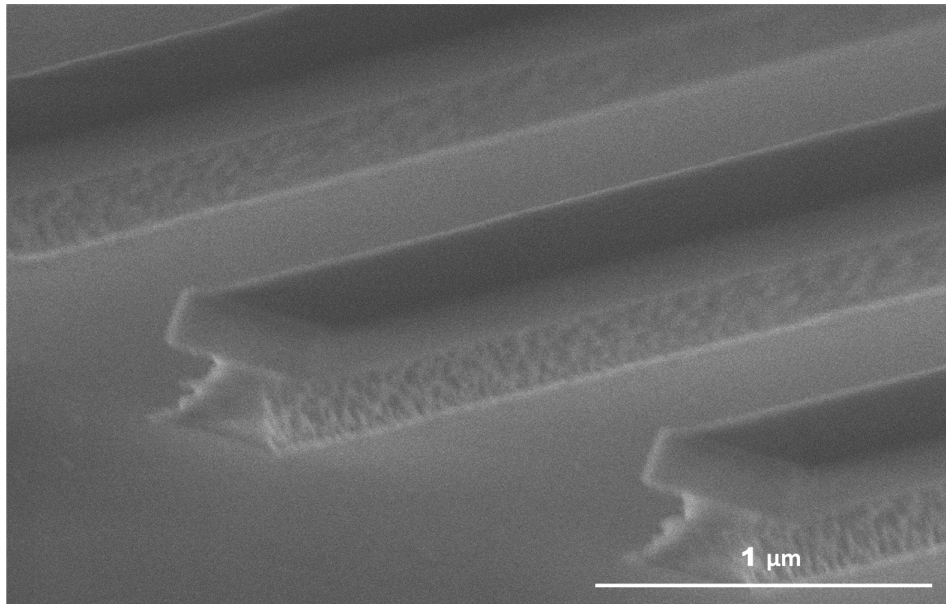


FIGURE 2.18: SEM images of the first etching on the Estrelas using the original recipe from STS

As for the transfer of the STS silicon etching to the Estrelas, the starting point was the original recipe shown in table 2.3. The resulting etching profile shown in Figure 2.18 is characterised by severe undercut and extremely high etching rates in the order of 440 nm/min. Furthermore, the ICP valve, which controls the pumping out of the byproducts of the etching, had to be opened at 100 % (rather than the recommended optimum of 25 %). As a result, it was not possible to accurately control the pressure of the etching and to ensure that all the by-products of the etching had been removed.

The substantial differences between the two machines found in the first etching run are most probably due to the following reasons: a) the chamber size is bigger in the Estrelas compared to the STS and hence it allows a larger expansion of the plasma. With the ions having higher kinetic energy, the pressure created in the chamber is higher and, at the same time, the by-products are pumped out at a smaller rate than in the STS. As a result, the pressure and the etching rate cannot be accurately controlled. b) Both machines can operate with either high frequency (HF) or low frequency (LF) plate power. For shallowly etched profiles in the order a few hundreds of nm the low-frequency option is preferred. The LF is typically applied in pulse mode, initially set to be 50 % on both machines. However, the Estrelas LF has a frequency that is double than the STS. This increases the concentration of fluoride radicals reaching the sample surface, hence the etching rate is much faster than in the STS machine. c) The much higher

energy of the Estrelas plasma reduces the formation of carbon fluoride polymer on the sample surface. As a result, the passivation of the sidewalls of the waveguide was not sufficiently fast to protect the surfaces from fluoride radicals and a severe undercut was produced.

In order to improve the etching, the pulse mode of the Estrelas was reduced to 25 % and, at the same time, the LF power was increased to attract enough radicals from the high energy plasma. Furthermore, the chamber set pressure was increased and the flow rate of the reactive gasses was reduced to allow better control of the chamber pressure.

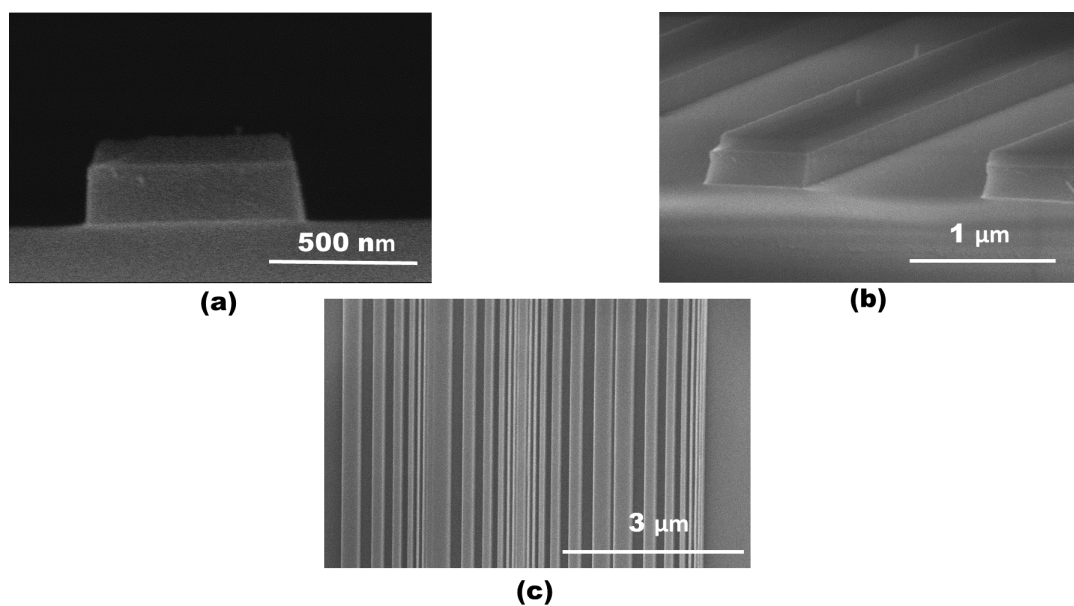


FIGURE 2.19: SEM images of (a) the profile of an etched waveguide, (b) the sidewall of the waveguide and (c) the gap clearance of the etching process using the Estrelas tool.

Following several runs to fine tune all the parameters, a final recipe was optimised as shown in table 2.4. The final etching consisted of two etching steps, an initial one with HF for a period of three seconds and the second one with LF for the remaining of the etching. The first step was a requirement of the machine to avoid damaging of the etching table. The etching rate was found to be lower than in the STS (110 nm/min as opposed to 150 nm/min) but still in acceptable range for accurately control the etching depth. Also, the selectivity of the process was not affected ($>2:1$ Si: HSQ).

The etching profile and the sidewalls roughness of the optimum recipe developed on the Estrelas can be seen in Figure 2.19a and 2.19b respectively. The verticality

Parameters	Step 1	Step 2
Gas	SF_6 C_4F_8	SF_6 C_4F_8
Flow rate (sccm)	15 45	15 45
Plate Power (W)	60 (HF)	25 (LF)
Coil Power (W)	600	600
Pressure (mTorr)	15	15
Etching rate (nm/min)	–	110

TABLE 2.4: Silicon Etching Parameters for the optimum recipe in the PlasmaPro 100 Estrelas.

of the sample is as good as 89° , which is comparable to the STS results, although a greater surface roughness is observed. The clearance in smaller gaps (<100 nm) is not as good as the STS etching (Figure 2.19c) but this can be easily improved by increasing the etching times.

A comparative measurement of the optical propagation losses in waveguides fabricated on the two machines was made. Two identical chips were patterned at the same time; one was etched on the STS and at the other on the Estrelas. Furthermore, in order to avoid the inaccuracies typical of the Fabry Perot method (see Appendix A), the cut back technique was used instead with spiral waveguides with length varying from 2 cm to 7 cm (see C). The losses for the STS etching were 3 dB/cm whereas for the Estrelas were 5 dB/cm for the Estrelas etching. This suggests that the additional sidewall roughness measured on the Estrelas etching have a substantial impact on the losses.

Further tests were made to improve the etching from the Estrelas with limited success. Although better sidewall roughness was achieved with lower pressure (down to 8 mTorr), without affecting the verticality, the etching rate was as low as 40 nm/min and the deterioration of the mask was too high. The selectivity of the silicon compared to the HSQ mask was below 1:1, which required the use of thicker masks which is not practical due to the unpractical aspect ratio between the mask thickness and the minimum pattern size. Further evaluation of the machine from Oxford Instrument is in progress in order to address different problems and improve the etching results.

2.5.2 PECVD Silica Deposition

One of the final steps of the fabrication requires the deposition of a thick buffer layer to protect the waveguides from the external environment and to optically separate the waveguides from the metallic layers used for the device tuning. A minimum distance of $1\ \mu\text{m}$ is necessary (see Section 3.1) in order to minimise the optical losses induced by the presence of the metallic layers. As discussed in the Section 2.4.1 a layer of HSQ provides uniform filling of very small gaps with a refractive index very close to that of silica. Although the HSQ spun on the sample can reach the required buffer layer thickness (i.e. the maximum HSQ thickness is $1.2\ \mu\text{m}$ [56]), the adhesion between the HSQ and the metal layers is not good. In fact, due to the very small surface roughness of the HSQ (measured at $0.5\ \text{nm}$), the metal layers tend to peel off easily. For this reason, a layer of silica deposited by Plasma Enhance Chemical Vapour Deposition (PECVD) was deposited on the top of the HSQ layer. The final process consisted of the first layer of HSQ with a thickness of $600\ \text{nm}$ followed by a $400\ \text{nm}$ -thick layer of PECVD silica.

PECVD is a method where the film is deposited at $300\ ^\circ\text{C}$ and the energy to dissociate the reactants is provided by microwave, photon excitation and RF power [71]. The plasma is created by an electric field accelerating free electrons inside the chamber where the precursors are delivered. The radicals are diverted towards the substrate where they form a stable film by reacting with the surface and creating chemical bonds. The deposition is characterised by two main factors:

1. The initial chemistry introduced in the chamber.
2. The energy is given to the system.

To optimise the quality of the deposited film, different variables must be taken into accounts such as the temperature, the RF power and the properties of the initial precursor. For this work, the standard recipe described in table 2.5 was used. The effective index of the deposited film was measured with an ellipsometry to be $n_{eff} = 1.461$.

Parameters	Value
Gas	SiH_4 N_2O N_2
Flow rate (sccm)	7 146 85
Power (W)	15
Temperature ($^{\circ}C$)	300
Pressure (mTorr)	1000
Deposition rate (nm/min)	30
Stress (MPa)	40

TABLE 2.5: Silica Deposition Parameters by PECVD.

2.5.3 ICP-CVD Silicon Nitride Deposition

In some applications, the deposition of a thick film of silicon nitride (Si_2N_3) is required. Specifically, silicon nitride is an interesting alternative to SU8 to fabricate input/output waveguides with large cross-section and can be used to induce a high level of stress to silicon waveguides. The latter is a technique that is currently being investigated to break the symmetry of the crystal and induce second-order non-linearities in silicon for a second harmonic generation. Some more details on the design of the waveguides are provided in the appendix. In order to deposit silicon nitride films with high quality, an Inductive Coupled Plasma Chemical Vapour Deposition (ICP-CVD) machine from Oxford Instruments [64] was used.

The differences between an ICP-CVD and a PECVD machine are similar to those of their etching machine counterparts (i.e. ICP and RIE). In fact, in an ICP-CVD tool, two different RF powers independently create the plasma and direct the radicals to the sample. Furthermore, low pressures and temperatures can be used for the deposition [72], allowing for low damage of the substrate and lift-off technique to be used.

The films deposited as part of this work are both low stress and a high-stress silicon nitride films with their deposition parameters given in table 2.6. The effective index of the film was measured with an ellipsometry to be $n_{eff} = 1.99$.

2.6 Conclusion

In this chapter, all the fabrication techniques required for the device fabrication presented in this thesis were introduced and analysed. Considerable time and

Parameters	Low stress	High stress
Gas	$SiH_4 N_2$	$SiH_4 N_2$
Flow rate (sccm)	7 6	7 6
ICP Power (W)	100	200
Platen Power (W)	0	10
Temperature ($^{\circ}C$)	25	25
Pressure (mTorr)	4	4
Deposition rate (nm/min)	30	30
Stress (MPa)	100	3000

TABLE 2.6: Silicon nitride Deposition Parameters with ICP-CVD tool.

effort were devoted to the optimisation of these processes as their impact on the design and performance of the devices can be substantial. The high quality and repeatability of the fabrication processing developed or optimised here allowed the development of several devices with state-of-the-art performance. In the following chapters, these devices will be presented from both a theoretical and experimental point of view.

A substantial effort has been spent on optimising the electron-beam HSQ process as it is one of the most important steps of the fabrication flow for silicon photonics. While the main process had been developed in previous works, and a lot of data already existed, in this work the process was fine-tuned for sub wavelength and critical dimension structures. Also, a recipe was developed for defining waveguides with the positive resist ZEP as an alternative process for shallow etched waveguides. Finally, the SU8 process for fabricating polymer couplers was optimised mostly with regards to the optimal waveguide dimensions.

As a future work, an improvement of the silicon etching is required, especially on the most recent Oxford Instruments machine available in the lab. In particular, it is critical to further reduce the roughness of the waveguide for lower optical losses and improve the repeatability and stability of the process. The cryo etching is an interesting venue to explore for the optimisation of the process. Also, techniques such as Atomic Layer Deposition (ALD) that became recently available in the JWNC can improve the passivation of the waveguide sidewalls [73]. Another area for future work is the improvement of the silicon nitride film with Low-Pressure Chemical Vapour Deposition (LPCVD) [74] which was added to the capabilities of the JWNC after the completion of this work.

Chapter 3

Component Design

Although high yield has been achieved in the fabrication of integrated silicon photonics as presented in the previous chapter, the dimensions of the devices are still at the limits of current fabrication technology. Any variation in device dimensions, even at the nanometer scale, might result in significant deviations from the designed behaviour. To mitigate such fabrication non-uniformity power-hungry tuning elements are often required.

Also, the submicrometer cross-section dimensions required for single mode operation causes substantial problems in coupling light into the system. In fact, while a silicon waveguide usually has a dimension of 500×220 nm, standard fibres have a typical spot size of $4 \mu\text{m}$ with the smallest single mode fibre having a spot diameter of $2.3 \mu\text{m}$. This size mismatch between the fibre and the silicon waveguide leads to high coupling losses.

In this chapter, an attempt to address these two issues will be made. Specifically, we will present the design and fabrication of efficient thermal heaters that can be used to tune the different components of a photonic chip. We will then discuss the optimisation of inverse couplers to increase the coupling efficiency of the silicon waveguides to optical fibres. Finally we will present results on the fabrication of sub-wavelength components. This approach increase the toolkit available to designers and can be of benefit to several applications such as non-linear optics.

3.1 Thermal tuning of silicon devices

3.1.1 Introduction

Reconfiguration of optical integrated components is usually required on most integrated components such as [75], delay lines [76], high-speed modulators and switches [77–79]. Among different techniques, the thermo-optic effect [16, 80–89] and electro-optic effect [77, 78, 90] have been the most widely used because of their compatibility with complementary metal-oxide-semiconductor (CMOS) fabrication process [90–92]. Electro-optic effects based on injection or depletion of free carriers offer high-speed modulation capabilities up to several tens of GHz [93] at the expenses of an increase in the optical losses [77, 78]. Such increase in losses makes EO effects unsuitable to tune or trim a large number of components. On the other hand, thermo-optic effects are of interest for large circuits as they don't introduce additional losses. However, due to the slow heat diffusion process on SOI, this technique has a low response time on the order of a few microseconds at best [79, 83].

In most of the works presented so far, the primary focus was on optimising heaters for low power consumption without too much emphasis on the modulation efficiency of the heater [87, 88]. In the following section, a theoretical and experimental work will be presented for the optimisation of the heater geometry for minimum power consumption and maximum tuning efficiency.

3.1.2 Thermo-optic effects in silicon

The thermo-optic effect is of great interest in silicon photonics due to the high thermo-optic coefficient of silicon ($\frac{\Delta n}{\Delta T} = 1.86 \times 10^{-4} K^{-1}$) and low expansion coefficient ($\alpha_{exp} = 2.6 \times 10^{-6} K^{-1}$) [94]. At the same time silica, which is the main cladding for the fabricated devices in this work, has nearly two orders of magnitude ($\frac{\Delta n}{\Delta T} = 6.53 \times 10^{-6} K^{-1}$) smaller thermo-optic coefficient, which ensures a very low thermal crosstalk across multiple components. Also, the similar expansion coefficient of silica makes the whole system very robust. On table 3.1 the expansion and thermo-optic coefficients for silicon and are reported.

Material	$\Delta n/\Delta T [K^{-1}]$	α_{exp}
Si	1.86×10^{-4}	2.6×10^{-6}
SiO_2	6.53×10^{-6}	6.7×10^{-6}

TABLE 3.1: Thermo-optic and expansion coefficients for Silicon and Silica. A difference of nearly two orders of magnitude is present between the two thermo-optic coefficients.

Upon application of heat on the silicon waveguide, a red shift is observed as given by the equation:

$$\frac{\Delta\lambda}{\Delta T} = \frac{\lambda_0}{n_{eff}} \frac{\Delta n}{\Delta T} \quad (3.1)$$

Where $\frac{\Delta\lambda}{\Delta T}$ is the shift of the spectrum in nanometers per degree Kelvin, λ_0 is the free space wavelength, n is the variation of the effective index due to the temperature change and n_{eff} is the effective index of the mode.

3.1.3 Heater configuration

For this work, a Mach Zehnder Interferometer (MZI) was chosen as the optical device to optimise the heater geometry. By integrating a heater on one arm of the MZI as shown in Figure 3.1a, the relative phase difference between the arms can be changed, which vary the power from the two output waveguides. From a measurement point of view, this is advantageous as a simple optical power measurement is sufficient to evaluate the phase change induced on the waveguide by the heater. Given a temperature difference ΔT on the waveguide, the phase change ($\Delta\phi$) is given by:

$$\Delta\phi = \frac{2\pi L}{\lambda_0} \frac{\Delta n}{\Delta T} \Delta T \quad (3.2)$$

Where L is the length of the heater and $\frac{\Delta\lambda}{\Delta T}$ is the shift of the spectrum in nanometers per degree Kelvin defined earlier. The power needed for a full π -shift is given by [86]:

$$P_\pi = \frac{H}{\tau} \Delta T_\pi \quad (3.3)$$

Where H is the heat capacity, τ is the thermal time constant of the system and ΔT_π is the temperature needed for a full π -shift.

ΔT_π can be easily calculated by setting $\Delta\phi = \pi$ in equation 3.1.3 and inserting the coefficient of Table 3.1:

$$\Delta T_\pi = 4167L^{-1} \quad (3.4)$$

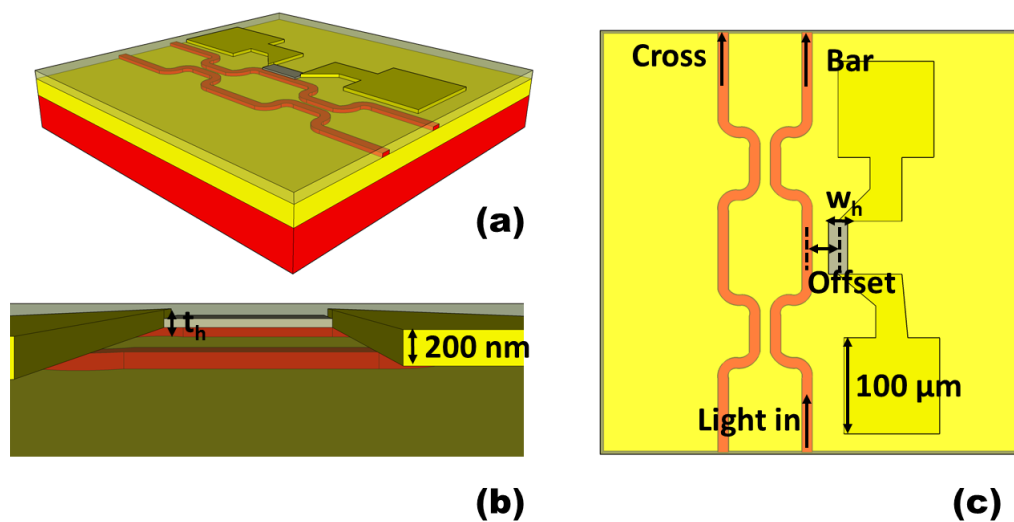


FIGURE 3.1: Schematic of a heater integrated on the arm of a silicon Mach Zehnder Interferometer. (a) 3D view, (b) Top view and (c) side view

In order to obtain good power efficiency, the first requirement is to use two metals with a high difference in their electrical resistivity to ensure that the majority of the power is delivered to the component to be tuned and not on the electrical pads and connections. For this work, a bi-layer of NiCr was used as the heating element and Au as the electrical contacts. The decision was made due to the very different electrical resistivity between the metals which is $1.1 \times 10^{-6} \Omega m$ and $0.02 \times 10^{-6} \Omega m$, respectively [95]. Due to the low resistivity and the very large size of the gold electrodes, the resistance of the pads was negligible compared to that of NiCr heaters. Although gold is an ideal electrical contact (i.e. low resistivity, high melting point, chemically inert), the adhesion between the upper silica cladding and the gold is poor, leading to low device yield. In order to address this problem, a thin layer of Ti was used as an adhesion layer between the silica cladding and

the gold contact. Considering the large difference in resistivities and thicknesses between the two layers, the current mainly propagates through the gold layer.

The optimisation of the heater geometry was divided into two parts. The first step was the optimisation of the cladding thickness between the silicon waveguides and the NiCr for maximum heat transfer and minimum optical losses. The second part consisted in optimising the heater geometry (thickness, width and offset from the waveguides as shown in Figure 3.1 for best power efficiency or maximum modulation. Both parameters cannot be optimised simultaneously as will be explained in the rest of this Section.

3.1.4 Upper cladding design

The silica top cladding plays a vital role in the performance of the integrated device and on the thermo-optic modulator fabricated on the top of it. An important point to consider is that silica is an excellent thermal insulator and, as such, is a major impediment for transferring the power produced by the heater to the waveguide. Therefore, silica claddings as thin as possible are always preferable to maximise the power efficiency. However, a too thin of an upper cladding increases the optical losses because of the stronger interaction of the optical mode with the metallic layer. Figure 3.2a shows the simulated temperature of a silicon waveguide as a function of the silica cladding thickness for a constant heater temperature of 75 °C. By varying the top cladding between 300 nm and 1.7 μm the efficiency of the delivered temperature decreases from 65 °C to 45 °C. These simulations were performed with a finite element method (FEM) from the commercial software COMSOL.

Figure 3.2b shows the theoretical losses for both the TE and TM mode for a cladding thickness ranging from 300 nm to 1.5 μm calculated with a finite difference eigenmode (FDE) method. As the TM extends substantially in the vertical direction, as expected, it is affected more from the presence of the metallic layer.

As a result, a compromise has to be found between the temperature delivery efficiency and the optical losses induced by the metal heater. Based on the graph in Figure 3.2b, for the negligible level of propagation losses (i.e. 0.1dB/cm), at least a 0.8 μm thick silica upper cladding is needed for the TE mode. This value increases to 1.3-1.4 μm for the TM mode. As the propagation losses are an essential

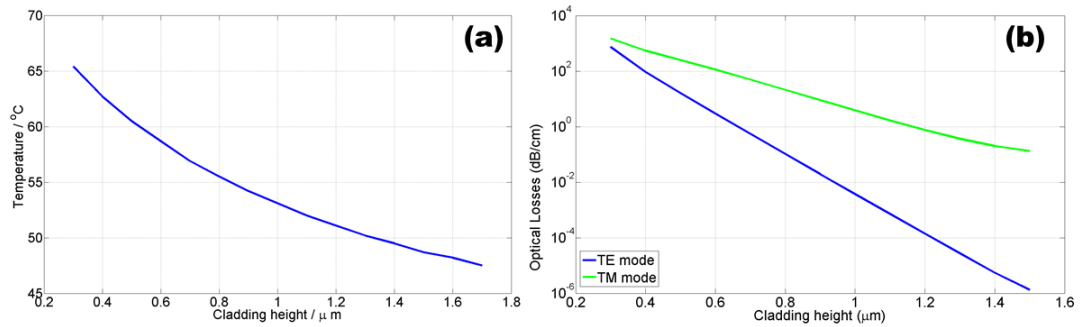


FIGURE 3.2: Simulations of the thermal and optical behaviour of a silicon waveguide with an integrated metallic heater as a function of the upper cladding thickness. (a) The temperature of the silicon waveguide against the height of the cladding, with a heater constant temperature of 75 °C and (b) the optical losses of the TE and TM mode due to the presence of a metallic layer against the thickness of the upper cladding.

aspect of any photonic device, a thickness of 1 μm was assumed as a standard for the rest of this work and the heater geometry was optimised based on this figure. It is worth noting that the large difference in propagation losses for the TE and TM mode in the presence of a metallic layer can be used to design effective TM absorbers as will be discussed in the next chapter.

3.1.5 Heating element geometry

The second part of the optimisation process is the optimisation of the heater geometry. A commercial software, COMSOL, based on a finite element method was used to simulate the heat flow and profile in the device. As the resistance of the gold pads is much smaller than that of the NiCr, it did not contribute to the overall heating of the waveguide, and hence it was not included in the simulations. In the optimisation process of the heater geometry, the thickness and width of the NiCr have varied as well as the offset of the heater with respect to the centre of the waveguide. The latter is of particular relevance in the presence of lithographic misalignments between the waveguide and heater layer. An example of such simulation is shown in Figure 3.3, which plots the thermal profile of two different heater thicknesses when the same current is applied. The same current in a thinner metallic film produces a higher current density and therefore a higher temperature. The temperature on the metallic layer/silicon waveguide is 110 / 71 degrees and 74 / 51 degrees for the 30 nm-thick and 50 nm-thick layers, respectively.

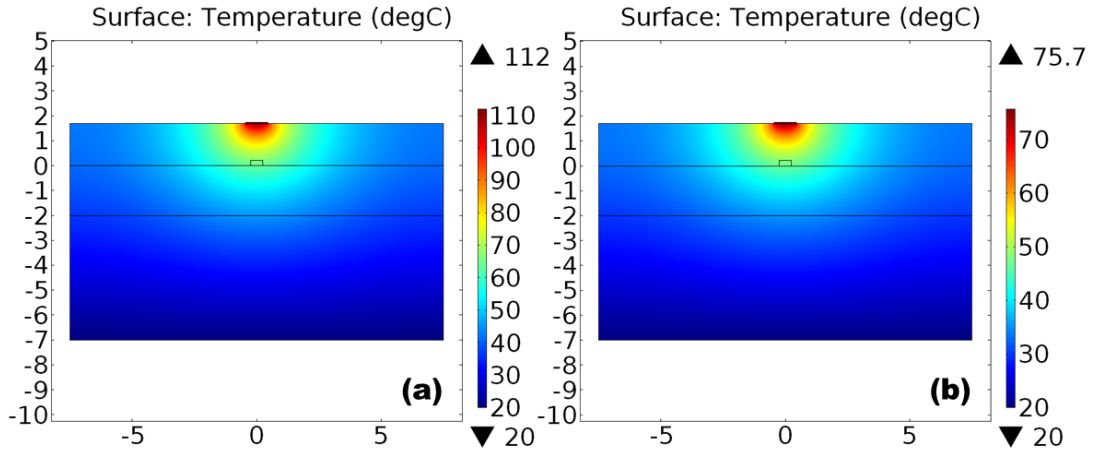


FIGURE 3.3: Temperature profile for the cross section of the device for a $w_h = 900$ nm wide and (a) 30 nm and (b) 50 nm thick heater when a constant current is applied.

The power dissipated by the heater element is given by the equation:

$$P = IV = \frac{V^2}{R} = V^2 \frac{w_h t_h}{\rho L} \quad (3.5)$$

Where I and V are the current and voltage applied to the heater, ρ is the resistivity of the NiCr, R is the resistance of the heater, and w_h , t_h and L are the width, height and length of the heater.

From the equation, a linear increase in the power consumption, and hence of the temperature, is expected by increasing the width or the thickness of the heater for a constant length. However, a linear increase in the temperature does not translate into a linear increase in the waveguide temperature because of thermal dissipation in the silica cladding. Figure 3.4 shows the waveguide temperature as a function of the heater width and for a fixed thickness of 50 nm. In these simulations, the heater temperature was kept constant for all the widths. The simulations indicate that the waveguide temperature saturates for a width of the heater exceeding $2 \mu\text{m}$. This can be better explained by the simulations of Figure 3.3, showing that the heat flow radiates in all directions, therefore, as the width of the heater becomes much larger than the waveguide width, most heat is dissipated on the side. The simulation was repeated with and without an HSQ overcladding above the heater, but no significant difference was found. Also, various thicknesses of the heater were simulated, but again no significant difference in the thermal behaviour of the waveguides was noticed. This was due to the limitation of the simulations that do

not take into account radiation losses or the influence of environmental conditions, which mostly affect thicker heaters. Therefore, in a real scenario, thinner heaters might provide a substantial performance improvement. Also, as shown in Figure 3.3, thinner heaters can produce higher temperature when the power input to the heater is kept constant, i.e. thinner heaters provide higher tuning efficiency defined as DT/DP

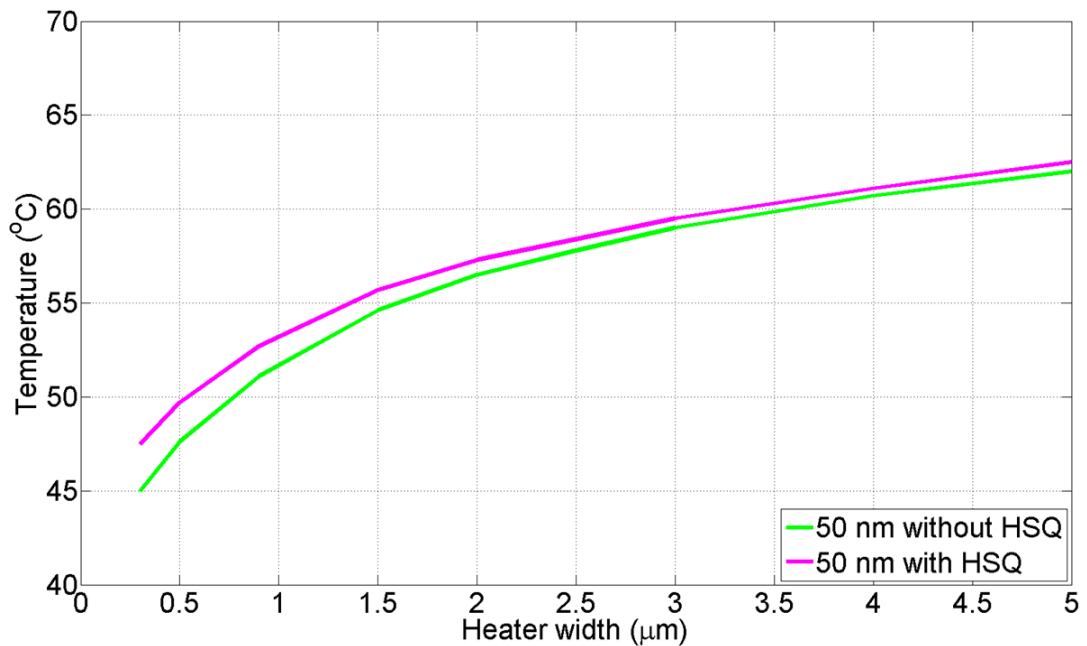


FIGURE 3.4: Waveguide temperature for different values of heater thickness and width, and for a constant temperature of the heater. Silicon waveguide temperature without any HSQ on the top of the heater (green line) and with HSQ on the top (purple line) for the same heater thickness.

From equation 3.2, the maximum phase shift occurs with the highest temperature difference on the waveguide. However, the most power efficient heater, is the one which requires the least amount of power for a full π -shift, i.e. has the maximum wavelength shift per unit power which is given by the equation:

$$\frac{\Delta P}{\Delta \lambda} = \frac{\Delta V^2}{R_h \Delta \lambda} = \frac{w_h t_h}{\rho L_h} \frac{\Delta V^2}{\Delta \lambda} \quad (3.6)$$

Figure 3.5 shows the required power for a full π -shift as a function of the heater width and thickness. The most power efficient heater geometry has a width around 900 nm and thickness as small as practically possible. However, thin heaters lack long-time stability and robustness due to the non-uniformity of the film thickness. Therefore, it was decided to keep the minimum thickness at a safe value of 50 nm.

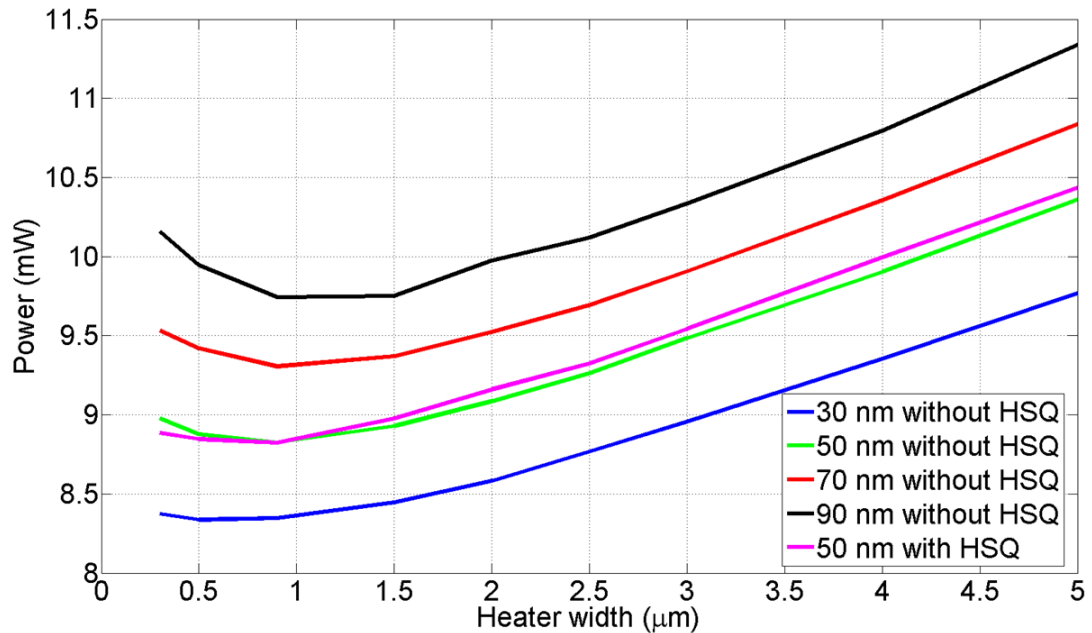


FIGURE 3.5: Tuning efficiency dependence on the heater thickness and width. As for the previous simulations the presence of HSQ on the top of the heater has a negligible effect.

3.1.6 Mach Zehnder Interferometer (MZI) tuning

Following the theoretical study, an experimental investigation was done using MZIs as discussed above. The devices were fabricated as described in Chapter 2 and the thickness of the NiCr was chosen to be 50 nm. A series of optical devices were assessed with varying both the thickness and the distance of the heating element from the waveguide. An identical set of devices was fabricated with a HSQ protecting layer above the NiCr, as corrosion issues have been seen in the past. The output signal of a fabricated MZI is shown in Figure 3.6 against the heater power.

From the graph, it is possible to extract the power needed to obtain a full π -shift for a specific heater width. For this analysis, only the first oscillation of the output fringes was used. Figure 3.7 shows the experimental data for the power needed for a full π -shift against the width of the heater without (blue line) and with (green line) an overcladding of HSQ. The optimum width for the most power efficient heater is in both cases around 1 μm , which is an excellent agreement with the simulations.

From the simulations and the experimental data, no significant difference was found between heaters without and with HSQ overcladding. However, previous

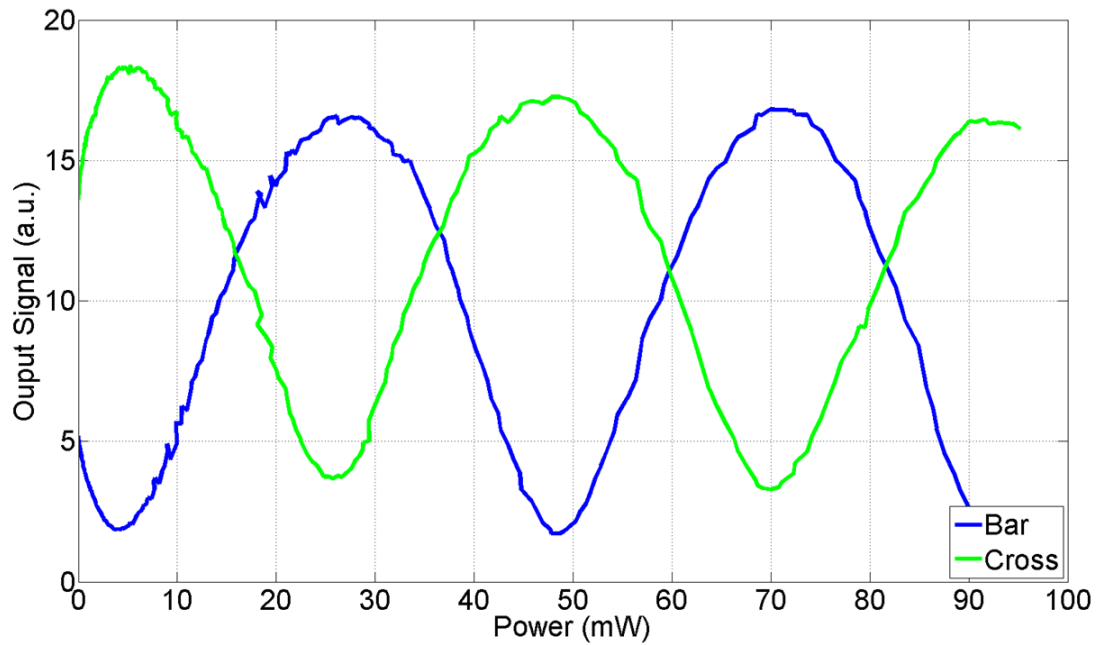


FIGURE 3.6: The output signal of a MZI for both the bar and the cross outputs as a function of the heater power

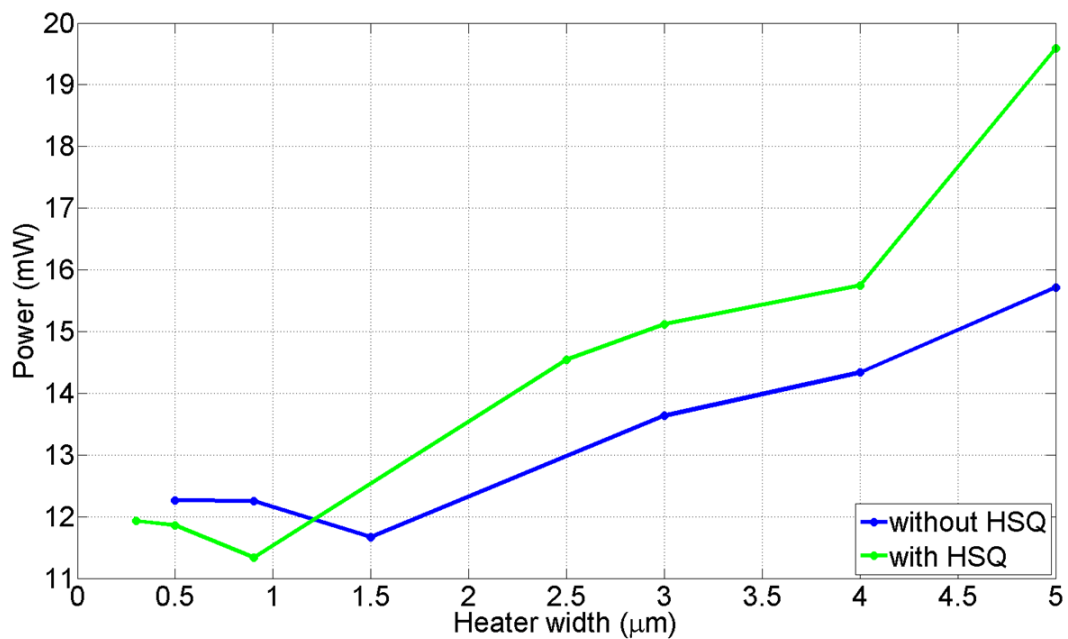


FIGURE 3.7: Heater tuning efficiency as a function on the heater width, without (blue line) and with (green line) HSQ on the top.

experimental data indicated a long-term degradation of the heater performance; hence an HSQ overlidding was always deposited above the NiCr heaters. From both the experimental data and the simulations it was found that the best power efficiency is obtained with a width 900 nm.

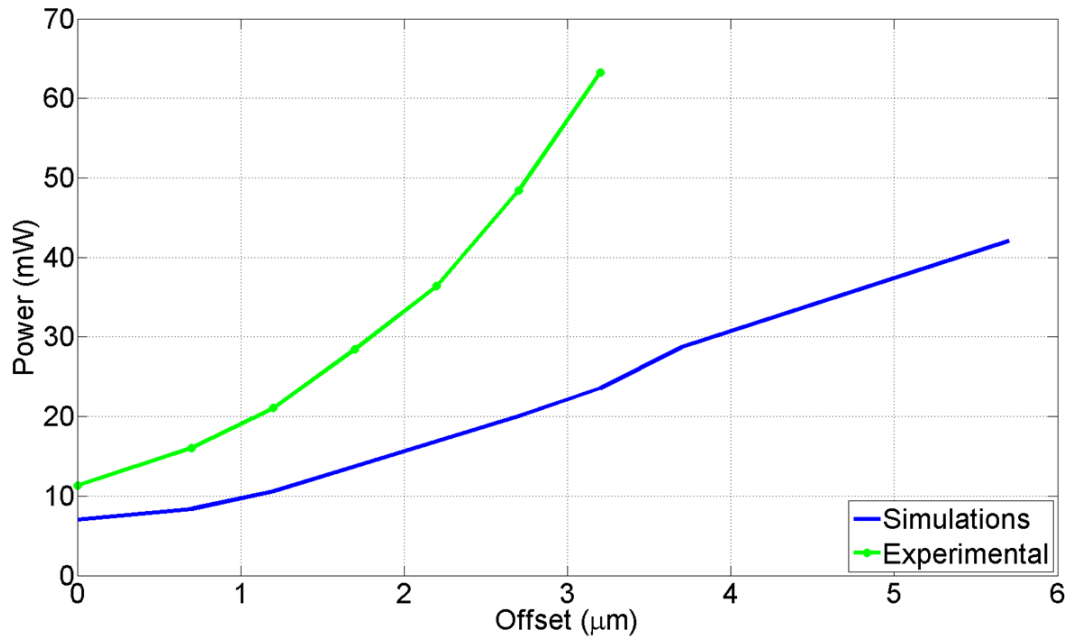


FIGURE 3.8: Heater tuning efficiency as a function of the heater offset from the waveguide, for theoretical (blue line) and experimental (green line) results.

Because it is not always possible to have the heater centred above the waveguide due to fabrication error from the e-beam misalignment between different lithography steps (see Section 2.3), a deliberate offset was introduced between the centre of the waveguide and the heater as shown in Figure 3.1c. This investigation was done by both simulation and experiments, the results of which are shown in Figure 3.8. As expected, the power required for a π -shift increases with the offset between the heater and the waveguide. The difference in the power between the simulated and measured data is due to the power consumption of the electrical probes and the gold pads, which were not taken into account in the simulations.

3.2 Inverse tapers couplers

3.2.1 Introduction

The high refractive index contrast between silicon and silica enables the fabrication of photonic devices with dimensions as low as a few hundreds of nm. However, such compact dimensions translate into a large modal mismatch between optical fibres and the silicon waveguides. In fact, the core of a fibre is several μm in diameter whereas the waveguide cross section is at least an order of magnitude smaller. This

results in high coupling losses as well as in the requirement for extremely accurate mechanical micromanipulators or expensive packaging solutions.

Different groups have taken different approaches to tackle the coupling to and from silicon chips. The most popular geometry is the grating coupler [98], in which vertical coupling occurs between surface gratings defined at the extremities of the waveguides and optical fibres that are vertically coupled to the chip. Even though gratings couplers have high coupling efficiency, they are wavelength and polarisation dependent and require a quite complex fabrication process of the grating to minimise the coupling into the substrate [99]. Another approach is to adiabatically taper up the silicon waveguide on the edges of the chip so as to enlarge the mode and improve the modal matching to the optical fibre [100]. This can be achieved with a single fabrication step but only yields a marginal performance improvement.

At Glasgow, we decided to use an inverse taper approach where a polymer waveguide (Figure 3.9) is interposed between the optical fibre and the silicon waveguide [101]. A schematic of the coupler is shown in Figure 3.10a. Improved geometries make use of 3D polymer tapers [102] where the polymer is tapered down in all directions to optimise the matching with the silicon waveguide. The best reported results show coupling losses of the order of 0.36 dB and 0.66 dB for TM and TE, respectively [103].

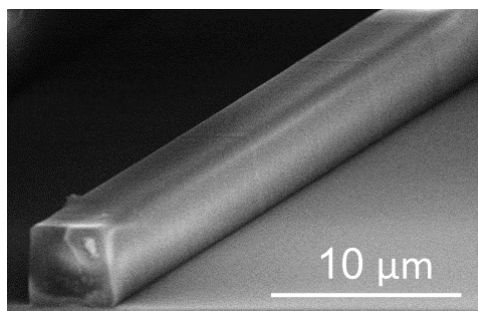


FIGURE 3.9: SEM image of a cleaved SU8 polymer waveguide.

This section will discuss the work performed to optimise the polymer couplers used in our silicon devices, which exhibited losses as high as 10dB. This high value was a combination of a non-repeatable thickness of the polymer and a non-optimal polymer cross-section. SU8-3005 was used for the polymer waveguide since its refractive index of 1.552 [62] offers sufficient optical confinement when clad with silica (which has a refractive index of 1.46). The typical polymer cross-section was $2\ \mu\text{m}$ in thickness and $2.5\ \mu\text{m}$ in width. Both simulations and

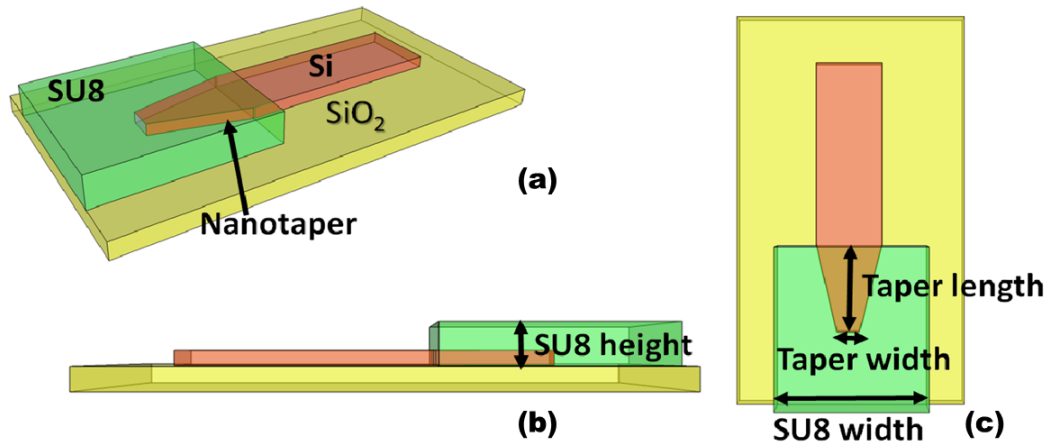


FIGURE 3.10: Schematic illustration of a polymer coupler with an inverse taper (a) 3D view, (b) Top view and (c) side view.

results in the literature suggested that larger waveguide dimensions of at least $3.5 \times 3.5 \mu\text{m}$ [103] are a better option for low loss coupling.

Initial experimental work was performed to obtain a uniform and repeatable thickness of SU8-3005. Samples were spun at different speeds and then exposed with photo-lithography in order to calibrate the polymer height. This was followed by different baking temperatures and times and cleaning procedures to obtain repeatable results. The final optimised fabrication process for the polymer waveguides can be found in Section 2.4.4. Following the film optimisation, a theoretical analysis was performed to obtain the best geometry for the inverse taper polymer couplers. The work was divided into two sections: The first part was the optimisation of the polymer waveguide geometry, while the second investigated the dimensions of the inverse tapers.

3.2.2 Polymer Waveguide Geometry

The optimisation of the polymer waveguide was performed with a commercial software, Lumerical Mode solutions, based on Finite-Difference Eigenmode (FDE) and Eigenmode Expansion (EME) solvers as described in Appendix B. The standard technology at Glasgow university consisted of a polymer waveguide with a cross section of $2 \mu\text{m}$ in thickness and $2.5 \mu\text{m}$ in width. At those dimensions, as seen in Figure 3.11a the mode of the waveguide is strongly interacting with all the sides of the waveguide.

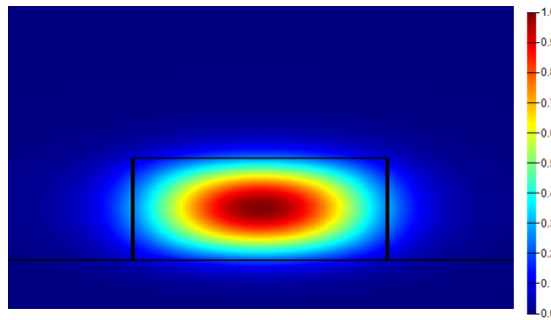


FIGURE 3.11: The fundamental TE mode of the polymer waveguide with a width of $2.5 \mu m$ and height $2 \mu m$.

Figure 3.12 shows the effective index of a SU8 waveguide for the TE mode against the polymer width and various thickness. As expected, the effective index of the original polymer waveguide cross section is very close to the refractive index of silica and hence to cut-off. As the polymer width and thickness increases, the effective index also increases, and lower losses are expected as shown in Figure 3.13.

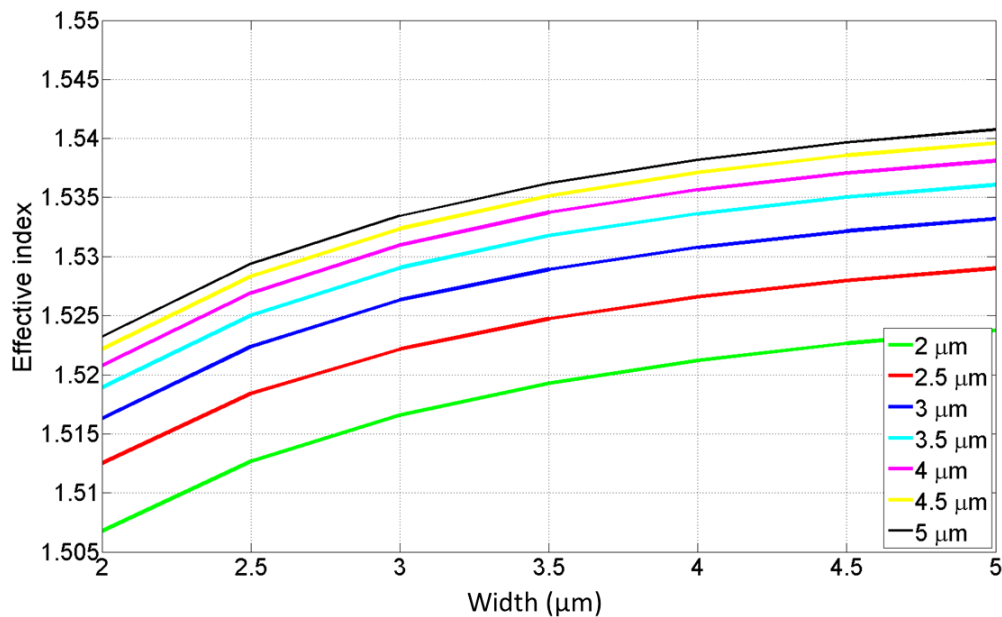


FIGURE 3.12: The effective index of the fundamental TE mode against the width of the polymer waveguide and for different heights.

The theoretical propagation losses of the SU8 waveguide are of acceptable level (a few dB/cm) for height and width above $3.5 \mu m$, while they are not improving significantly above $4.5 \mu m$. This is expected based on literature review where the best results were demonstrated on waveguides with a cross-section of $3.5 \times 3.5 \mu m$

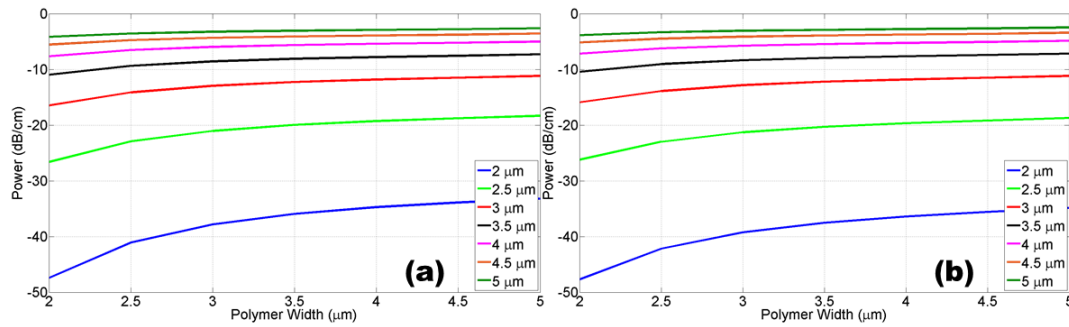


FIGURE 3.13: The optical losses of the fundamental (a) TE and (b) TM mode against the width of the polymer waveguide and for different heights.

[103]. From the initial film optimisation, a thickness of $3.5 \mu\text{m}$ can be accurately obtained with a thickness variation of $\pm 200 \text{ nm}$ across a chip of $30 \times 30 \text{ mm}$.

A square cross-section of the waveguides should be avoided to minimise the coupling between the TE and TM polarised modes. Furthermore, the thickness of the waveguide should not exceed $3.5 \mu\text{m}$ to avoid multi-mode propagation. Therefore, the optimal polymer waveguide should have a thickness of $3.5 \mu\text{m}$ and a width of $4 \mu\text{m}$.

3.2.3 Inverse taper

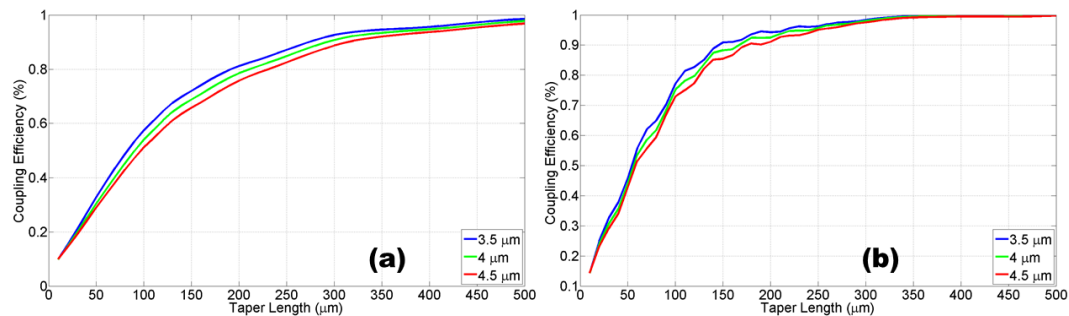


FIGURE 3.14: Simulation results of the transmitted power against the length of the taper for constant polymer height and different polymer widths for the (a) TE and (b) TM mode.

In an efficient coupler, all the optical mode travelling inside the polymer waveguide has to be coupled to the silicon waveguide. This is achieved by adiabatically decreasing the effective index of the mode propagating in the silicon waveguide through an inverse taper in order to match one of the polymer waveguides. The taper has an initial width equal to that of the silicon waveguide and then adiabatically decreases to a width of 20 nm .

Simulations were performed with an EME solver in order to reduce the simulation time. Figure 3.14 shows the percentage of the energy of the (a) TE and (b) TM mode coupled into the silicon waveguide as a function of the length of the taper from a SU8 waveguide with height of $3.5 \mu\text{m}$ and widths of $3.5 \mu\text{m}$, $4 \mu\text{m}$ and $4.5 \mu\text{m}$. For the chosen dimensions of the polymer, a taper with a length between 200 to $300 \mu\text{m}$ is required to maximise the power coupling into the silicon waveguide. The modulation is observed in Figure 3.14b, are due to simulation inaccuracies. With a high number of monitors this modulation can be removed at the price of longer simulation times (see Appendix B).

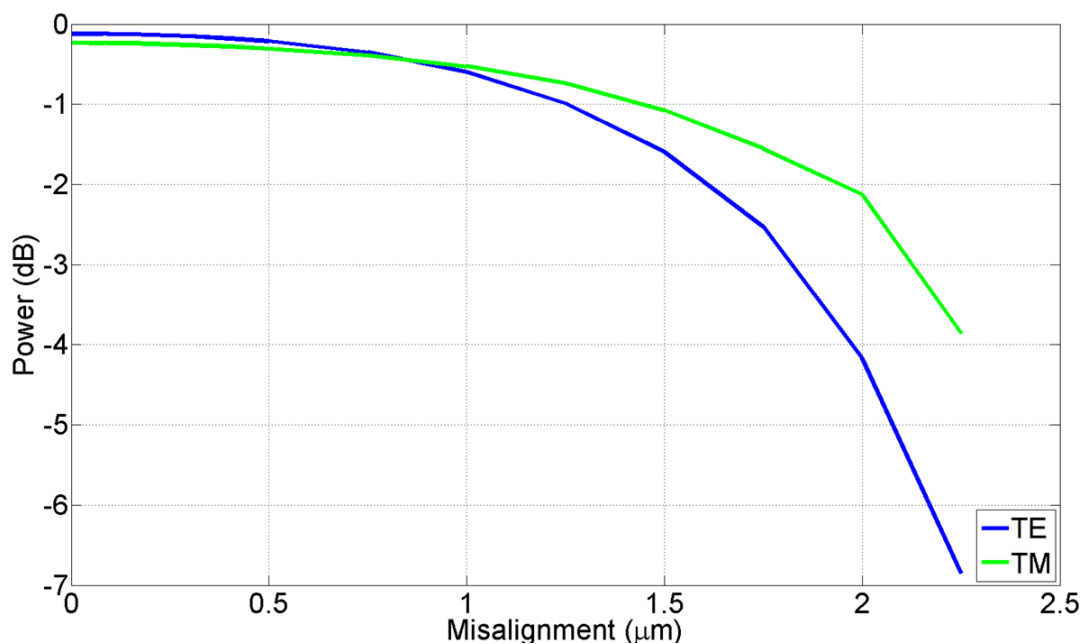


FIGURE 3.15: Simulation results of the optical losses against the misalignment between the inverse taper and the polymer waveguide for the TE (blue line) and TM (green line) mode.

Although the fabrication of silicon photonics is well established in the JWNC, fabrication errors due to the drift of the e-beam lithography (see Section 2.3) can introduce misalignments between the silicon and polymer waveguides, which can cause additional coupling losses. Figure 3.15 shows the extra theoretical losses induced by a misalignment between the polymer and the silicon waveguide for the TE (blue line) and TM (green line) mode.

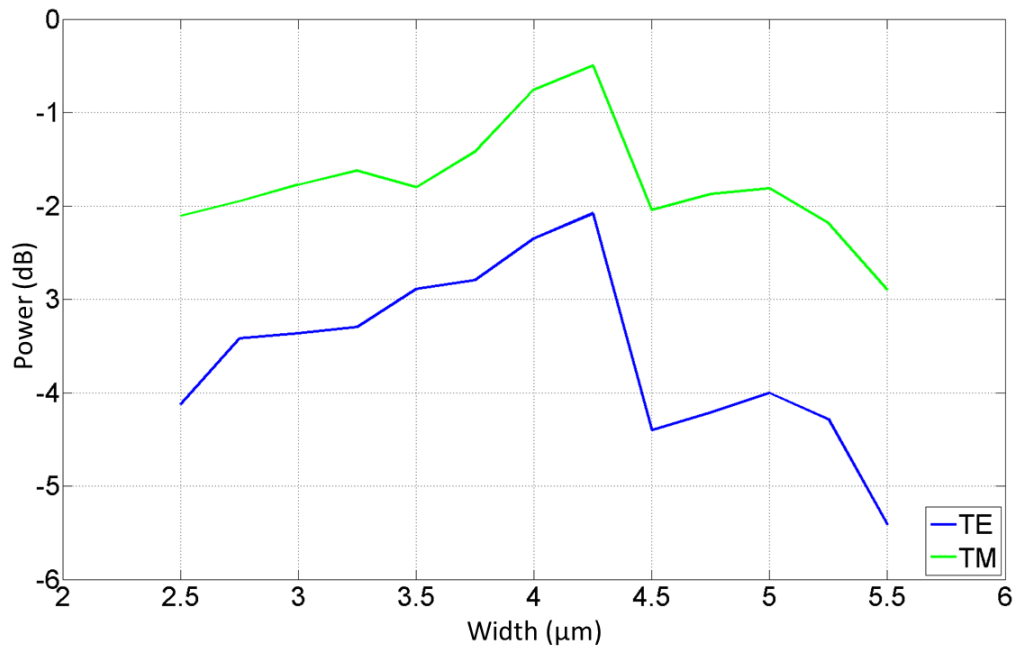


FIGURE 3.16: The optical losses of the TE (blue line) and TM (green line) mode against the width of the polymer waveguide.

3.2.4 Experimental data

Because the misalignment is unlikely to exceed a few hundreds of nm, the additional losses are negligible (i.e. 0.1-0.2 dB) compared to the other losses such as coupling and propagation losses. However, this misalignment breaks the lateral symmetry of the system and can, therefore, induce substantial polarisation rotation between the TE and TM mode. This effect, which will be analysed at the end of this section, is far more detrimental than small additional losses.

An experimental study was done to investigate the performance of the polymer couplers and confirm the results of the simulations. Two individual set of devices were fabricated. The first set was designed to examine the optimum width of the polymer waveguide with a constant thickness of $3.5 \mu\text{m}$ (the actual thickness was measured to be $3.7 \mu\text{m}$). Figure 3.16 shows the coupling losses as a function of the width of the polymer waveguide for the TE (blue line) and TM (green line) mode. The insertion losses decrease with increasing width, with the minimum found at a polymer width of $4 \mu\text{m}$. Above this width the waveguide becomes multimode, and the losses increase. This behaviour is in excellent agreement with the simulation that suggests an optimal width of $4 \mu\text{m}$.

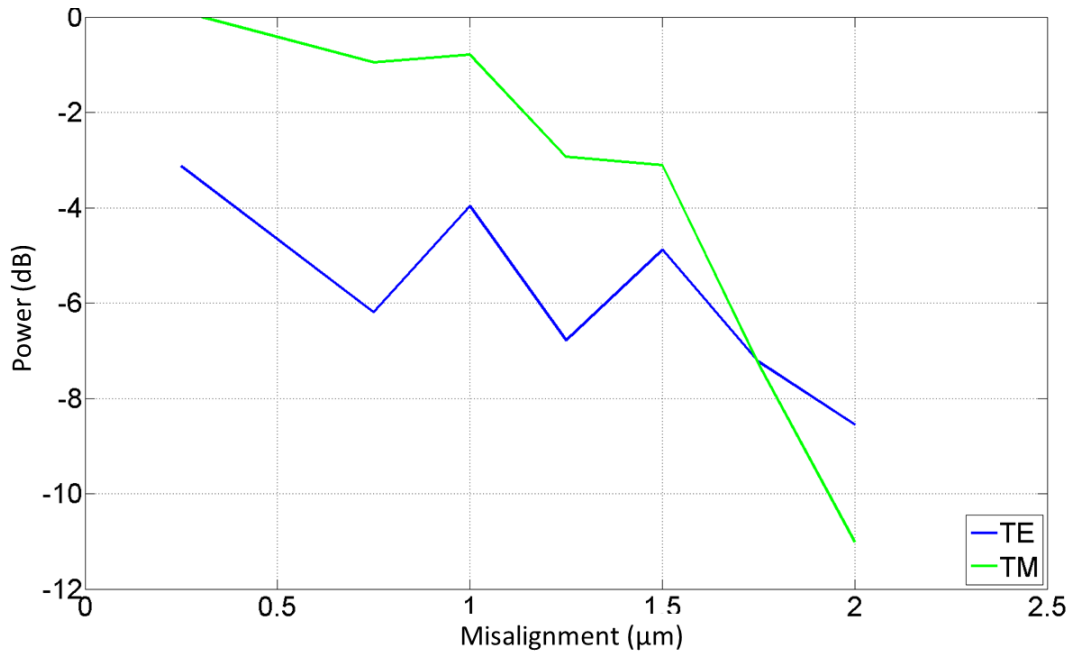


FIGURE 3.17: The optical losses against the misalignment of the inverse taper with respect to the polymer waveguide for the TE (blue line) and TM (green line) mode.

For the second set of devices, the inverse taper was intentionally misaligned with respect to the output polymer waveguide only, i.e. the input polymer waveguide was kept aligned to the centre of the silicon waveguide. Having only one of the two sides misaligned allow measuring the extra losses per facet more accurately and any possible polarisation conversion due to symmetry breaking. All the devices were fabricated with constant polymer height and width of $3.5 \mu\text{m}$ and $4 \mu\text{m}$ respectively. However, because the control of the SU8 thickness is critical, the actual polymer waveguide was 300 nm thicker than designed, which led to multimode operation.

Figure 3.17 shows the extra losses of the system due to the misalignment between the inverse taper and the polymer waveguide for the TE (blue line) and TM (green line) mode. As expected the losses increase with increasing misalignment, while some unexpected values for the TE mode are due to the multimode nature of the waveguide.

Finally, the polarisation rotation inside the polymer waveguide due to the misalignment of the taper was measured with the use of a polarimeter, and the results were plotted in a Poincaré sphere as shown in Figure 3.18 for a wavelength $\lambda = 1500 - 1600 \text{ nm}$. The measurements refer to a set of devices where the misalignment between the taper and the polymer waveguides was increased from 0 to $2 \mu\text{m}$ in increments of 250 nm (devices with 250 nm misalignment were not

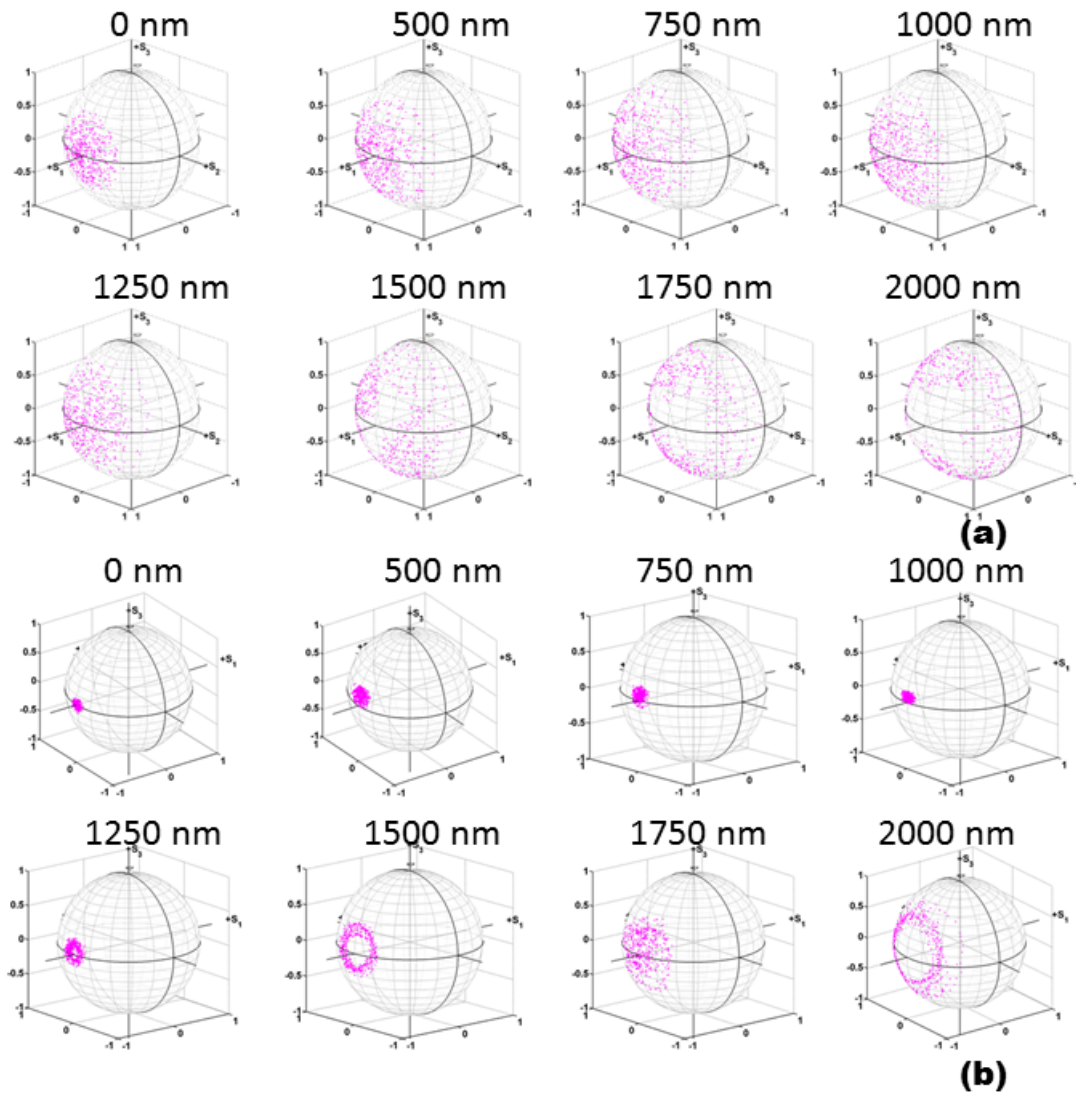


FIGURE 3.18: Poincaré sphere for the (a) TE and (b) TM mode, for 0 to $2 \mu\text{m}$ misalignment between the inverse taper and the polymer waveguide with a step of 250 nm.

working). What appears evident from the measurements is that the TE is affected far more than the TM mode. In fact, a misalignment as small as 500 nm already causes an average polarisation rotation of approximately 30 deg. The difference between the two modes can be explained by inspecting the electric field profile of the modes. As the TE is interacting more with the sidewall of the waveguide, the presence of any roughness will introduce higher polarisation state scattering than in the TM mode.

The experimental results have confirmed the theoretical simulations, where the optimum width for the minimum insertion losses is around $4 \mu\text{m}$ with a tapered

length of $300\ \mu\text{m}$. In the case of misalignment between the inverse tapers and the polymer waveguides, the absolute loss values do not increase substantially, but strong polarisation rotation on the TE mode is observed.

3.3 Waveguide Geometries

In the work presented so far, single mode waveguides in the form of silicon nanowires have been used. However, various other geometries have been exploited over the years as an alternative. Each design has unique characteristics, and it can be used for specific applications. In this section, the designed and fabrication of slots and subwavelength waveguides is discussed. The two designs were optimised for operation at wavelengths of $1.5\ \mu\text{m}$, and $3\ \mu\text{m}$ with the objective to assess the second-order non-linearity produced by the silicon-air interfaces. Some more background theory of the non-linearities in silicon and the design of the silicon nanowire for second harmonic generation experiments are given in Appendix C.

3.3.1 Slot Waveguides

Waveguides formed by two narrow silicon nanowires separated by a central air slot, i.e. also known as slot waveguides, are of interest for sensing [104, 105] due to the strong localisation of the field inside the slot. The fact that any element placed inside the slot experience a strong interaction with the propagating field can be exploited for the design of efficient sensors.

In our case, the slot is for interest as it increases the overlap of the mode with the silicon-air interfaces and therefore maximises any surface-induced second-order non-linearity. Also, two different parameters (widths of the gap and waveguide) can be varied separately and therefore provide an extra degree of freedom to optimise the waveguide dispersion. Also, to facilitate the coupling to optical fibres, the design of the coupling between straight and slot waveguides need to be explored in detail (Figure 3.19).

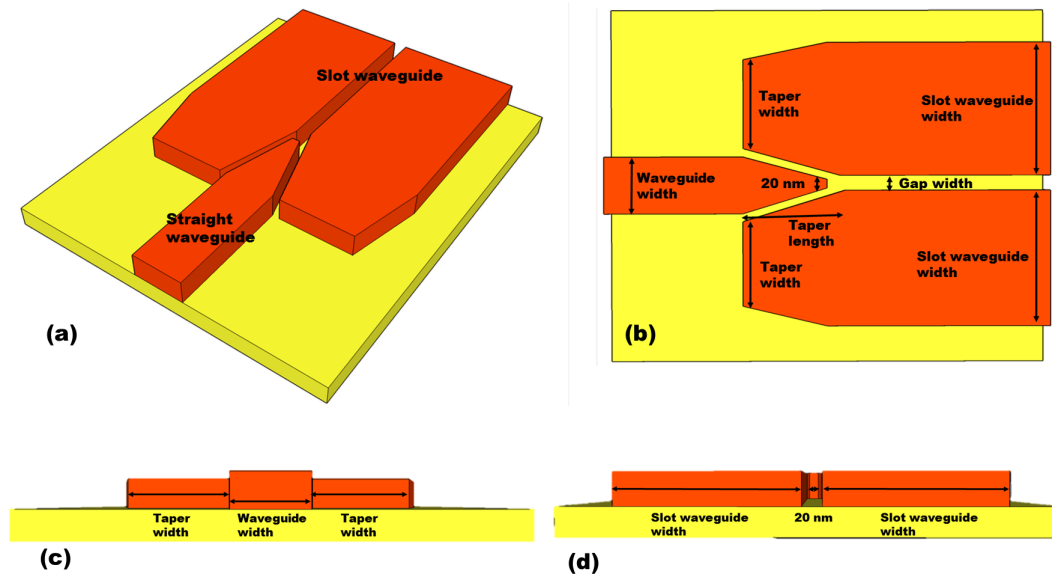


FIGURE 3.19: The nano-taper used for coupling between a straight and a slot waveguide (a) 3-D view, (b) Top-View, (c) side-view with the straight waveguide as an input and (d) side-view with the slot waveguide as an input.

3.3.1.1 Effective Index and Phase matching

The first parameter to be optimised was the width of the waveguides. The slot gap was fixed at a value of 100 nm, and the effective index against the width of the waveguide was calculated between 200 nm and 1 μm . The effective index at the wavelengths of $\lambda = 1.5 \mu\text{m}$ and $\lambda = 3 \mu\text{m}$ were plotted on the same graph in order to identify the phase matching condition in a second harmonic generation experiment with a pump at a wavelength of 3 μm as shown in Figure 3.20.

As it can be seen in Figure 3.20, only one phase matching condition exists between the fundamental TE mode for $\lambda = 3 \mu\text{m}$ and the fourth TE mode (TE_{04}) for $\lambda = 1.5 \mu\text{m}$ for a width of the waveguide of 980 nm.

With a good understanding on how the effective index of the slot waveguide depends on the total width of the waveguide, further simulations were performed in which the slot gap was varied from 50 nm to 300 nm. No significant change was observed on the general trend of the refractive index curves shown in Figure 3.20, except for the actual value of the effective index that decreased for increasing gap width. The major impact of varying the gap was found on the propagation losses as shown in Figure 3.21 for a wavelength of 3 μm . For increasing gaps, the losses

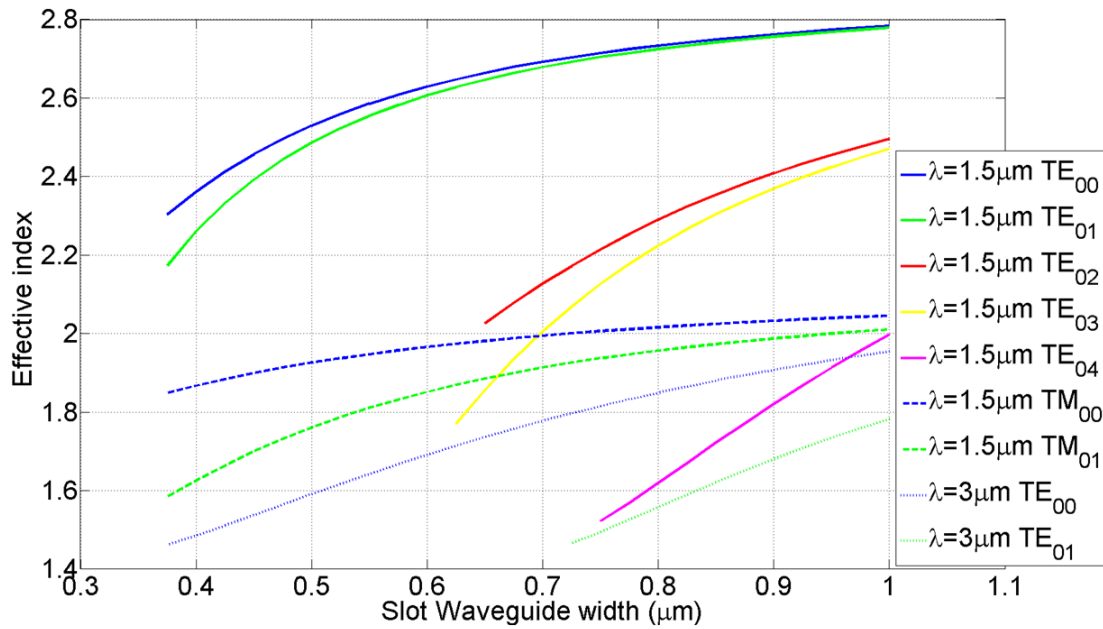


FIGURE 3.20: The effective index against the width of the slot waveguide, for wavelengths of $\lambda=1.5\mu\text{m}$ and $\lambda=3\mu\text{m}$, with a fixed gap width of 100 nm.

increase because of the smallest effective index and the lower confinement of the mode.

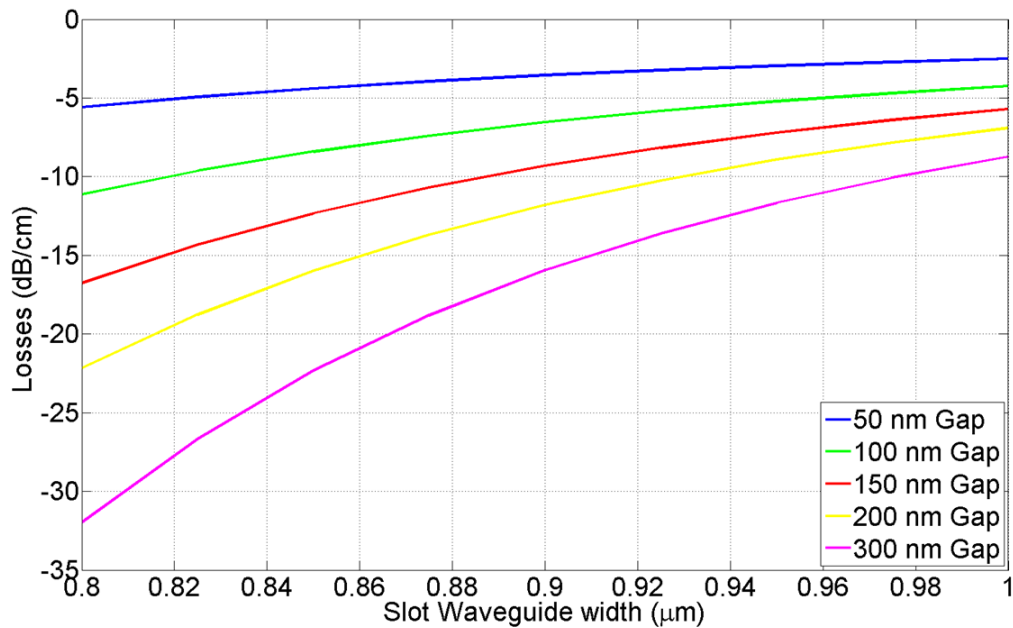


FIGURE 3.21: The losses at a wavelength of $3\mu\text{m}$ against the width of the slot waveguide for different gap widths.

The simulations for the slot waveguide geometry suggest that a small slot gap is needed for low propagation losses. Ideally, the 50 nm gap should be used to

keep the losses in the range 2-3 dB/cm but, due to fabrication limitations, this is extremely challenging. As discussed in Chapter 2, the etching depth is reduced for small gaps compared to open areas. If simple fabrication with a single etching depth is required, a gap of 100 nm is needed as a minimum gap in order to ensure uniform etching depths.

3.3.1.2 Taper design

The final component in the design of slot waveguides is the inverse taper for coupling the mode between the straight waveguide and slot waveguides. Two different designs have been optimised: one for coupling between the fundamental mode of the TE mode in and out of the slot waveguide at $\lambda = 3 \mu\text{m}$ and the second one for coupling between the TE_{04} and the TE_{00} at $\lambda = 1.5 \mu\text{m}$.

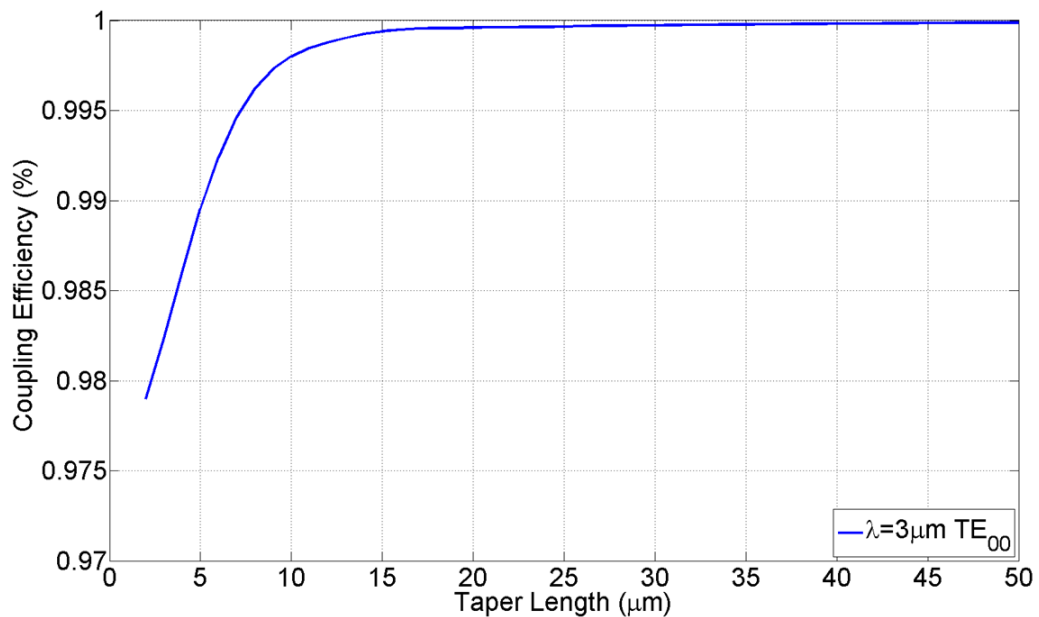


FIGURE 3.22: The coupling efficiency against the taper length between a straight waveguide with a $1.3 \mu\text{m}$ width and a slot waveguide with a 980 nm waveguide width and a 100 nm gap at $\lambda=3\mu\text{m}$.

For a wavelength of $3 \mu\text{m}$, the design was based on work reported in literature [106]. The taper was designed on the geometry depicted in Figure 3.19, with a waveguide width of $1.3 \mu\text{m}$. This value of the width was selected due to the low propagation losses (Figure C.3) and the absence of any phase matching conditions (Figure C.2). The above reasons make the width of $1.3 \mu\text{m}$ an ideal dimension for the input waveguide of the slot waveguide, i.e. losses are negligible and no second

harmonic generation will be generated in the input waveguide. Finally, the taper tip was chosen to be 20 nm to ensure adiabatic coupling.

With the above geometry, the coupling efficiency is very high, even for a very short taper length as it can be seen in Figure 3.22. A final length of 50 μm was chosen as it offers a more adiabatic coupling and also decreases the fabrication tolerance.

The second taper design was for the coupling between TE_{00} and TE_{04} . With a geometry similar to that discussed above, it was found that the taper was not adiabatic and additional losses were introduced. Therefore, a larger width of the taper had to be selected in order to couple between the fundamental TE mode and higher orders modes with negligible losses. After several simulations, the ideal taper width was found to be 850 nm.

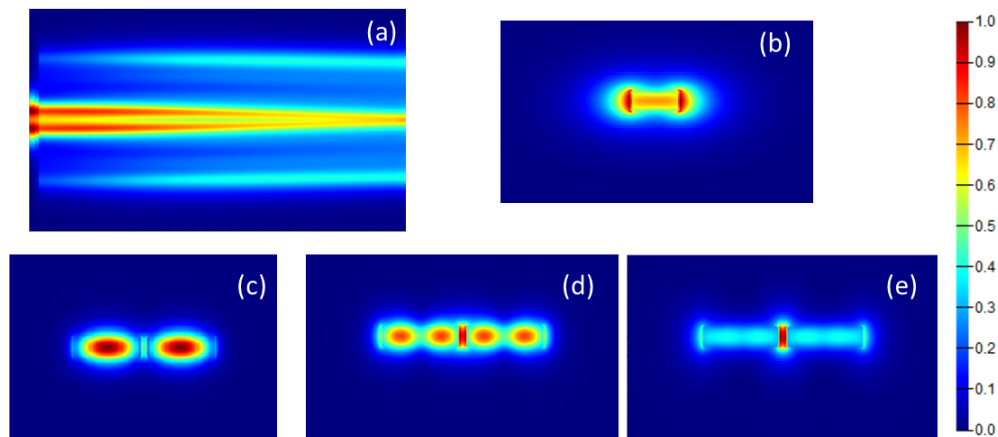


FIGURE 3.23: (a) The electric field for a 300 μm long taper as shown in Figure 3.19. (b) The input mode of TE_{00} for a straight waveguide with width of 300 nm. (c-e) The mode profiles for the TE_{00} , TE_{02} and TE_{04} in a slot waveguide with a waveguide width of 980 nm and 100 nm gap.

In order to enhance the coupling between the straight and slot waveguide, the mode has to strongly interact with the sidewall of the waveguide as shown in Figure 3.23b. For such interaction to be strong, an ideal width for the waveguide was found to be the 300 nm. While this width is suitable for the coupling between the two waveguides, the propagation losses of the mode is high. To circumvent this issue, the input 500 nm wide waveguide was tapered down to 300 nm just before the slot waveguide taper.

The maximum power in a slot waveguide is propagating in the middle of the waveguide as shown in Figure 3.23a. Following the simulations to calculate the mode solutions in the slot waveguide, it was found that two higher order modes

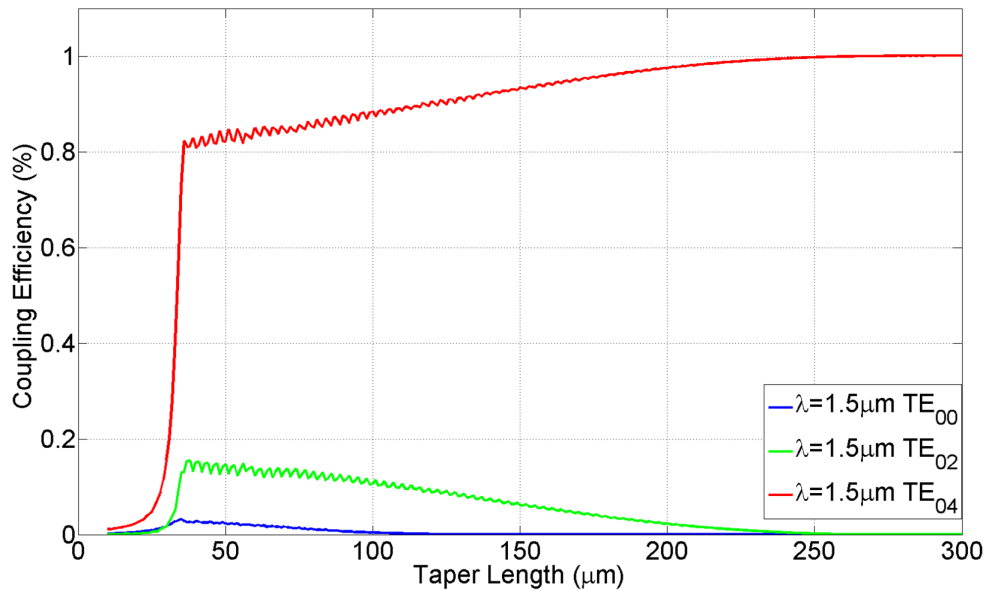


FIGURE 3.24: The coupling efficiency against the taper length between a straight waveguide of 300 nm width and a slot waveguide of 980 nm width and 100 nm gap at $\lambda=1.5\mu\text{m}$.

are able to propagate in the middle of the slot waveguide, TE_{02} and TE_{04} , as shown in Figure 3.23, as well as the fundamental TE mode. For our experiments, it was necessary to ensure coupling only for the TE_{04} into the slot waveguide.

For obtaining the coupling between the required modes, additional simulations were performed to assess the impact of the taper length on the coupling between different modes. The length was varied between 10 μm and 300 μm , and the coupling efficiency was recorded as shown in Figure 3.24. By using a non-adiabatic taper with a width of 850 nm, the coupling efficiency between the mode travelling in the straight waveguide and the TE_{04} rapidly increases and reaches almost 100 % for a taper length of 300 μm . At the same time, there is no coupling with the other modes.

Following the simulation results, the optimum dimensions of the taper are summarised in Table 3.2.

3.3.2 Sub-wavelength waveguides

Sub-Wavelength Waveguides (SWG) are periodic structures in which a grating with periodicity Λ is defined along the waveguides as shown in Figure 3.25.

Parameters	Values
Taper Length (μm)	300
Taper width (nm)	850
Slot gap (nm)	100
Slot waveguide width (nm)	980

TABLE 3.2: Slot waveguide and 1.5 μm wavelength input taper design parameters.

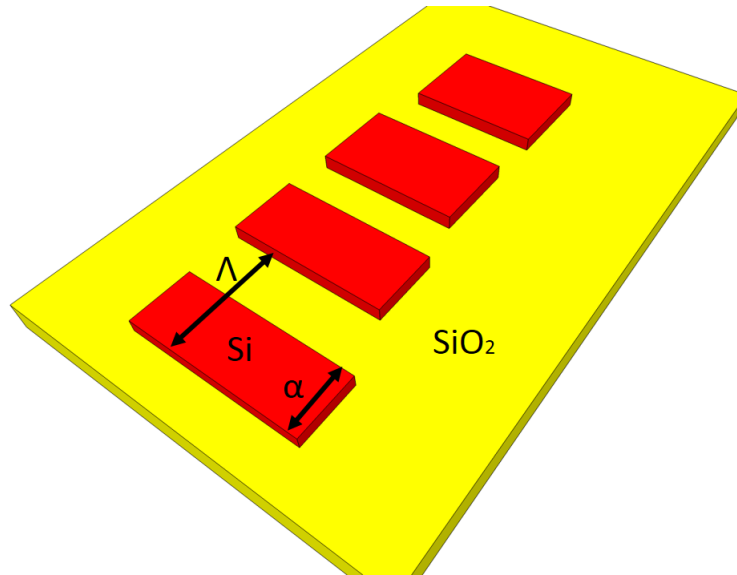


FIGURE 3.25: Schematic of a sub-wavelength grating waveguide.

The structure is fabricated by periodically etching the waveguide in order to obtain a periodic structure which is defined by a refractive index combination given by n_1 (silicon) and n_2 (silica or air). If the grating period is smaller than the wavelength (hence the term sub-wavelength grating), the wave sees a waveguide with an average refractive index given by [107]:

$$n_{\parallel} = (fn_1^2 + (1-f)n_2^2)^{1/2} \quad (3.7)$$

for a wave with TE polarisation and

$$n_{\perp} = (fn_1^{-2} + (1-f)n_2^{-2})^{-1/2} \quad (3.8)$$

for a wave with TM polarisation.

Where $f = \alpha/\Lambda$ is the duty cycle of the grating (see Figure 3.25). The above equations, derived from the effective medium theory [107], are accurate for calculating the effective index of the mode but do not provide information on the losses, which need to be experimentally assessed. [108].

SWG waveguides have recently attracted interest in experimental [108] and theoretical works [109]. A variety of devices was simulated and fabricated based on SWG, from simple straight and bent waveguides [108], polarisation selectively filters [110], couplers [111][107] and sensing devices [109].

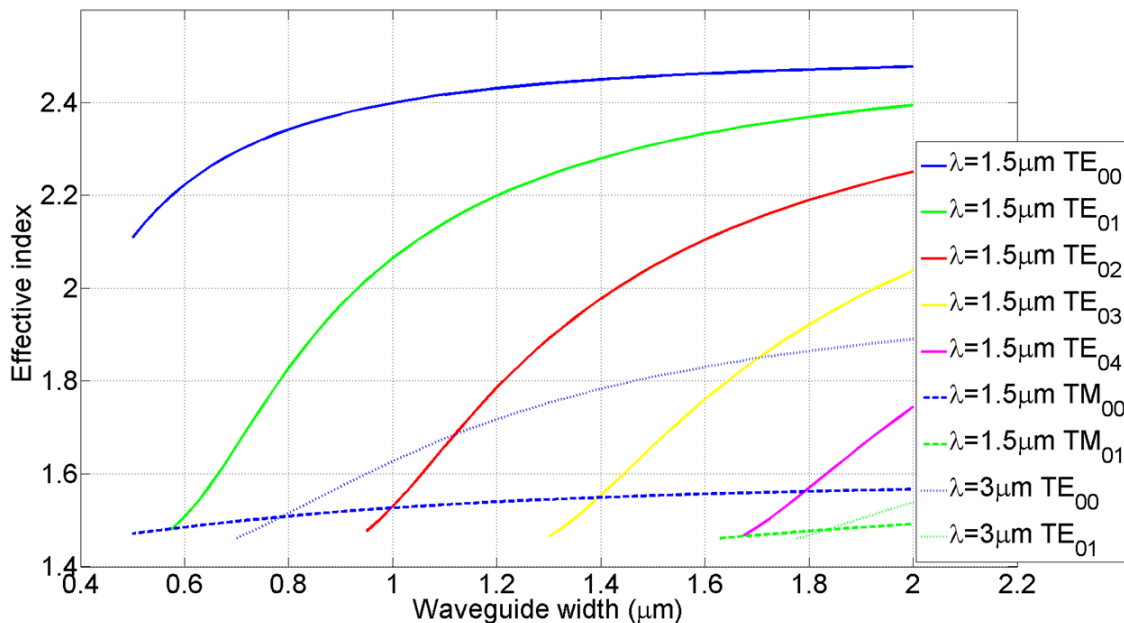


FIGURE 3.26: The effective index of a sub-wavelength grating against the width of the waveguides, for a wavelengths of $\lambda=1.5\mu\text{m}$ and $\lambda=3\mu\text{m}$. The SWG have a periodicity of 200 nm and $\alpha = 150$ nm.

The main reason for developing sub-wavelength waveguides is that the interaction of the mode with the silicon-air interface is strongly enhanced compared to a standard waveguide. Similarly to the slot waveguides discussed in the previous section, this geometry has the potential to increase the surface-induced second-order non-linearity in silicon waveguides. In order to optimise SWG designs for our experiments, mode simulations were performed to optimise the dimensions of the waveguides. Both Lumerical mode solutions [112] and a finite element method in Matlab [113] were used. The simulated structure consisted of a SOI wafer with $2\mu\text{m}$ box and a 220 nm core. The refractive index of the core was calculated from equations 3.7 and 3.8 as a function of the duty cycle of the SWGs. For this work, two duty cycles were initially chosen: $\alpha = 150$ nm and $\alpha = 100$ nm with $\Lambda = 200$

nm. The second duty cycle was found to be too lossy at a wavelength of $3\ \mu\text{m}$ and hence was no further explored. The effective index against the width of the waveguide for $\alpha = 150\ \text{nm}$ and $\Lambda = 200\ \text{nm}$ can be seen in Figure 3.26. It is worth noting that the effective index for a wavelength of $3\ \mu\text{m}$ is very close to cut off, even for the duty cycle with $\alpha = 150\ \text{nm}$ and hence the losses are expected to be high.

Similarly to the slot waveguides, a taper was needed for coupling light between the SGWs and the straight input waveguides. The taper design, in this case, is more straightforward and a simple adiabatic approach can be used in all geometries. A $300\ \mu\text{m}$ long taper with a tip width of $20\ \text{nm}$ was selected as the optimal geometry.

The fabricated devices for both the slot waveguides and the SWGs are shown in Figure 3.27.

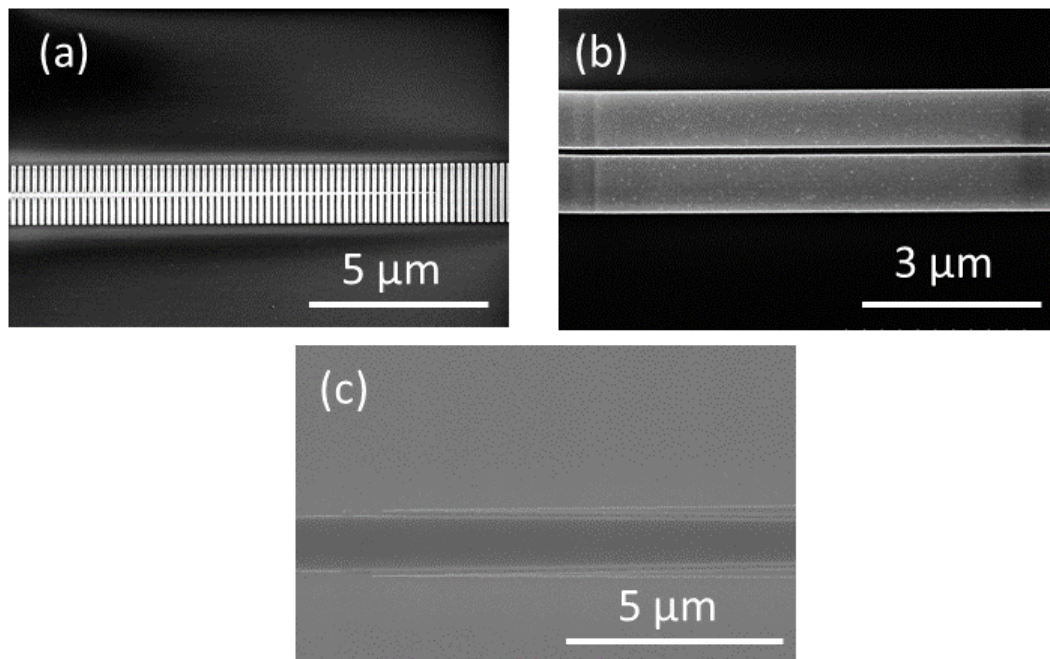


FIGURE 3.27: SEM images of the fabricated devices. (a) SWGs with coupling taper, (b) Slot waveguide and (c) An inverse taper to slot waveguide transition.

3.4 Conclusion

In this chapter, a number of key components in the design of silicon photonic circuits were optimised. The first component was metallic heaters deposited on

the top of the waveguides to tune their refractive index. The performance of the heaters was optimised both theoretically and experimentally for power efficiency and high tuning range. The heater geometry with the highest power efficiency has a width of 900 nm, whereas the best tuning range is achieved with a 2 μm wide heater. To ensure uniformity of the metallic layer, a minimum thickness of 50 nm for the NiCr layer was chosen. However, simulations clearly indicate that thinner layers can be very advantageous in terms of power efficiency. A number of deposition tests are currently being performed to optimise the uniformity of the layer so as to decrease its thickness to values in the order of 20nm. Also, a number of alternative designs are currently being explored where the heater is in direct contact to the silicon to improve its time response. In order to avoid extra optical losses due to the presence of the metal, a shallowly etched waveguide configuration will be implemented with the metal to be placed a few microns away from the waveguide as described in the literature[81].

The second activity presented in this Chapter was the optimisation of the inverse taper polymer couplers for minimum insertion losses. Even though we demonstrated insertion losses as low as 1 dB; it was found that the performance strongly depends on the geometry of the polymer waveguide. The thickness and process development parameters of SU8, which is the preferred option, are very dependent on its age. A different option for the polymer waveguide needs to be developed to ensure a more robust fabrication process. Potentially the use of silicon nitride waveguides could be an interesting solution, but more investigation is required.

On the third Section of this Chapter, the design and fabrication limitations of two different waveguide geometries were presented: the slot and the sub-wavelength waveguides (SWGs). Both geometries offer an alternative solution to the simple nanowires in applications that either require a larger delocalisation of the mode (i.e. for sensing) or stronger interaction with the silicon/air interfaces (i.e. for surface-induced non-linearities). While the designs have not yet been experimentally characterised, several devices were designed and fabricated and are described in more detail in Appendix C.

Chapter 4

Polarisation Selective Filters

4.1 Introduction

The accurate control of the state of polarisation is of great importance to a large variety of integrated photonics circuits for telecommunication systems [120], hybrid III-V on silicon lasers [121, 122] signal processing [123, 124], and quantum photonics [125, 126]. In particular, filters with accurate control over the behaviour of the TE and TM polarisation as well as with high extinction ratios are desirable in many applications. In quantum photonic devices, the latter is of great importance as the pump signal needs to be very strongly rejected [86, 127, 128].

The sidewall Bragg gratings offer a simple solution to filtering light on-chip, and they have been widely studied [110, 129, 130] and used [120, 131–133] as filters for the TE polarisation due to their simple fabrication [134], as both waveguides and gratings are defined in the same lithographic and etching steps. Furthermore, the stop band can be easily engineered by apodising or chirping the grating profile [135, 136]. On the drawback, as a result of the high Δn of Si and the strong interaction of the TE mode with the edges of the waveguide, a strong scattering between the two polarisations is present [42]. The coupling of part of the TE polarisation into the TM mode results in a saturation of the maximum extinction ratio of approximately 30dB regardless of the strength or length of the grating. The solution to the problem is to simultaneously filter both modes through the development of alternative geometries [137, 138].

In this chapter, we first theoretically analyse the side-wall Bragg grating geometries, showing how the extinction ratio and the stop-band width depend on the coupling coefficient (κ) and grating length (see figure 4.1). A number of experimental results for side-wall grating filters will be presented, and the limitation of the design will be discussed with regards to the polarisation state of the propagating light. Two independent designs for TM polarisation will then be introduced and experimentally evaluated. Finally, a combination of TE/TM selective filter will be presented and evaluated.

4.2 Side-wall grating Bragg filters

4.2.1 Design

This section will introduce the basic principles and design rules of waveguide Bragg gratings. Figure 4.1 shows the schematic of the side-wall Bragg grating geometry that will be explored in this work. The grating is defined by its amplitude (α), grating length (L_G), period (Λ) between the higher (n_1) and the lower (n_2) refractive index section and duty cycle (D_G) which is given by the equation:

$$D_G = \frac{w_{n_1}}{\Lambda} \quad (4.1)$$

where w_{n_1} is the width of the higher refractive index section.

The effective index (n_{eff}) of the grating will depend on the material refractive index as well as on the amplitude and the duty cycle of the grating. For small amplitudes α around 5 nm, the effective index of the grating can be assumed the same as the effective index of the input waveguide (for this work the input waveguide is 500 nm in width with $n_{eff} \approx 2.44$ and $n_{eff} \approx 1.77$ for the TE and TM polarisation, respectively). Since the effective index is not linear with the width of the waveguide, this assumption does not hold for amplitudes larger than 5 nm.

The grating strength depends on the amplitude of the sidewall corrugation and is defined by the coupling coefficient (κ) of the grating which can be either extract from the simulations based on the equation:

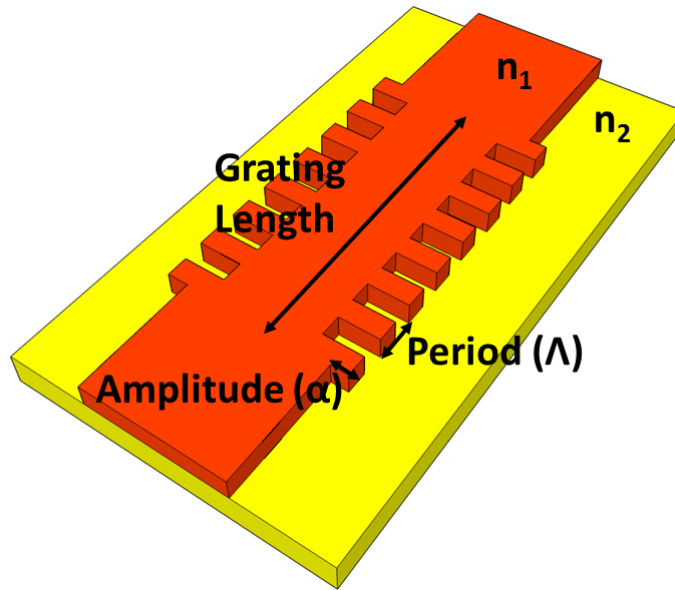


FIGURE 4.1: Schematic of a side-wall Bragg grating geometry.

$$\kappa = \frac{(n_1^2 - n_2^2)\Gamma_{x,y}}{2n_{eff}^2\Lambda} \quad (4.2)$$

or from experimental data using:

$$\kappa = \pi n_g \frac{\Delta\lambda}{\lambda_0^2} \quad (4.3)$$

where $\Gamma_{x,y}$ is the confinement factor of the mode in the waveguide cross section, n_g is the group index, λ_0 is the Bragg wavelength and $\Delta\lambda$ is the bandwidth which can either be measured experimentally.

The stop band is created by the coupling of the forward and backward mode induced by the periodic refractive index perturbation. The period of the perturbation Λ is given by the Bragg condition:

$$m\lambda_0 = 2n_{eff}\Lambda \quad (4.4)$$

Where m is the order of the grating and can take integer values $m = 1, 2, 3, \dots$. The extinction ratio (ER) of the stop band depends on both the amplitude and length of the gratings (i.e. also known as the κL product of the grating). For high ER the backward reflection R_G induced by the gratings has to be as close to 1 as possible:

$$R_G = \tanh^2(\kappa L_G) \quad (4.5)$$

The first step was to evaluate the effect of the κL product on the ER of the grating.

The theoretical investigation was done with a commercial software, Lumerical, which is based on an Eigenmode Expansion (EME) and a Finite Difference Time Domain (FDTD) solver as described in Appendix B.

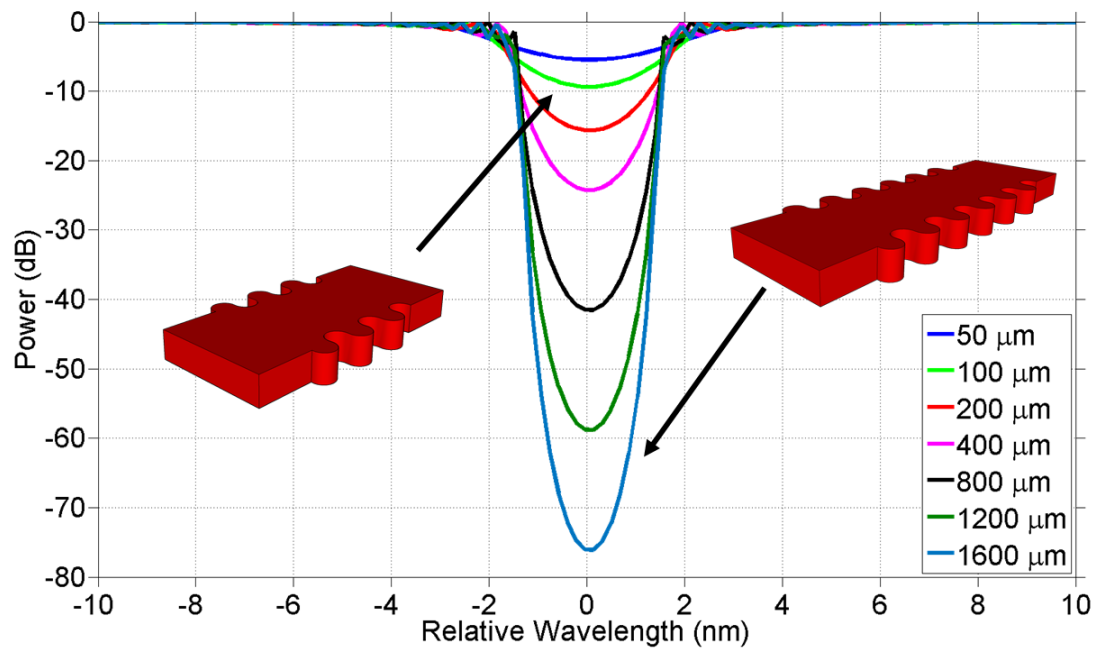


FIGURE 4.2: The simulated optical spectrum of side-walls gratings for the TE polarisation as a function the length.

While the period and the duty cycle of the gratings were fixed, the grating length and the amplitude were varied. Initially, a fixed amplitude of 5 nm was chosen, and the L_G was increased from 50 μm to 1600 μm , with the output spectra shown in Figure 4.2. These initial simulations were followed by a second set where the length was fixed to 50 μm , and the amplitude was varied from 5 to 40 nm as shown in Figure 4.3.

In both cases, the ER can be increased indefinitely by increasing the κL product. The main difference is that increasing the grating length does not enlarge the stopband bandwidth while increasing the kappa affects both the ER and the stopband bandwidth.

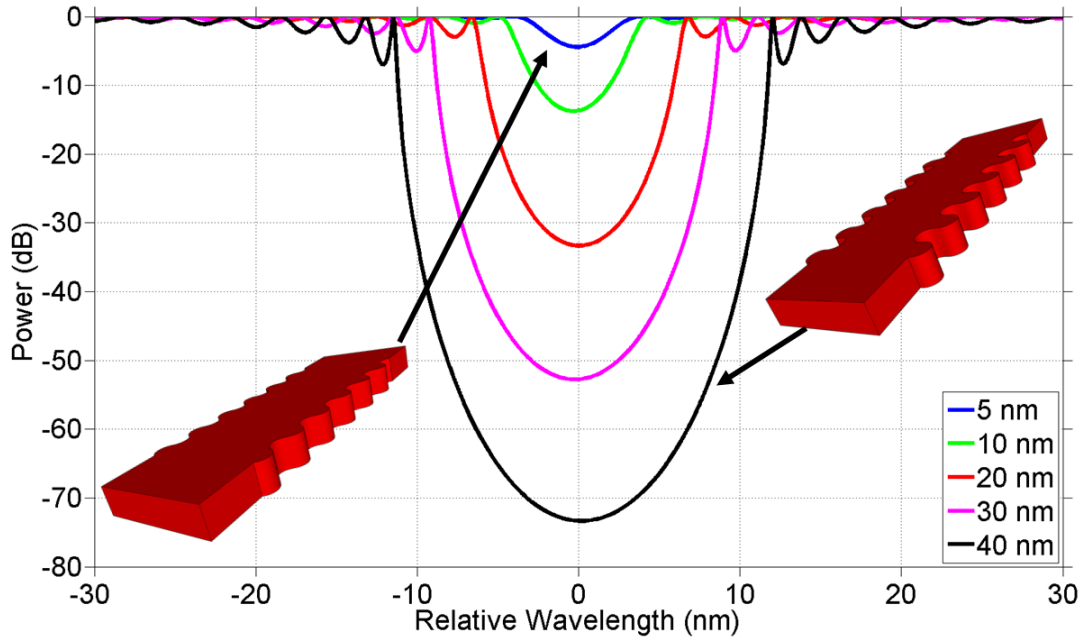


FIGURE 4.3: The simulated optical spectrum of side-walls gratings for the TE polarisation as a function the grating amplitude.

4.2.2 Experimental results

Following the simulation results, a set of devices with varying amplitude and length were fabricated based on the standard silicon fabrication procedure described in Section 2.2. Four different amplitudes (5,10,20 and 30 nm) and seven different lengths (50,100,200,400,800,1200 and 1600 μm) for each amplitude were chosen. Several copies of each device were fabricated to minimise any fabrication errors and statistical variations. The grating had a periodicity of 318 nm for the TE mode, which provides a theoretical minimum of the stopband at 1550 nm. To simplify the fabrication, a sinusoidal perturbation and a duty cycle of 50 % were chosen.

The samples were measured by coupling light into the devices with a polarisation maintain (PM) fibre from a tunable laser with an output power of 0 dBm. The light was passed through an in-line polariser with 20 dB ER between the TE/TM mode prior to the coupling into the sample. The output light was collected with a second PM fibre, without any polarisation manipulation, and the signal was measured an Optical Spectrum Analyser (OSA). The total on-chip propagation losses were measured to be 4.5 dB, while the total insertion losses (coupling and propagation losses) of the chip were approximately 10 dB.

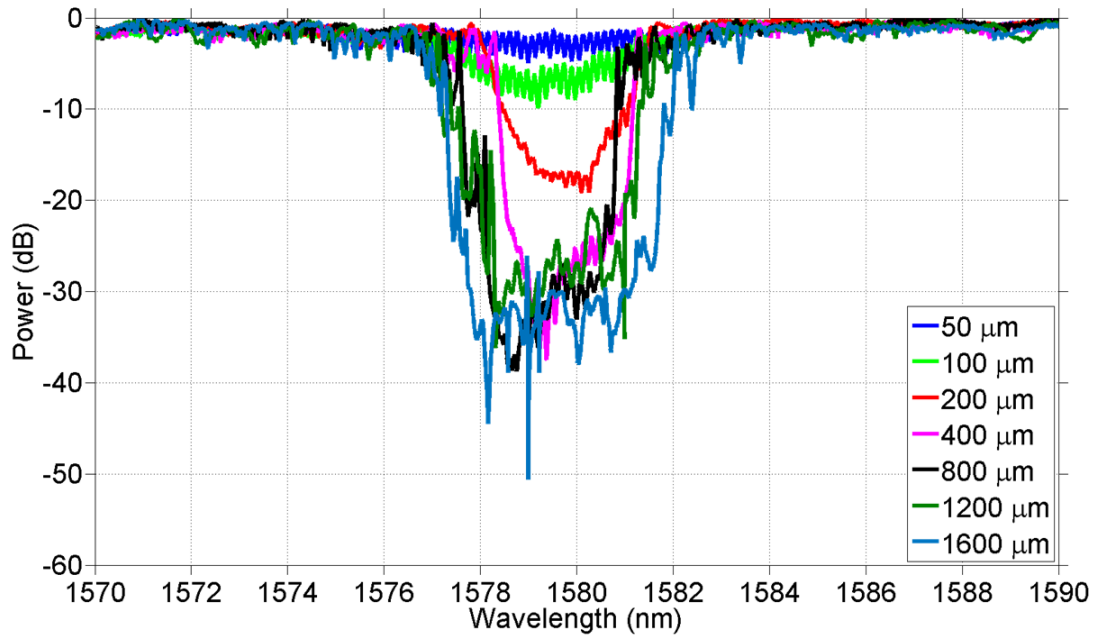


FIGURE 4.4: The experimental optical spectra of side-wall gratings for the TE polarisation with 5 nm fixed amplitude as a function of their length.

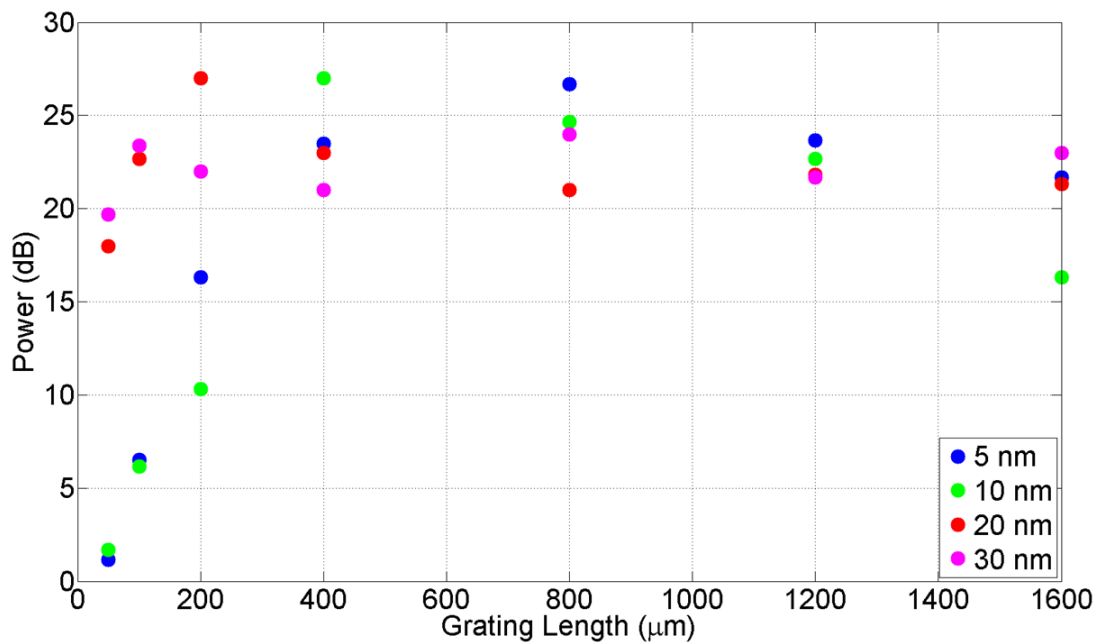


FIGURE 4.5: The extinction ratio of side-wall gratings for the TE polarisation as a function of the grating amplitude and length.

Figure 4.4 shows the optical spectra of the 5 nm amplitude gratings as a function of their length. As expected the ER increases with increasing length until it saturates at around 30 dB. As Figure 4.5 shows, the same behaviour was recorded for any grating amplitude. Independently on the grating amplitude or length, a saturation of around 25-30 dB in the ER was recorded for a κL product of approximately 10.

The origin of the saturation of the ER can be easily explained by analysing the output signal of a typical silicon waveguide with a polarimeter. Figure 4.6 shows the Poincaré spheres for (a) TE and (b) TM polarised mode for a straight waveguide with standard dimensions of 500 nm width and 220 nm height. As described in Section 3.2 and by Morichetti et al [42], silicon is a high refractive index material, and any roughness causes polarisation rotation. The scattering is more pronounced in the TE polarised mode because its interaction with the rougher waveguide sidewall is stronger than that of the TM polarised mode. This scattering is exacerbated in the presence of sidewall grating corrugation. Because the sidewall grating is very ineffective on the TM polarised mode, the residual output signal in the stopband of the filter is most probably a TM polarised mode.

In order to confirm this claim, a polariser was placed at the output fibre before the OSA. The recorded extinction ratio of the devices increased by 20 dB, which well agrees with the ER of the polariser. This clearly confirms that the limitation in the ER is the polarisation rotation inside the device. An easy solution to address this issue is to add polarisers at the output of the chip and cascade several chips to obtain high ER [86, 139] However, such approach largely increases the footprint of the whole filter and does not take benefit of the integration capabilities of SOI.

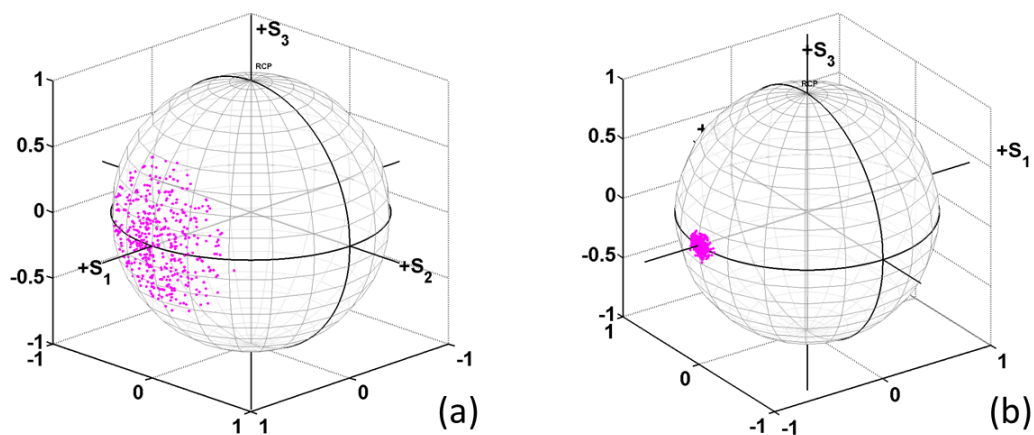


FIGURE 4.6: Poincaré spheres for polarisation rotation measurements for (a) TE and (b) TM mode in a 500 nm width and 220 nm high silicon waveguide.

4.3 TM filter

A better approach is to directly integrate a TM filter on the waveguide to remove the scattered signal. Important to this aim is first to gain a clear understanding of the modal profile of the TE and TM polarised modes in a single mode silicon waveguide. Figure 4.7 shows the electric field profile for (a) TE and (b) TM mode for a silicon waveguide with a geometry of 500 nm width and 220 nm high.

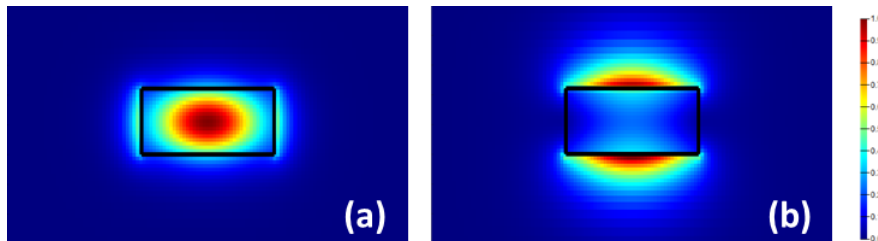


FIGURE 4.7: The profile of the electric field for the (a) TE and (b) TM polarisation in a 500 nm wide and 220 nm high silicon waveguide.

The TE mode is mainly confined in the centre of the waveguide with a strong interaction with the side-walls, which results in a strong scattering from the roughness induced by the lithographic and etching processes. On the other hand, the TM mode mainly propagates on the top and the bottom of the waveguide, with minimum interaction with the waveguide side-walls.

Even though it appears clear from the modal profile simulations that the TM has small interactions with the side-walls, additional simulations were carried out to quantify the effects of side-wall gratings on the TM mode. With the use of equation 4.4, the optimum grating period was found to be 438 nm, while the grating length and amplitude were varied over the same parameter space used for Figure 4.2 and 4.3.

Figure 4.8 shows the simulated optical spectra of the side-wall gratings for the TM mode for various lengths. As found with the previous results on the TE mode, the extinction ratio increases with increasing length, but it is at least an order of magnitude smaller than for TE mode. The simulated optical spectra for the amplitude variation are shown in Figure 4.9, where, similarly to the previous simulations, the extinction ratio increases with increasing amplitude, but with an ER being over two orders of magnitude smaller than the ER for the TE mode with the same grating amplitude and length.

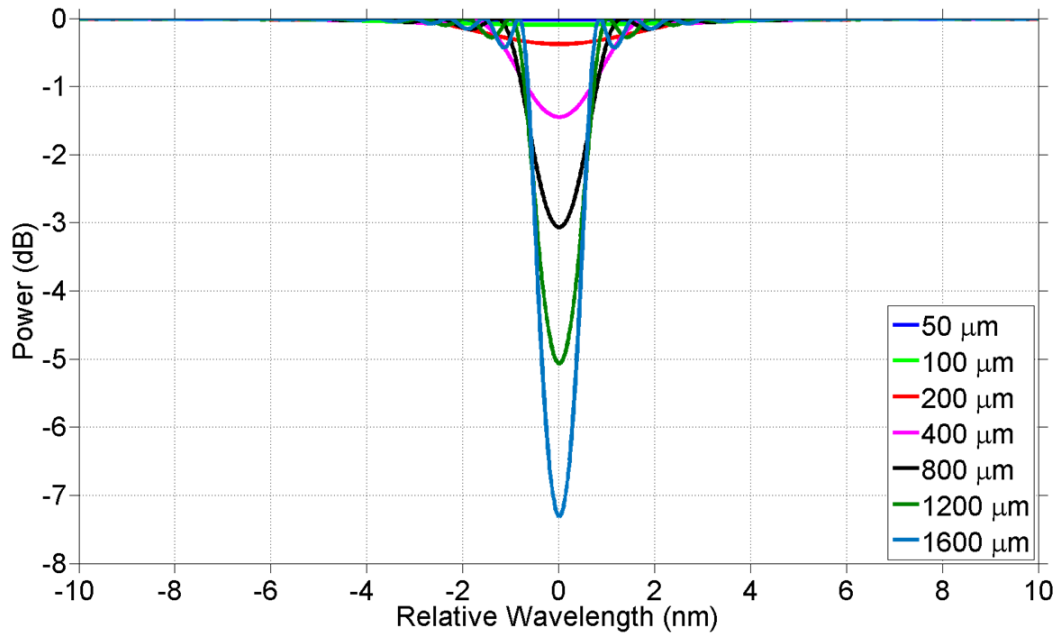


FIGURE 4.8: The simulated optical spectra of side-wall gratings for the TM polarisation as a function the grating length.

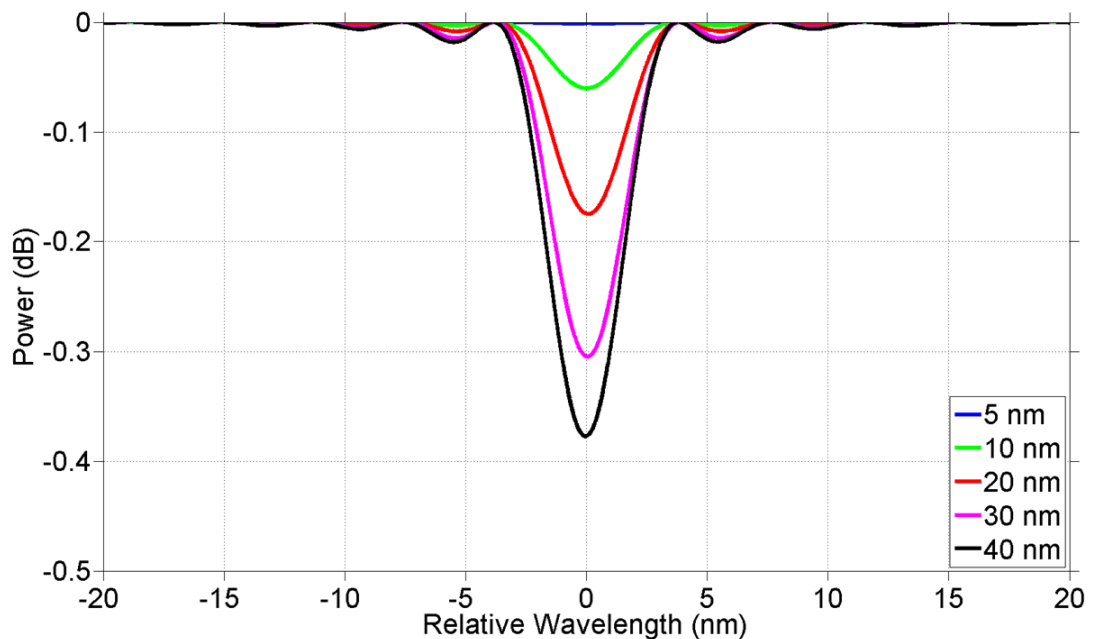


FIGURE 4.9: The simulated optical spectra of side-wall gratings for the TM polarisation as a function the grating amplitude.

Such a strong difference between the two polarisations is an obvious consequence of the very different interaction of the modal profiles with the side-wall of the waveguide. Following the same idea behind the design of the sidewall gratings, for maximum extinction ratios of the TM mode, a filter on the top of the waveguide is needed, as the bottom of the waveguide is not accessible. Two different filters

were designed and evaluated, which are presented in the rest of this chapter.

4.3.1 Metallic TM filter

The first design investigated is a simple metallic strip deposited on the top of the waveguide, which acts as a TM filter. This geometry builds on the large difference in the losses between the TE and TM mode which are induced from a metal strip on the top of the waveguide as discussed in Section 3.1 and shown in Figure 3.2b. While the propagation losses for the TE mode is below 10^{-2} dB/cm, for a cladding height of approximately $1 \mu\text{m}$, the TM mode losses are of the order of 20 dB/cm.

Two identical sets of devices were fabricated as described in Section 2.2. Both chips contained the same grating designs as those presented in the previous section. The first set was left unchanged, whereas a metal layer was placed on the top of the grating waveguides for the second chip. Due to the limitation of the lithography, it was chosen to replace the devices with 5 nm amplitude with an amplitude of 6 nm. This was done due to the proximity of the 5 nm amplitude gratings with the minimum possible Beam Step Size of our EBL (3nm). A 6 nm amplitude is an integer number of BSS and gives higher repeatability between consecutive fabrication runs. All the devices were characterised as described in Section 4.2.2, without any polarisation control at the output of the waveguide.

Figure 4.10 shows the optical spectra of a device with no metal (blue line) on the top and the same one with metal (red line) on the top. The distance between the metal and the waveguide is given by the upper cladding height, which has been optimised in Chapter 3 and is about $1 \mu\text{m}$.

Figure 4.11 shows the extinction ratio of the gratings against their length. Similarly to the results presented in the previous section, devices without any metal on the top (blue dots) saturates around 25-30 dB, whereas the ER for the devices with metal (red dots) do not saturate before a value of around 50-55 dB. The increase in the ER ratio agrees well with the additional losses of the TM mode induced from the metal strip on the top of the waveguide (i.e. approximately 25 dB/cm).

Although a metal strip can be a good filter for the TM mode, its performance is limited by the device length. If very high extinction ratios are needed, the metallic strip requires to be unpractically long. Therefore, an alternative solution

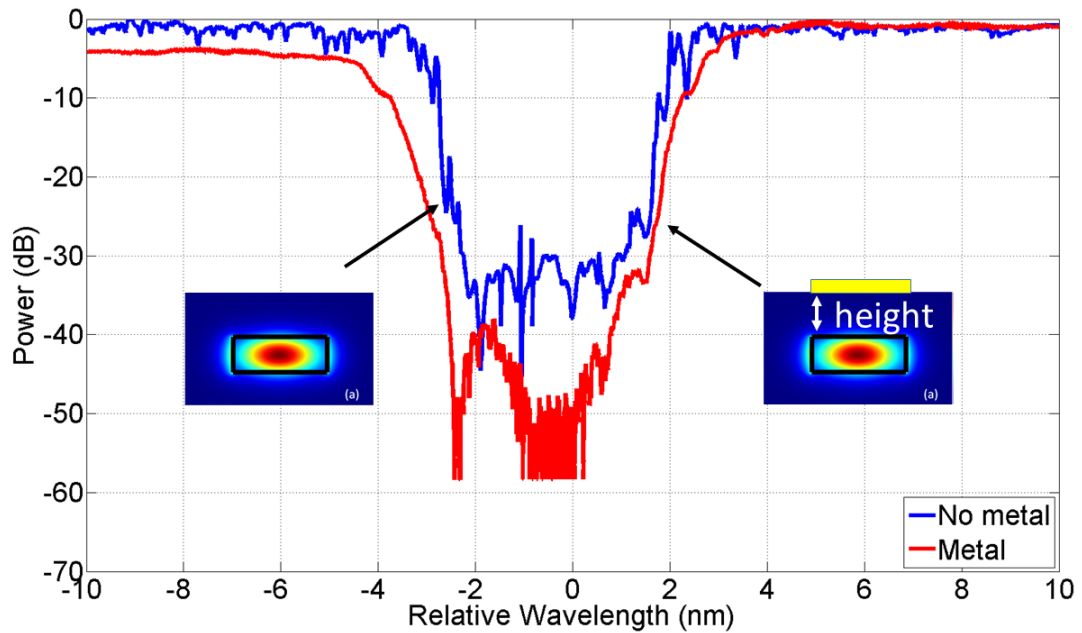


FIGURE 4.10: The optical spectra of side-wall gratings for the TE polarisation without (blue line) and with (red line) metal on the top of the waveguides.

is needed. Also, the presence of the TM absorbing metallic strip limits our ability to tune any device with a metallic heater as described in Chapter 3.

4.3.2 Top grating Bragg filters

4.3.2.1 Design

Since a large fraction of the TM mode overlaps with the top of the waveguide, a perturbation on the top of the waveguide, matching the Bragg condition (equation 4.4) can act as an effective filter.

For easier design and fabrication, as Figure 4.12 shows, circle gratings were chosen. For the side-wall gratings, only the amplitude and the length had to be optimised, as the etching was identical to the rest of the waveguide. The fabrication of the top gratings is more challenging as the etching depth (h) and diameter (d) of the holes as well as the grating length can be varied.

Even though the effect of the diameter of the holes and the length of the grating is of importance to the stop band and the extinction ratio, much of the simulations were focused on the grating behaviour as a function of the etching depth. The

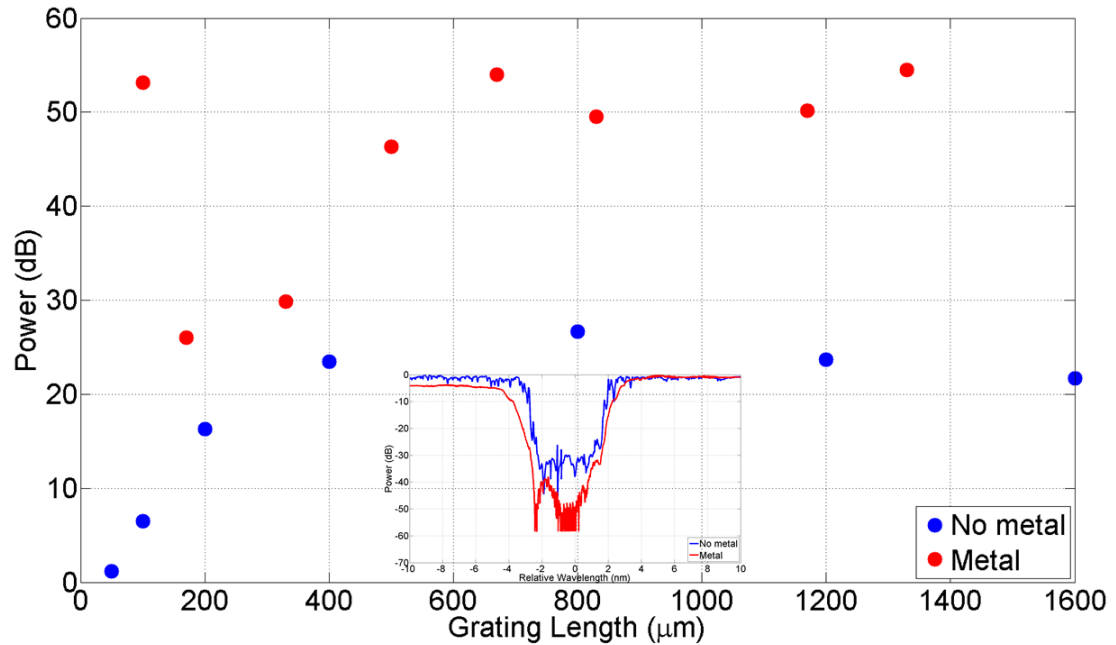


FIGURE 4.11: The extinction ratio of side-walls gratings for the TE polarisation as a function the grating amplitude and length, without (blue dots) and with (red dots) metal on the top of the waveguides.

motivation for this was that the hole depth has a profound impact on the modal profile and on the propagation losses as will be shown in the next section.

Figure 4.13 shows the simulated optical spectra for top gratings with (a) 40 nm and (b) deep etched holes for various lengths and a fixed hole diameter of 80 nm. The effect of the grating length, as expected, is the same as the side-wall gratings, i.e. as the length increases, the extinction ratio increased but the stopband is not affected. The deep etched holes show higher extinction ratio than the shallow ones although the difference is not significant. On the other hand, the stop band does not look affected by the etching depth as simulations show that the effective index of the TM mode does not change significantly for different etching depths of the hole and hence the coupling coefficient. This is also the reason for the modest increase in the extinction ratio.

Even though the etching depth does not have a big effect on the performance of the gratings, a substantial influence is expected in the optical losses of both the TE and TM mode. Figure 4.14 shows the optical losses for the (a) TE and (b) TM mode, as a function of the etching depth and the radius of the top gratings.

As expected, for both the TE and TM mode the losses rapidly increase for an increase in either the hole diameter or its etching depth. Bizarrely, as the etching

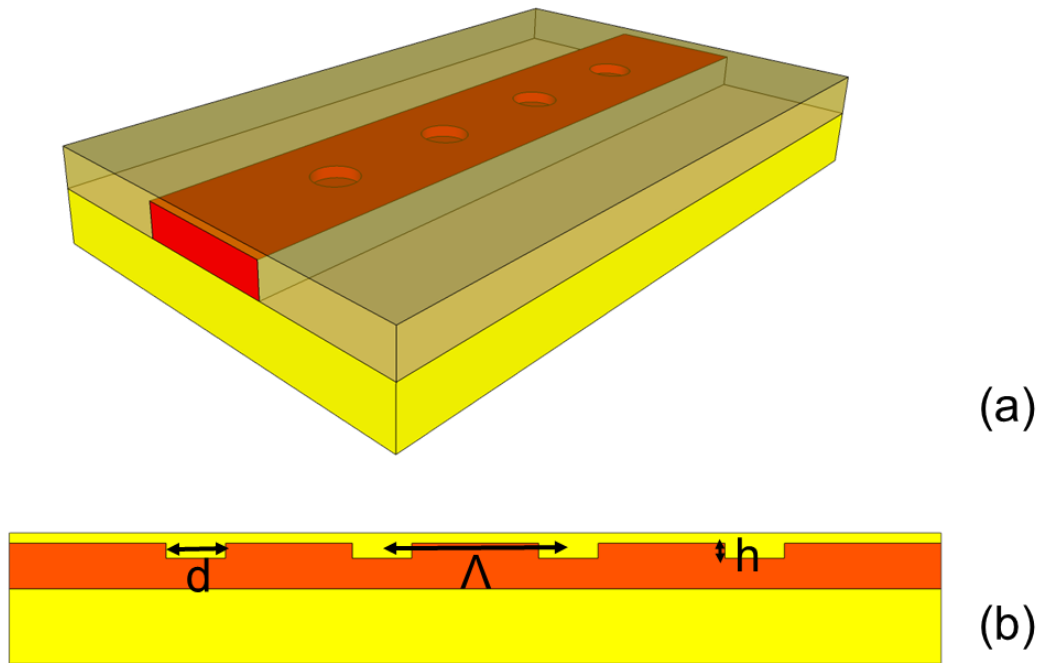


FIGURE 4.12: Schematic of the top Bragg gratings

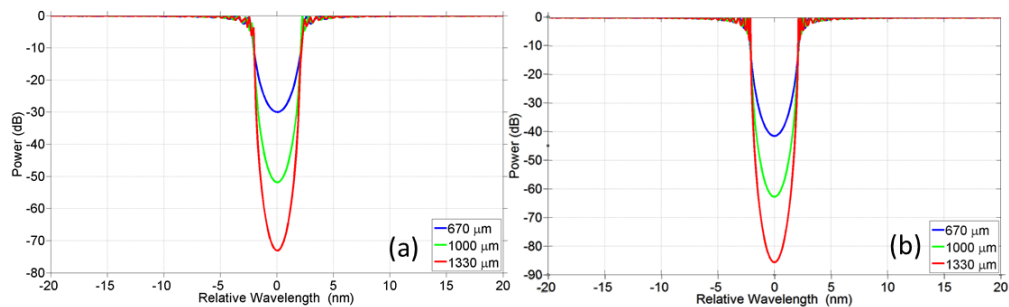


FIGURE 4.13: The simulated optical spectra of top gratings for the TM polarisation as a function of the length for (a) shallow and (b) deep etched gratings for a fixed hole diameter of 80 nm.

depth increases, the losses for the TM mode do not increase monotonically but reach a maximum at a depth of around 150 nm. This is happening because a very deep hole tends to form a slot waveguide geometry (see Chapter 3), which has lower losses than a partially etched straight waveguide (see Figure 4.15).

The same effect does not take place for the TE mode as the perturbation period does not match the Bragg condition and therefore the hole periodicity is below the propagating wavelength (i.e. the holes are seen as a sub-wavelength structure). As a result, the TE mode sees a waveguide with an average refractive index based on the duty cycle and the etching depth of the holes.

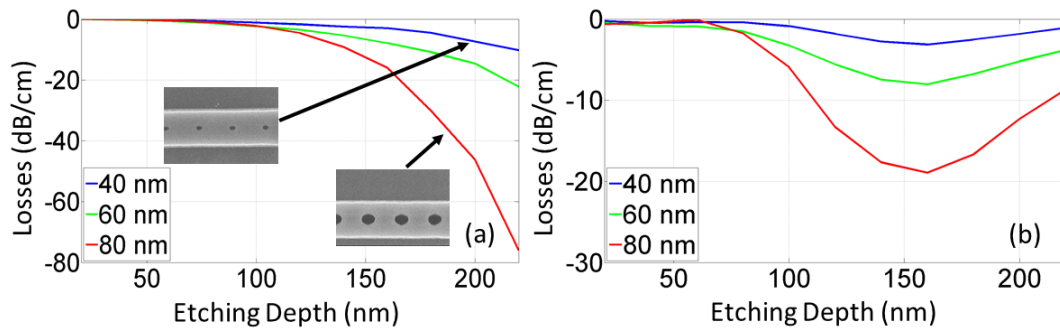


FIGURE 4.14: The theoretical losses of the (a) TE and (b) TM polarisation as a function of the grating radius and etching depth.

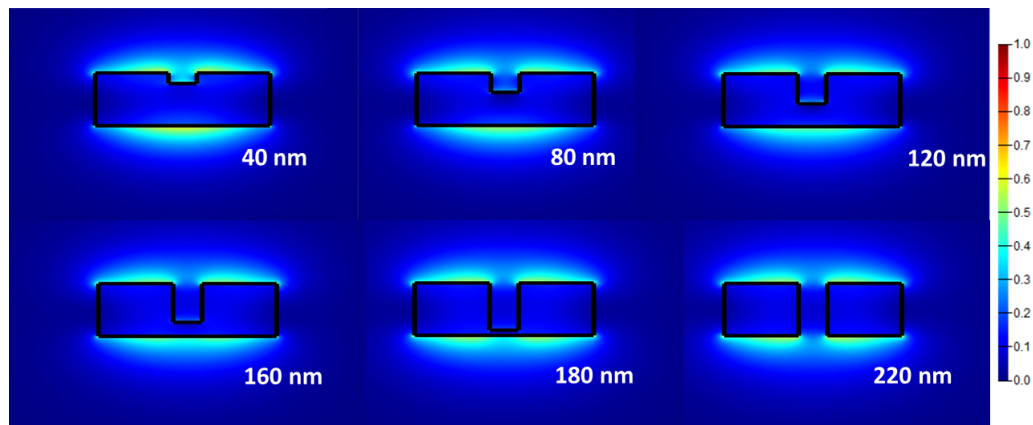


FIGURE 4.15: The profile of the electric field for various etching depths of 80 nm diameter hole in a 500 nm wide and 220 nm high silicon waveguide for the TM mode.

Based on the simulated results, small diameter ($d = 80$ and 160 nm) and shallow etched ($h = 40$ nm) holes were chosen as top gratings TM Bragg filters. The insert in Figure 4.14a shows fabricated devices for top gratings TM filters with various radius prior to the deposition of the upper silica cladding.

4.3.2.2 Experimental results

Experimental evaluation of the top grating TM filters was carried out on a set of devices with various top gratings radii and lengths. Three different lengths were chosen for the investigation ($L_G = 670, 1000$ and $1330 \mu m$), two different diameters ($d = 80$ and 160 nm) and a fixed etching depth of 40 nm with a period of 448 nm. In order to ensure a controllable shallow etched of 40 nm, the fabrication procedure described in Section 2.2 was modified. A ZEP mask was first used to define the holes, followed by a precisely timed shallow silicon etched that took

into account the feature size of the holes (i.e. the RIE lag effect links the hole diameter to the etching depth). Following the first silicon etching, the ZEP mask was removed and the rest of the standard silicon photonics fabrication (Section 2.2) was followed. While the pattern definition of the gratings by EBL is extremely accurate, an error of ± 2.5 nm is expected in the etching depth. However, as shown in Figure 4.13, this error will not affect the performance of the filters. The devices were characterised as described in Section 4.2.2, without any polarisation control at the output of the waveguides.

From the experimental results, it was confirmed that the gratings are invisible to the TE polarisation, and behave as excellent filters for the TM polarisation. However, they also introduce further propagation losses which were not predicted by the simulations. The extra insertion losses for the 40 nm radius holes were in the order of 20 dB/cm, whereas for the bigger holes were up to 80 dB/cm. This is due to the roughness induced by the etching of the holes, which cannot be simulated. Due to the high insertion losses of the 80 nm etched hole devices, no further study was made on these devices.

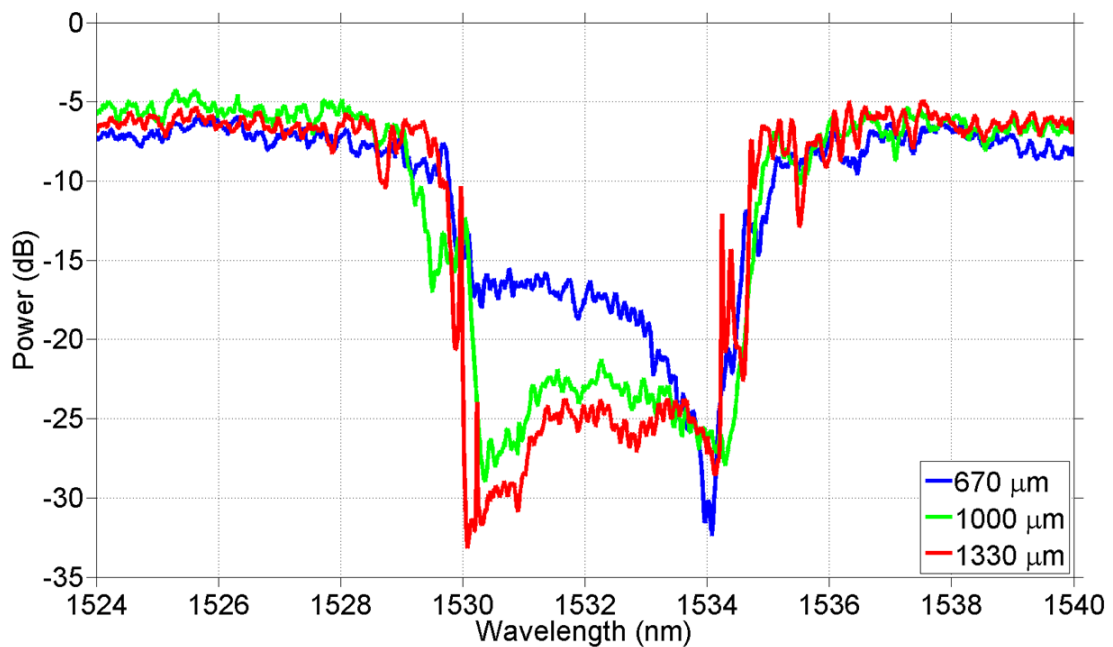


FIGURE 4.16: The experimental optical spectra of top gratings, with radius of 40 nm, for the TM polarisation as a function of their length.

Figure 4.16 shows the optical spectra of top gratings Bragg filters with holes with a 40 nm in radius and for all three grating lengths fabricated. The maximum ER is about 25dB and a similar saturation behaviour as that observed for the TE mode on the sidewall gratings is observed.

Parameters	Values / nm
Sidewall gratings amplitude	6
Sidewall gratings period	320
Top gratings diameter	80
Top gratings period	450
Top gratings etching depth	40

TABLE 4.1: The design parameters of the final grating device.

4.4 TE/TM Bragg filter

As a final experiment, a combination of the two filters was fabricated and evaluated on the same grating section. The periodicity of the two gratings were adjusted in order to overlap the stop band of the TE and TM filter when the two are fabricated on the same waveguide. Apart from the different period of the gratings, all the rest of the parameters were the same as in the previous experiments (see Table 4.1). The inserts of figure 4.17 and 4.18 show the fabricated devices prior to the deposition of the upper silica cladding.

Two sets of measurements took place on these devices. First, the transfer function of the grating was measured with TE polarised input light. Figure 4.17 shows the transmission spectra of an individual TE filter with sidewall grating only (blue line) and a TE/TM filter with the combination of the top and sidewall grating (green line) when a TE polarised light is coupled into the chip.

Due to a slight mismatch between the simulated and measured effective indices, the stop bands of the sidewall and top gratings are not perfectly matched. Even though this is not an ideal design, it is offering us the opportunity to compare the extinction ratio when the two filters are acting separately and together. A difference of the extinction ratio up to 30 dB is recorded between the two cases, with a maximum of 60 dB extinction ratio achieved in the spectral region where both filters overlap.

For the second set of experiments, the input light coupled to the chip was polarised to TM. Figure 4.18 shows the transmission spectrum of an individual TM filter with top gratings only (blue line) and the combination of the TE/TM filters (green line) when a TM polarised light is coupled into the device. Similarly to the previous case, when the dual TE/TM filter is used the whole stop band exhibit an increase

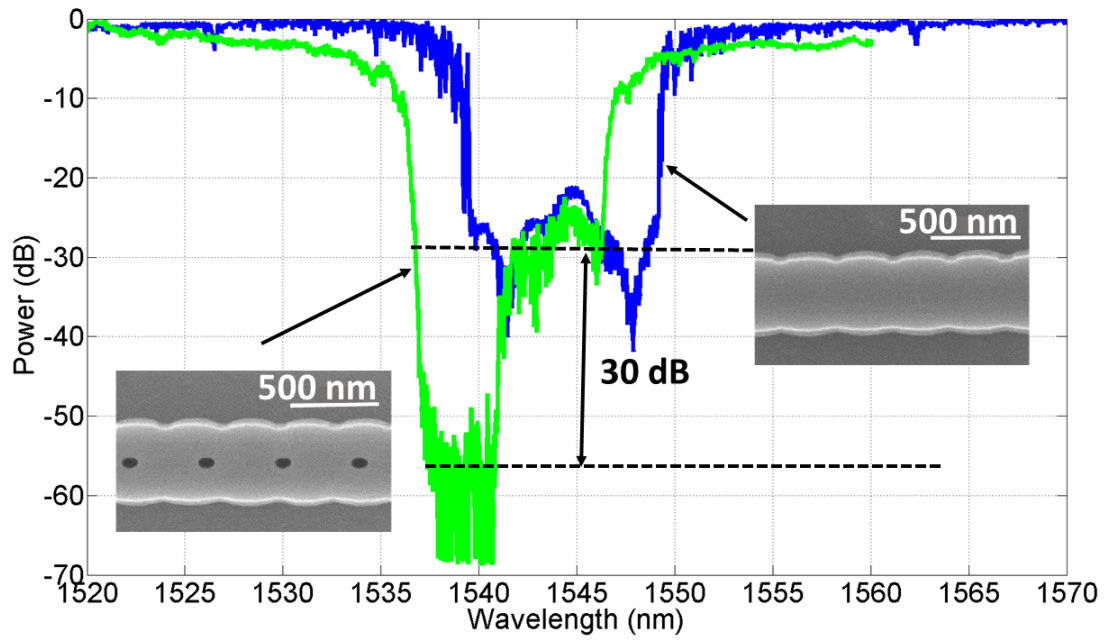


FIGURE 4.17: The transmission spectra of TE propagation for a single TE filter (blue line) and for a dual TE/TM filter (green line).

of the ER to up to 50 dB, which is an increase of almost 30 dB from the single TM filter case.

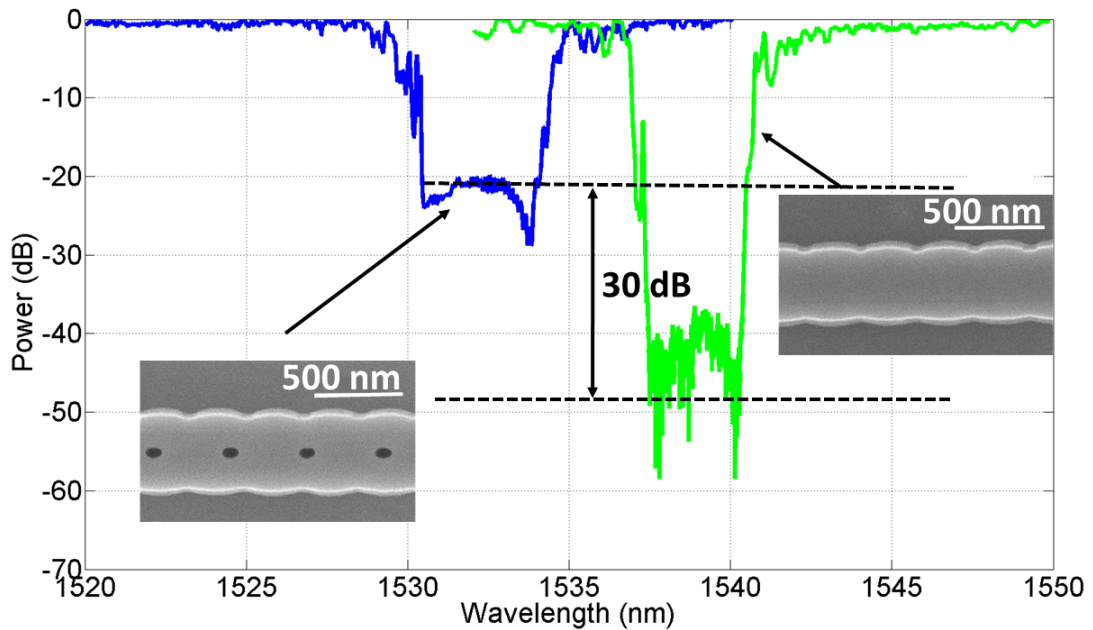


FIGURE 4.18: The transmission spectra of TM propagation for a single TM filter (blue line) and for dual TE/TM filters (green line).

The results show an increase of 30 dB for both polarisations, which, if the insertion losses are taken into account, corresponding to a total ER up to 75 dB. This value

is most probably a limit arising from light losses into the substrate. In fact, although a $2\ \mu\text{m}$ of BOX layer offers a good isolation of the core layer from the substrate and is a big improvement from the original $1\ \mu\text{m}$ BOX used a few years ago, some light is still escaping towards the substrate. This issue is known as substrate scattering.

In order to examine whether the final saturation is indeed due to substrate scattering, additional measurements were performed on a straight waveguide. The output fibre was first misaligned from the waveguide towards the silicon substrate. Then, measurements of the scattered light were taken as a function of the lateral distance from the output waveguide. The result recorded in Figure 4.19, show that an intensity value of $-74\ \text{dB}$ is measured exactly below the output waveguide. At a lateral displacement of $100\ \mu\text{m}$ from the waveguide, the signal levels decrease to $-82\ \text{dB}$, indicating scattering decrease of $8\ \text{dB}$ in the measured substrate scattering. Those results are in good agreement with the final saturation recorded on the extinction ratio of the filters.

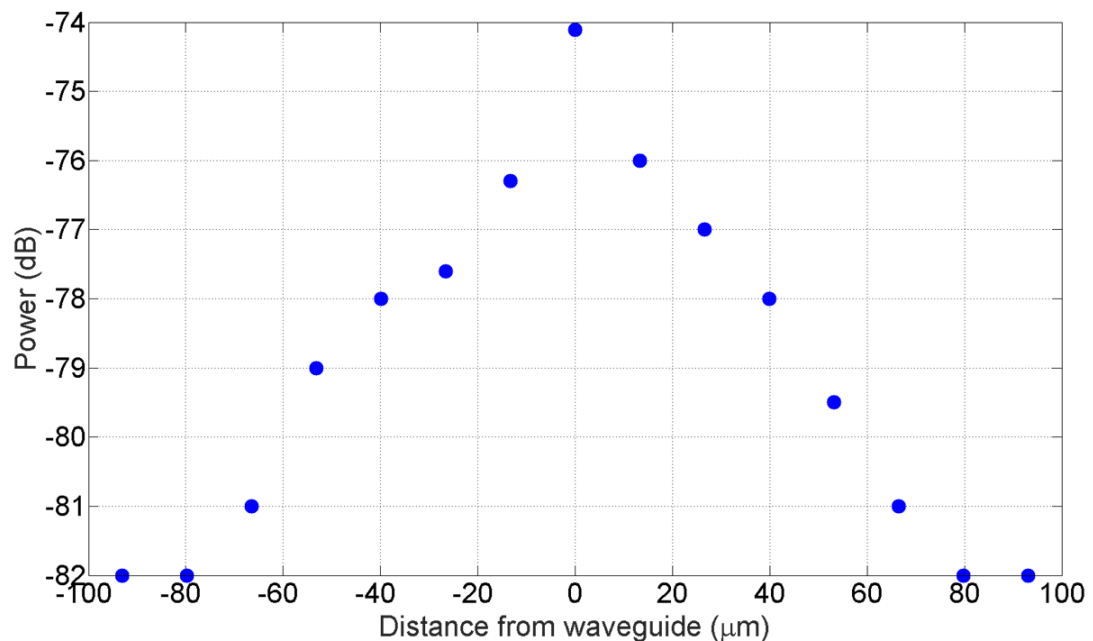


FIGURE 4.19: The level of substrate scattering as a function of the distance from the centre of the output waveguide.

This final result suggests that a further improvement of the filter performance might be obtained with an anti-reflection coating on the output edge of the chip and by folding the output waveguides so as to have both input and output waveguides on the input side of the chip. Such arrangement would completely remove any coupling from the substrate into the output optical fibres. This geometry will

be exploited in the future on all those devices that require on-chip filtering of the signal with extremely high values of ER.

4.5 Conclusion

In this chapter, polarisation selective filters were designed and studied. An initial theoretical and experimental investigation was performed on the well-assessed sidewall grating geometry, which provides flexible design and robust fabrication. Measurements clearly indicated that the maximum extinction ratio of 30-35dB is independent of the strength and length of the gratings, and is a consequence of the TE/TM polarisation rotation that occurs in waveguides with strong scattering.

Following the evaluation of the sidewall grating filters, two separate TM filters were design and experimentally evaluated to improve the overall extinction ratio of the devices. The first geometry consisted of a simple metallic strip deposited on the top of the waveguides, which acts as a TM absorber and therefore can offer an increase of the extinction ratio of the filters to up to 20 dB. However, this geometry limits the flexibility in designing more complex devices that either requires thermal tuning or multi-core configurations For the second filter design, a top grating Bragg filter was chosen as this provides a strong interaction with the TM polarised mode only. Experimental data indicate that the TM polarised mode can be filtered by up to 25 dB without adding appreciable losses to either the TE or TM polarised mode. Finally, a combination of the two Bragg gratings filters were integrated on the same waveguide, showing a maximum extinction ratio of up to 60, only limited by the substrate scattering.

As a future work, chips will be designed with the input and the output waveguides on the same side and an anti-reflection coating (AR) deposited on the output facet in order to reduce the noise from the substrate scattering and reach extinction ratios of 100 dB or more.

It is worth remarking that these geometries offer an appealing solution to independent manipulation of the TE and TM polarisations and as such are of interest to all those devices that require on-chip control of the polarisation state.

Chapter 5

Optical Vortex Emitters with Arbitrary Polarisation

Optical vortices (OVs) consist of a class of optical modes with phase variation or rotating polarisation around the central axis (i.e. these are light beams with an azimuthal component of the wave vector and helical phase). Due to the above property OVs have at least one singularity where the field cannot be defined, hence will be zero, often at the centre of the beam.

In 1992, Allen et al. discovered that photons in OVs can carry orbital angular momentum [140], which led to a number of applications in optical manipulation [141], imaging [142], optical communication [143] and quantum information [144, 145].

Currently, much of the manipulation, generation and detection is done with bulk optics such as spatial light modulators (SLMs) [146], sub-wavelength gratings [147], inhomogeneous birefringent elements [148], nano-antennas [149] and spiral phase plates (SPPs) [143, 150]. These optical components are either bulky and expensive or can only manipulate a single OAM state, without the ability for modulating states or switching between states.

In recent years, integrated optics enabled a major progress towards the demonstration of applications based on OVs thanks to the development of miniaturised, reliable and scalable components [151, 152]. Compact planar waveguide based Optical Angular Momentum (OAM) emitters can be easily interconnected via waveguides to detectors and lasers in large numbers to form complex and functional devices.

In this chapter, a theoretical study of the OAM emitters will first be given with particular emphasis on the polarisation state of the emitted beams. This will be followed by the design and fabrication of emitters in which the polarisation of the beams, either radial or azimuthal, can be controlled by integrating the novel Bragg gratings described in the previous chapter.

5.1 Introduction

Circular optical resonators, such as microdisks and microrings [150] are ideal integrated devices to emit OV beams. In fact, if a suitable periodic modulation of the refractive index is engraved into the waveguide of the circular resonators, the confined whispery gallery modes (WGMs) can be coupled to free space (Fig. 5.1).

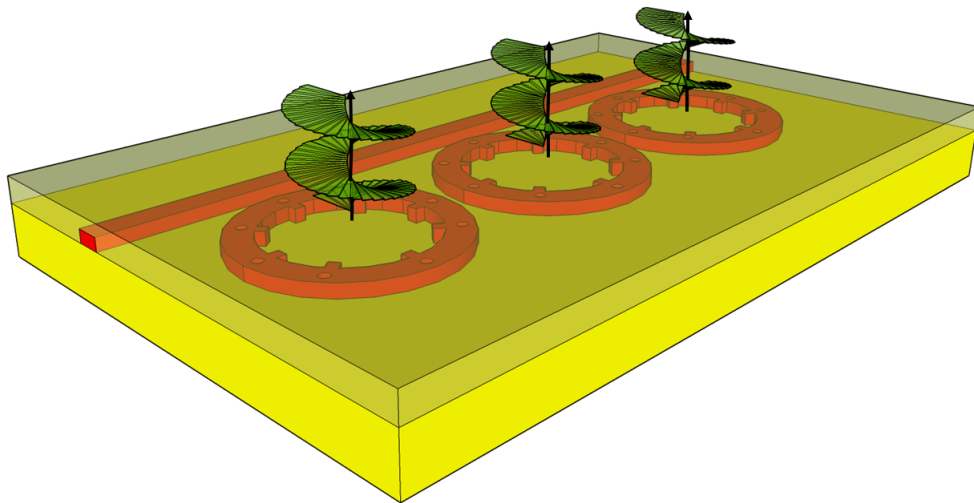


FIGURE 5.1: Illustration of the device with angular grating patterned along the inner and top wall of a microring resonator that is coupled to an access waveguide for optical input. The radiated beams are emitted orthogonally to the plane of the rings with a helical wavefront that depends on the periodicity of the grating.

The operation principle is similar to that of the surface gratings used to vertically couple the light from an optical waveguide to an optical fibre [147]. In fact, the grating elements scatter the guided mode to a certain angle ϕ , in which constructive interference occurs. If the grating is of the second order, the dominant scattered direction is orthogonal to the direction of propagation of the light (i.e.

orthogonal to the plane of the PIC as illustrated in Figure 5.3). By way of Huygens' principle, the wavefront will transform into a helix suggesting the creation of an OAM-carrying beam [153]. The order of the emitted OAM beam is dictated by a relationship between the wavelength of the beam, optical length of the resonator and periodicity of the Bragg grating. A more detailed analysis will be provided in the next section.

5.1.1 Phase-matching condition

In this section, we will provide the theoretical background to evaluate the coupling between the guided WGMs and the radiation modes. To do so the cylindrical coordinate framework (Fig. 5.2) is a natural approach for the theoretical treatment of the WGMs due to their cylindrical symmetry. The coupled mode theory (CMT) can be used to describe the coupling, where the grating elements can be considered a periodic variation of the dielectric constant responsible for coupling the WGMs to radiated modes. The dielectric constant can be written as:

$$\epsilon(\rho, z, \theta) = \epsilon_a(\rho, z) + \Delta\epsilon(\rho, z, \theta) \quad (5.1)$$

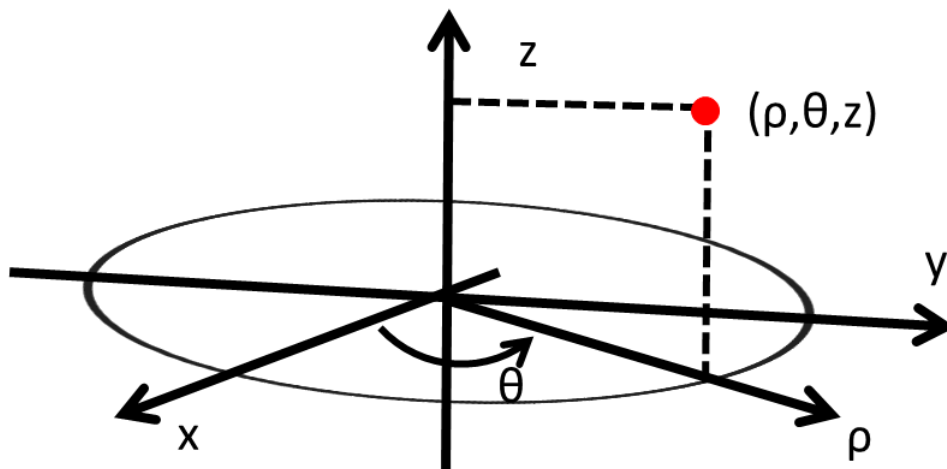


FIGURE 5.2: Schematic of the cylindrical coordinate framework used in the theoretical analysis presented in this section

In the waveguide plane, the z component of the magnetic and electric field satisfies the wave equation:

$$\left(\frac{\partial^2}{\partial \rho^2} + \frac{1}{\rho} \frac{\partial}{\partial \rho} + \frac{1}{\rho^2} \frac{\partial^2}{\partial \theta^2} + \frac{\partial^2}{\partial z^2} + k_0^2 n^2\right)_{E_z(\rho,\theta,z)}^{H_z(\rho,\theta,z)} = 0 \quad (5.2)$$

where n is the refractive index of the waveguide and:

$$\frac{H_z(\rho,\theta,z)}{E_z(\rho,\theta,z)} = R(\rho)\Theta(\theta)Z(z) = \sum_m A_m(\theta) \frac{H_m(\rho,z)}{E_m(\rho,z)} \exp[i(\omega t - v_m \theta)] \quad (5.3)$$

$$k_0^2 n^2 = \omega^2 \mu(\epsilon_a(\rho, z) + \Delta\epsilon(\rho, z, \theta)) \quad (5.4)$$

where ω is the angular frequency, $v_m = \beta_m R$ is the angular propagation constant and β_m is the propagation constant of the m^{th} eigenmode. The summation is taken over all eigenmodes, including the radiation modes and the coefficient A_m that depend on θ .

The axial dependence of the waveguide modal distribution in the vertical direction is given by:

$$\left(\frac{\partial^2}{\partial z^2} + k_0^2 n^2\right)Z(z) = \beta^2 \quad (5.5)$$

where β is the axial wave vector. The azimuthal dependence takes the form of:

$$\Theta(\theta) = \exp(-jq\theta) \quad (5.6)$$

with the topological charge $q = \frac{2\pi n R}{\lambda}$, where λ is the wavelength and R is the effective radius. Due to periodic boundary conditions, q is an integer and is related to the OAM quantum number (l). The radial dependence of the planar waveguide mode has the following form:

$$R(\rho) = a\mathcal{H}_l^{(1)}(\beta\rho) + b\mathcal{H}_l^{(2)}(\beta\rho) \quad (5.7)$$

where a and b can be defined by applying the continuity conditions at the interfaces.

Solving Equation 5.2 for the electric field with a slowly varying amplitude (SVA) approximation we obtain

$$\sum_m -2iv_m \frac{dA_m}{d\theta} E_m(\rho, z) \exp(-iv_m \theta) = -\omega^2 \mu \rho^2 \sum_n \Delta\epsilon(\rho, z, \theta) A_n E_n(\rho, z) \exp(-iv_n \theta) \quad (5.8)$$

and by taking the scalar product of the above equation with the electric field conjugate ($E_s^*(\rho, z)$), we obtain:

$$\langle s|s \rangle \frac{dA_s}{d\theta} = \frac{\omega^2 \mu}{2iv_s} \sum_n \langle s|\Delta\epsilon(\rho, z, \theta)\rho^2|n \rangle A_n \exp[i(v_s - v_n)\theta] \quad (5.9)$$

where

$$\langle s|s \rangle = \int E_s^*(\rho, z) E_s(\rho, z) d\rho dz \quad (5.10)$$

$$\langle s|\Delta\epsilon(\rho, z, \theta)\rho^2|n \rangle = \int E_s^*(\rho, z) \Delta\epsilon(\rho, z, \theta) \rho^2 E_n(\rho, z) d\rho dz \quad (5.11)$$

The perturbation of the dielectric constant on the θ direction can be expanded as a Fourier series:

$$\Delta\epsilon(\rho, z, \theta) = \sum_{g \neq 0} \epsilon_g(\rho, z) \exp(igq\theta) \quad (5.12)$$

where g is an integer. Substitution equation of 5.12 into equation 5.9 yields

$$\frac{dA_s}{d\theta} = \frac{\omega^2 \mu}{2iv_s \langle s|s \rangle} \sum_m \sum_n \langle s|\Delta\epsilon(\rho, z, \theta)\rho^2|n \rangle A_n \exp[i(v_s - v_n + gq)\theta] \quad (5.13)$$

In order to obtain the increment of the s^{th} field amplitude (ΔA_s), due to the mode coupling with the n^{th} mode, we integrate equation 5.13 over an arc much larger than the period (Λ) but much smaller than the variation of the field amplitude:

$$\Delta A_s = \frac{\omega^2 \mu}{2iv_s \langle s|s \rangle} \langle s|\Delta\epsilon(\rho, z, \theta)\rho^2|n \rangle A_n \int_{\theta R \gg \Lambda} \exp[i(v_s - v_n + gq)\theta] d\theta \quad (5.14)$$

For the coupling between the s^{th} and the n^{th} mode to different than zero, the following condition has to be satisfied:

$$v_s - v_n + gq = 0 \quad (5.15)$$

Because n is a guided WGM mode and as radiated mode, equation 5.15 can be rewritten as:

$$v_{rad} = v_{WGM} - gq \quad (5.16)$$

where $g = \pm 1, \pm 2, \dots$ is the diffraction order and equation 5.16 describes the angular phase matching condition. A large number of modes can satisfy the phase matching condition provided their angular wave vector matches some values of g , however, in practice g is limited by the material system.

As for the radiated mode in the free space, the wave vector ($\beta_{rad,\theta}$) needs to satisfy the following relation:

$$|\beta_{rad,\theta}| = \left| \frac{v_{rad}}{R} \right| < \frac{2\pi}{\lambda} \quad (5.17)$$

Also

$$\beta_{WGM} = \frac{v_{WGM}}{R} = \frac{2\pi}{\lambda} n_{eff} \quad (5.18)$$

Substituting equation 5.17 and equation 5.18 into equation 5.16 leads to

$$(n_{eff} - 1) \frac{\Lambda}{\lambda} < g < (n_{eff} + 1) \frac{\Lambda}{\lambda} \quad (5.19)$$

Because for silicon devices, λ is around 1550 nm, Λ is around 636 nm and n_{eff} is around 2.44. g is in the order of 0.6 to 1.4, and therefore the only possible value for g is 1. Using $v_{WGM} = p$ (the azimuthal order of the WGM), equation 5.16 can be rewritten as:

$$v_{rad} = p - q \quad (5.20)$$

By the engineering point of view, p is the number of optical periods around the resonator, q is the number of grating elements around the resonator and v_{rad} is the OAM order.

5.1.2 States of Polarisation of the emitted optical field

As discussed earlier, optical waveguides have two States of Polarisation (SOP), the quasi-TE mode, which is mainly parallel to the plane of propagation and the quasi-TM mode, which is orthogonal to the plane of propagation. The cylindrically symmetric SOPs of the radiated beam are a direct consequence of the cylindrically symmetric SOPs of the WGMs modes propagating in a circular cavity. More precisely, the superimposed radiation pattern emitted in free space will be determined by the SOP of the local optical field being scattered at each grating element. In highly confined waveguides such as silicon, the quasi-TE mode has a strong electric field in the azimuthal (propagation) direction, E_{az} [154], while the transverse electric field, E_T is weak and associated with large discontinuities.

Figure 5.3 shows the field distribution for the quasi-TE mode for E_{az} and E_T in a bent silicon waveguide that reproduces the situation experienced by a mode propagating in a microring resonator. The E_{az} component is predominantly located on the sidewalls of the waveguides, which explains why gratings fabricated on the sidewalls of the waveguide will emit beams with azimuthal polarisation. On the other hand, for the E_T component the main interaction of the field occurs with the top of the waveguide, therefore, by placing the gratings on the top of the waveguide, the emitted beam is radially polarised. This suggests that the gratings developed in this thesis and presented in Chapter 4 can be used to engineer the SOP of the emitted beam.

In the design of the top grating the E_T mode profile is the more relevant because of the much stronger interaction of the field with the top surface of the waveguide.

5.2 Device Design

As part of this work, top grating elements were designed in the attempt to produce radially polarised OAM beams. For the design of the grating elements, the physical

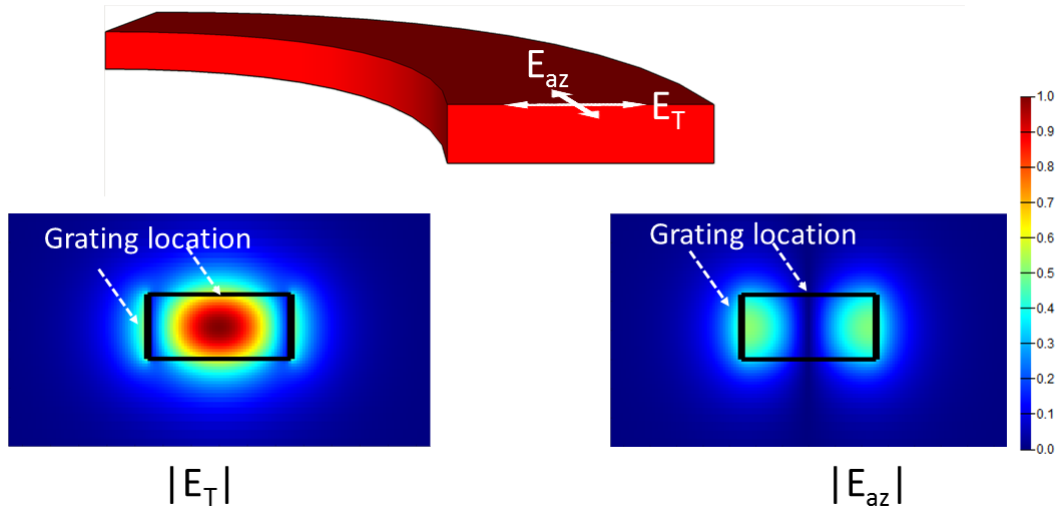


FIGURE 5.3: Waveguide geometry (top) and simulated field distribution of the transverse electric field E_T and azimuthal electric field E_{az} for the quasi-TE mode in a single mode silicon waveguide at 1550 nm (bottom). A grating placed on the side of the waveguide would produce a predominantly azimuthal polarised emission, whereas a grating placed on the top would produce radially polarised emission. By using both sidewall and top grating, it is, therefore, possible to engineer the SOP of the emitted light.

principles and design rules developed in Chapter 4 were used. The Bragg period was calculated based on the effective refractive index of the waveguide, and a resonator radius R of 20μ was chosen as a compromise between compact footprint and negligible the bending losses. For such bending radius, the effective refractive index of the mode propagating in the ring can be assumed to be the same as that of a straight waveguide, i.e. $n_{eff} = 2.44$. The OAM order $l = 0$ was designed to be at $\lambda = 1550$ nm, which translates into a period $\Lambda = 636$ nm and $q = 198$ (number of gratings elements).

The geometry of the gratings is squared/rectangular, as this allows to easily vary the grating strength by either controlling the grating width or amplitude. Figure 5.4 shows a 3D illustration and a top view of an OAM emitting device engineered for azimuthal polarised emitted OAM modes. The grating perturbation is defined on the inner sidewall to minimise the perturbation with the coupler to the bus waveguide.

Following the same design rules used for the sidewall gratings, the period for the top gratings was chosen as the arc connecting the centre between two consecutive grating elements. For controlling the strength of the gratings, either the radius or the etching depth of the circular elements forming the gratings can be changed.

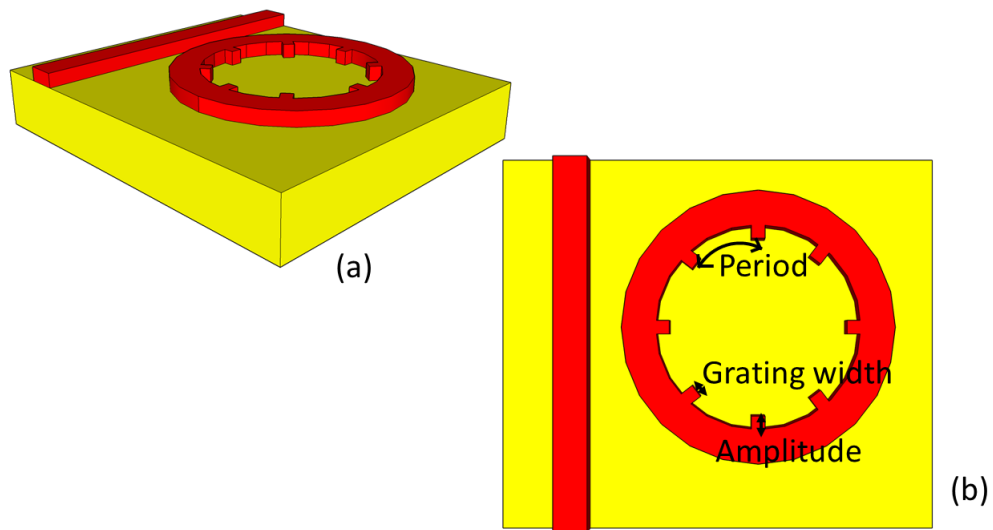


FIGURE 5.4: Schematic illustration of a ring coupled to an access waveguide and with gratings defined on the inner sidewall (a) 3D illustration and (b) top view.

Even with the use of e-beam lithography, a radius below 30 nm is technologically challenging, and the variation between holes can be significant. As a consequence, the minimum radius of the gratings was chosen to be 30 nm, while the maximum is limited by the dimensions of the waveguide, $r_{max} = 250$ nm. In order to minimise the losses induced from the holes etched in the waveguides (Figure 4.14), as discussed in Chapter 4, and to avoid large variations in the effective index of the waveguide, a shallow etched design was chosen with a maximum depth of 40 nm. Figure 5.5 shows a 3D illustration and the top view of the devices designed for the radially polarised emitted OAM modes.

5.3 Experimental work

Several devices for emitting radially polarised beams were designed and fabricated by the fabrication process described in Chapter 2.

The complete process flow included the initial e-beam lithography definition of circular gratings with positive resist ZEP. The gratings were shallow etched to a depth 40 nm before the resist was stripped with a combination of oxygen ash and 1165 stripper. In order to ensure uniformity between the various devices with different radius, devices with a radius of 30 nm, 40 nm and 50 nm only designed

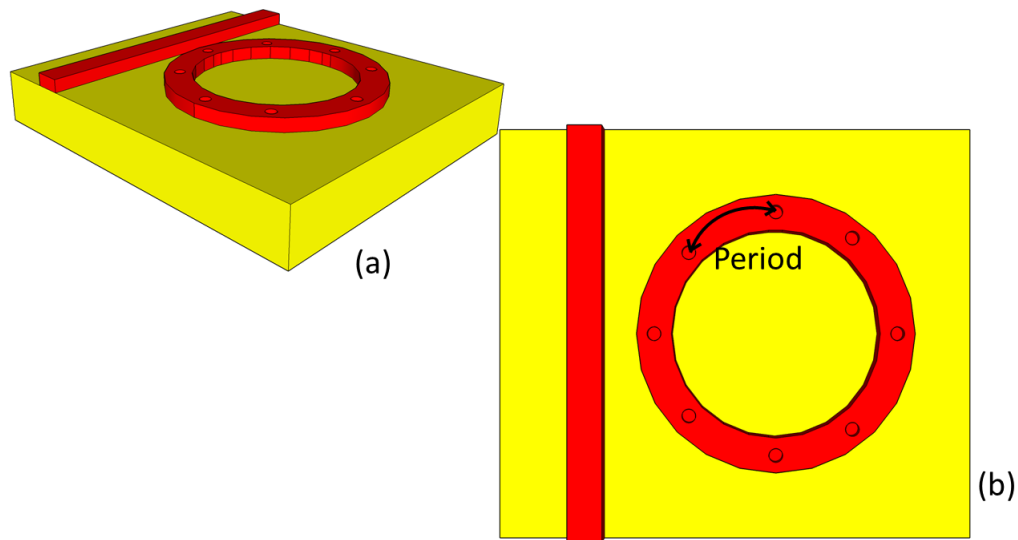


FIGURE 5.5: Schematic illustration of a ring with gratings on the top coupled to an access waveguide (a) 3D illustration and (b) top view.

and fabricated originally. Devices with greater radii up to 120 nm were fabricated in a separate lithographic and etching run. A second lithographic step was then performed with a negative resist (HSQ) for the definition of the microrings and the waveguides. For enhancing the coupling to optical fibres, polymer (SU8) couplers were fabricated on the edges of the chip as described in Section 3.2. A film of HSQ and a layer of PECVD silica were deposited as an upper cladding.

5.3.1 Experimental set-up

Figure 5.6 shows the experimental set-up used to characterise the near and far field profile of the emitted beams. The light from a tunable laser is coupled into the polymer waveguide with the use of a polarisation maintaining fibre after the light is passed through an in-line polariser with 25 dB extinction ratio between the TE/TM mode. To characterise the near field, the emitted light was collected by a Molded Lens (ML) and passed through an Iris (IR) before a Beam Splitter (BS) directed part of the light towards a Mirror (M) with an antireflection coating at 1550 nm. The mirror can be flipped to either direct the beam to an Infrared Camera (IC) for imaging its profile and to a Photo Diode (PD) for measuring its emitted power. In order to analyse the SOP of the emitted beam, a linear polariser is used before the iris.

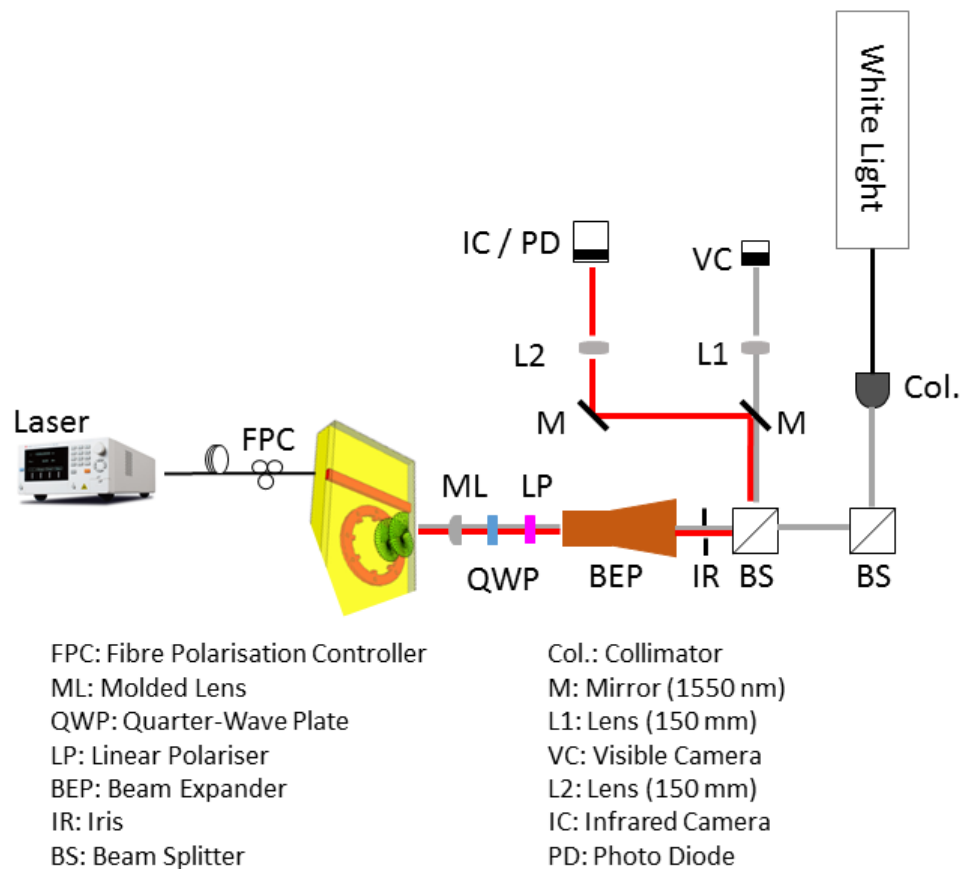


FIGURE 5.6: The experimental set-up for measuring the phase structure for the radiated beam from the silicon chip.

The same set-up was used to image the profile of the emitted field in the far field with the addition of a Beam Expander (BEP) before the iris. A Quarter-Wave Plate (QWP) was also added before the BEP. With the QWP adjusted either to -45° or $+45^\circ$ the left-hand circularly polarised (LHCP) and right-hand circularly polarised (RHCP) beam profile of the far field can be observed.

For easier alignment, a white source was used to illuminate the sample. The light from the white source was collimated by a Collimator (Col.) and directed to the sample through two BSs and the molded lens. The red and grey lines in Figure 5.6 indicate the infrared and white light path, respectively.

5.3.2 Measurements

Three different sets of measurements were performed on the fabricated devices. Initially, the devices were characterised with the set-up described in Section A.3

and shown in Figure A.1. The light from a tunable laser was coupled into the input waveguide with a PM lensed fibre, and collected from an objective lens before the output power was recorded by a photodiode. The coupling losses of the devices were measured at 2 dB per facet, and the propagation losses were found to be 1.5 dB/cm.

Figure 5.7 shows the optical spectra for a simple ring (blue line), for a device with 30 nm radius gratings (green line) and 40 nm radius gratings (red line) with a coupling gap between the bus waveguide and the ring of 100 nm. For devices with larger radius gratings, no clear resonances could be recorded. This was the consequence of the excessive strength of the gratings that translated into a large increase of the round trip propagation losses and a decrease of the resonator quality factor.

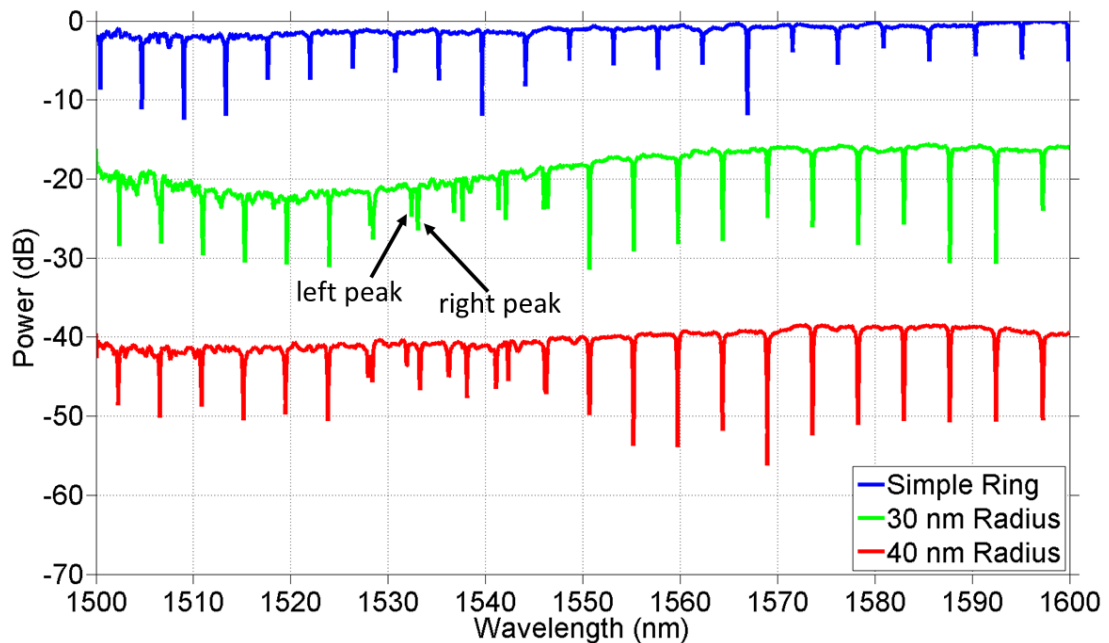


FIGURE 5.7: Radiation spectrum for a single ring device (blue line) and devices with 30 nm and 40 nm radius top gratings (green and red line). The spectra were shifted downwards for easier reading.

When inspecting the spectra of the resonators containing the gratings and comparing them to that of the single ring, distinct resonance splittings can be seen around a wavelength of 1535 nm. This is a typical feature of the OAM ring emitters that occurs at a resonant corresponding to the OAM order $l=0$. In fact, the emission of an OAM mode at $l=0$ is perfectly vertical to the plane of the chip and causes cross-coupling between the degenerate clockwise (CW) and counter-clockwise (CCW) WGMs in the resonator. Because the mode $l=0$ was designed to

emit at a wavelength of 1550 nm, there is a deviation between the calculated and measured Bragg wavelength of approximately 1%, which is within the error tolerance of our fabrication process. It is worth noting that the double peak feature on devices with sidewall gratings is usually observed at $l = 0$ only [151], whereas in these devices $l = \pm 1$ and $l = \pm 2$ also show a similar behaviour. The fact that the CW and CCW modes are coupled for resonances other than $l=0$ suggest that the top gratings are far stronger than anticipated.

Following the initial characterisation of the devices, the devices were aligned to the set-up described in Section 5.3.1 and shown in Figure 5.6 for near and far field beam profile measurements. Only devices with gratings elements with a radius of 30 nm and 40 nm were further characterised as they show clear resonances.

The emitted light was collected by a molded lens and imaged on a Hamamatsu infrared camera. Figures 5.8 and 5.9 shows the near-field intensity pattern of two rings with gratings of 30 nm and 40 nm and for two different values of the OAM order l . The top part of the figures shows the field intensity of the unpolarised light emitted by the two devices tuned at values $l = 4$ and $l = -3$ for the 30nm radius device (Figure 5.8) and $l = 5$ and $l = -4$ for the 40nm radius device (Figure 5.9).

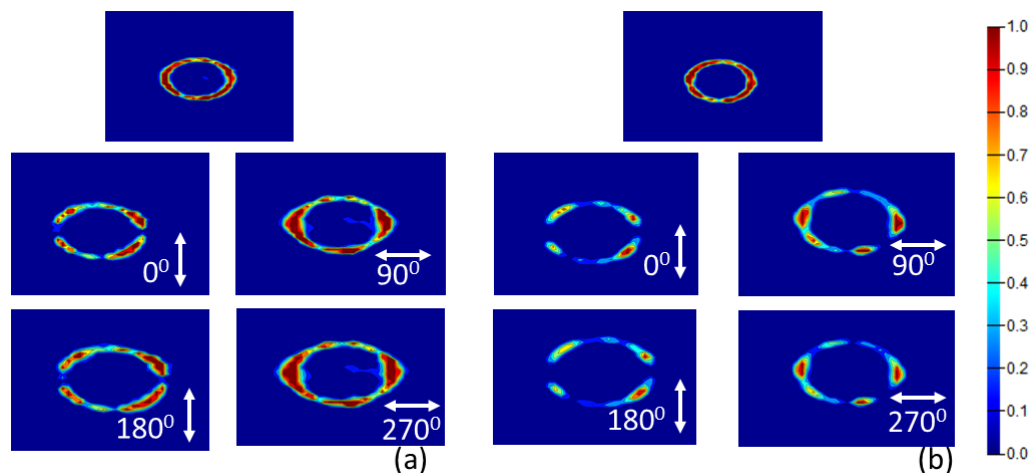


FIGURE 5.8: The unpolarised near field profile (top) and the orthogonal linearly polarised field profile for devices with 30 nm radius top gratings at a wavelength of (a) 1520 nm and (b) 1551 nm. At any point the SOP is predominantly radial.

The near-field intensity pattern shows a non-uniform distribution of the emitted power along the circumference of the ring, with the maximum output power approximately located at 90° and 270° relative to the x-axis.

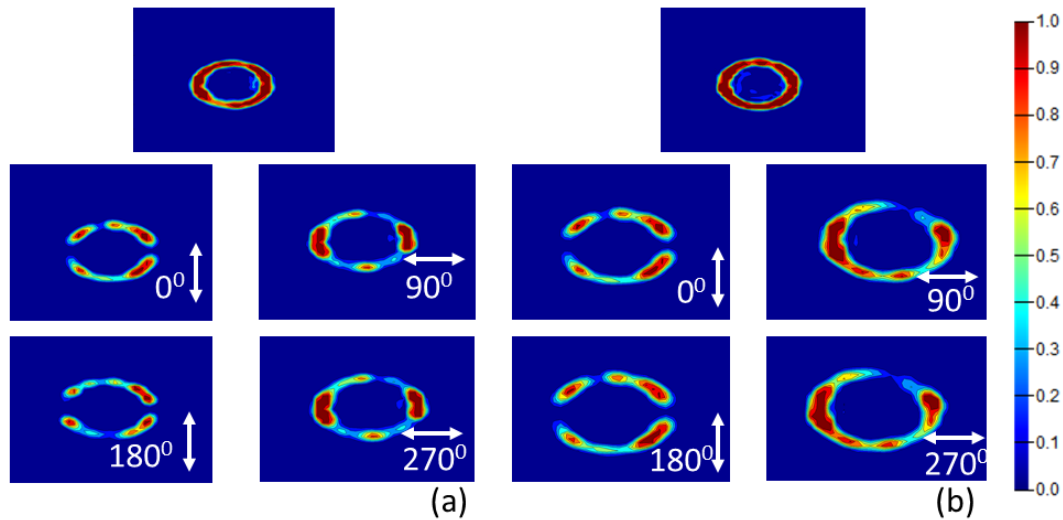


FIGURE 5.9: The unpolarised near field profile (top) and the orthogonal linearly polarised field profile for devices with 40 nm radius top gratings at a wavelength of (a) 1515 nm and (b) 1556 nm. At any point the SOP is predominantly radial.

A linear polariser was added after the molded lens, with the axis of polarisation rotated at 0° , 90° , 180° and 270° relative to the y-axis, and the output intensity pattern was recorded with the infrared camera as shown in Figures 5.8 and 5.9. Although the recorded data confirm a predominantly radially polarised emitted beam, the substantial field intensity is still present in the azimuthal direction. The reason for this non-ideal behaviour can be explained by inspecting the bottom of Figure 5.3 that shows the field profile in the ring waveguide. While mainly the E_T component of the field interacts with the top of the waveguide, there is also some interaction of the E_{az} component with the top of the waveguide. The stronger the top elements of the gratings, the higher the interaction of the E_{az} component becomes, which leads to an increase in the azimuthal polarisation. These measurements confirmed that the fabricated top gratings are too strong and as such, they generate non-uniform emitted beams with residual azimuthal polarisation.

The final set of measurements was the imaging of the far field intensity pattern. To do so, a beam expander and a quarter wave plate were added after the molded lens as shown in Figure 5.6. The measurements were focused on the devices with the 30 nm radius gratings due to the better uniformity of the near-field intensity and highest polarisation purity of the emitted beam.

The radiated beams can be described as the superposition of two orthogonal

scalar vortices consisted of a left-hand circularly polarised (LHCP) with topological charge $l-1$ and right-hand circularly polarised (RHCP) with $l+1$. When the radiated beams interfere with a reference beam, an interference pattern should be produced with the number of arms to be $l+1$ and $l-1$ for RHCP and LHCP respectively [151].

Initially the far field profile without the interference of a reference beam was recorded as shown in Figure 5.10 for devices with 30 nm gratings and for $l = 3$, $l = 0$ for the left peak, $l = 0$ for the right peak and $l = -3$. By rotating the quarter-wave plate at -45° , relative to the positive y-axis, LHCP was recorded (top of Figure 5.10), and when the QWP was rotated at 45° the RHCP was measured (bottom of Figure 5.10).

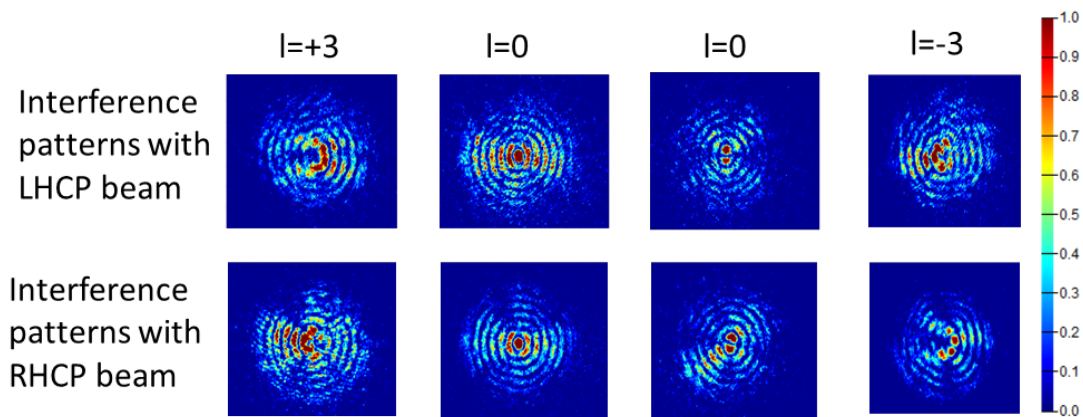


FIGURE 5.10: The far field image of the LHCP (top) and RHCP (bottom) for devices with top gratings with radius of 30 nm and wavelengths 1524 nm, 1537 nm (first split), 1537 nm (second split) and 1551 nm from left to right respectively.

For $l = \pm 3$ the imaged far field profile is a centrosymmetric pattern with a zero intensity in the middle. However, the field intensity is not uniform all around the ring. The strength of the gratings is too high, and as a result, the mode cannot fully resonate inside the ring. Similarly, for $l = 0$ centrosymmetric circles were observed with the maximum intensity in the middle of the ring (for the right peak the centre ring is split into two semicircles). Again depending on whether the LHCP or the RHCP is observed, the power is stronger in one part of the ring only. Due to this uneven power intensity of the rings, no experiment was performed with the interference of a reference beam as not spiral pattern could be detected.

Although a clear indication of a radially polarised emitted beam has been recorded, no clear evidence has been found that these beams carry OAM modes. The uneven distribution of the field as well as the complex wavelength spectrum of the resonator (mainly due to the presence of several split peaks), led to inconclusive results for the emitted beams.

In order to obtain emitted beams with more uniform distribution, the gratings need to be much weaker. This was not completely appreciated at the time these devices were fabricated as the understanding of the top grating behaviour, and OAM ring emitters was still superficial.

While many works have explored the SOP in the presence of sidewall gratings, both theoretical and experimental [151, 155] limited studies have been performed so far for the top gratings [156, 157] due to the non-availability of adequate modelling software and challenging fabrication. By the end of this project, the 3D FDTD simulation package from Lumerical became available in the group, and some simulations were performed to confirm the results. Figure 5.11 shows 3D-FDTD simulations of the SOPs for devices with the same top grating and ring dimensions of the fabricated devices (i.e. the radius of 30nm and depth of 40 nm). From left to right the total intensity distribution, the intensity of $|E_x|^2$ and the intensity of $|E_y|^2$ only of an emitted beam with $l=-1$ (i.e. $l = v_{rad}$) are shown. The simulations confirm that top gratings emit a predominantly radially polarised beam. However, the noisy intensity patterns and uneven field distributions in Figure 5.11 confirm the excessive strength of the gratings.

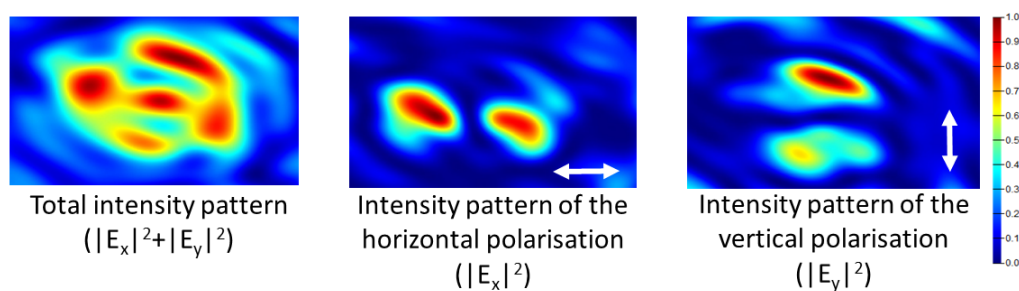


FIGURE 5.11: The 3D-FDTD simulation results of the intensity patterns for a radiated beam that is scattered by a top grating. When the total intensity (on the left) is decomposed into the two orthogonal linearly polarised beams, the SOP at any point is radial.

5.4 Conclusion

This chapter presented the design and fabrication of optical vortex emitters based on a microring resonator integrated with a Bragg grating. Previous devices were constructed with sidewall grating geometries that emitted azimuthally polarised beams. The main aim of the work presented in this chapter was to integrate the top grating devices developed in Chapter 4 on the resonator waveguide so as to emit radially polarised beams.

The experimental results showed that the emitted beams had a predominantly radial polarisation, although azimuthal components were still present and the beam was not completely uniform, which did not allow to confirm the presence of optical angular momentum. The main reason was the excessive strength of the gratings, which was independently confirmed by experimental measurements and theoretical simulations.

The strength of the grating can be reduced by either decreasing the radius or the depth of the hole element forming the grating. However, both solutions are very difficult to implement from a technological point of view because they require extreme control over both e-beam lithography and dry etching. An alternative approach is to use a material platform with lower refractive index confinement such as silicon nitride so as to decrease the interaction of the mode with the gratings. A further solution is to engrave the grating in the upper cladding layer rather than in the guiding waveguide core. All the approaches would have required major design and technological developments, and therefore they were not investigated further.

Chapter 6

Conclusion

The main objective of this thesis was on the development of integrated Bragg grating device that could independently manipulate the TE and the TM polarisation. This work was accompanied by a substantial activity on SOI process and component optimisation that was required to maximise the performance of the developed devices. The main achievements are summarised in the following sections.

6.1 Fabrication techniques

A significant amount of time of this work has been spent for the optimisation of the silicon photonic fabrication process. The need for devices of increasing level of complexity both in terms of minimum critical dimensions and number of components per chip demands a reliable and repeatable fabrication process.

One of the primary focus of this work was the optimisation of the e-beam lithographic process with HSQ, which offer excellent line edge roughness and short writing times. With good control over the EBL dose and mask fracturing process as well as deep understanding of the process parameters such as dilution and ageing of the resist, it was possible to obtain repeatable sub-wavelength features as small as 6 nm.

Alternative resist processes such as ZEP and SU8 were also developed. Although both of these processes are well-known by the SOI community, they were not well assessed in the JWNC and as such demanded some careful optimisation. The ZEP process allowed us to fabricate uncovered waveguides, which are required for

applications such as sensing, with losses at the same level as those obtained with the HSQ process. The SU8 resist process is an important component of our SOI process flow as it is used to define the large waveguides that facilitate the coupling to the input/output optical fibres. The main challenge here arose from the very high sensitivity of the resist and the poor control over the spun thickness.

While the chemistry to dry etch silicon was not modified during this work, the repeatability of the process was improved, and various tests were performed to ensure the reproducibility of the results over time. Repeatable propagation losses as low as 1 - 1.5 dB/cm were obtained during the whole duration of this thesis, mainly due to the smoothness of the etching mask, the standardisation of the chip size and the proper setting of the various machine parameters. Due to the stability of the process, devices with shallow etched features of 40 nm with a deviation of less than 2 nm were systematically fabricated. A final task of the etching development was the transfer of the process to a new Estrelas etching tool, which is still an on-going activity as the new machine has shown a number of issues in terms of stability and reliability.

Finally, the quality of the upper cladding was ensured with the optimisation of the deposition of a HSQ and PECVD silica by-layer. Of particular importance here was the very accurate control over the film thickness as this has a major impact on the design of the metallic heaters and the TM absorbers discussed in Chapter 4.

6.2 Components Design

The second main activity of this work was on the design and optimisation of a number of key device components, such as thermo-optic modulators, inverse taper couplers, sub-wavelength waveguide and silicon membranes.

The design optimisation of a thermo-optic modulator based on a NiCr heating element provided record power efficiency as low as 12 mW per π -shift. This was the result of a thorough theoretical and experimental study on the optimal dimensions and position of the metallic film.

Initially, the silica top cladding thickness was optimised so as to minimise the impact on the losses from the metal strip. Then, the dimensions of the heater

were optimised, either for maximum tuning range or tuning efficiency. An optimal heater geometry of $50 \text{ nm} \times 2 \text{ }\mu\text{m}$ and $50 \text{ nm} \times 900 \text{ nm}$ were found for the first and second case, respectively. It was also found theoretically that thinner heater cross sections might provide further improvements as a larger fraction of their heat can be delivered to the silicon waveguide. A careful optimisation of the uniformity of very thin metallic films is currently being performed.

Finally, the effect of cladding the NiCr heater was examined. While no appreciable differences were found on the performance of the heaters, the additional cladding layer improved the long-term stability of the device and its robustness against environmental fluctuations.

Following the work on the thermo-optic modulator, the geometry for the inverse taper coupler was completely re-designed. Previously, the standard cross-section of the polymer waveguide used in Glasgow was $2 \text{ }\mu\text{m}$ in height and $2.5 \text{ }\mu\text{m}$ in width. While this geometry gives excellent coupling to the silicon waveguide, it is not ideal in the matching the optical fibre mode. This resulted in fairly high losses of up to 5 dB/facet. Moreover, simulations indicated that these dimensions are very close to cut-off and therefore propagation losses were in the order of several dB/cm. This was not an issue if very short polymer waveguides were used but severely limited the applicability of this waveguide technology in devices requiring long polymer waveguides.

As a result of simulations, the optimum dimension of the polymer was found to be $3.5 \text{ }\mu\text{m}$ in height, and $4 \text{ }\mu\text{m}$ in width, with a taper length of $300 \text{ }\mu\text{m}$. Insertion losses as low as 2 dB/facet and 1 dB/facet for the TE and TM mode respectively were measured on a fabricated devices. One conclusion of this activity was that SU8 is not an ideal choice because of the poor fabrication control over its thickness. Alternative materials such as low-stress SiN or SiON should be considered as a future work.

The effect of the misalignment between the polymer and the silicon waveguide was also examined. While it was found that the TM mode is robust to the misalignment, the TE mode can be significantly affected, which resulted in insertion losses as high as 6 dB/facet with a 500 nm of misalignment. A far more critical consequence of such misalignment was the strong polarisation rotation that can be as high as 30 deg.

The final components examined were sub-wavelength and slot waveguides for applications in sensing and non-linear optics. Specifically, slot waveguide and SWG designs were developed to explore surface-induced second-order non-linearities in silicon photonics. These waveguides are currently being tested as part of another research project.

6.3 Polarisation selective devices

The final part of this work was devoted to the design and evaluation of polarisation selective devices focused on Bragg grating geometries and to their application in optical filters and optical vortex emitters.

In the initial part of the work, devices containing well-assessed sidewall gratings were assessed with the objective of evaluating their behaviour in terms of polarisation. It was found that the strong polarisation scattering occurring in these waveguides poses a hard limit of 30dB in the maximum extinction ratio that can be obtained, regardless of the length or strength of the grating.

This issue was addressed with the design of two TM filter geometries, the first consisting of a simple metallic strip, the second of a grating defined on the top of the waveguide. Both geometries are very effective on the TM mode only and do not add substantial losses to the TE mode. When both TE and TM designs were integrated on the same waveguide, filters with ER as high as 60 dB were measured. Because this value is limited by the strong substrate scattering, improved designs can be developed to further increase this ER figure by at least 20dB.

The same top grating geometry developed for the filters was transferred to microring resonators for the emission of optical vortex beams. The final objective here was to combine on the same waveguide both the sidewall and top grating designs so as to engineer the state of polarisation of the radiated beam. Although the experimental results indicated the presence of radial components generated by the top grating, it was found that the strength of the grating was far too high to keep a uniform shape of the emitted beam. This device can be substantially improved thanks to the more solid understanding gained on the top grating geometry and with the technological advantages offered by the new dry etching tool. Unfortunately, time constraints did not allow to further develop this device.

Appendix A

Origin and Extraction of Optical Losses

A.1 The origin of optical losses

A significant aspect of the design of an integrated photonic circuit is the evaluation of the propagation losses as these have a substantial impact on the performance of the device. In integrated waveguides, the total losses α_{tot} are the sum of three different type of losses, the scattering losses (α_{sc}), the absorption losses (α_{ab}) and the radiation losses (α_{rad}).

$$\alpha_{tot} = \alpha_{sc} + \alpha_{ab} + \alpha_{rad} \quad (\text{A.1})$$

Each type is explained below in more detail.

A.1.1 Scattering Losses

The scattering losses are themselves divided into two categories, the volume and the interface scattering losses. The volume scattering losses arise from defects in the material such as dislocations, voids and contaminant atoms. These are usually negligible due to the high quality of the SOI wafers.

The interface scattering losses are generated by the interaction of the propagating beam with the roughness of the interfaces between the waveguide core and the surrounding claddings. However, the interfaces on the sides of the silicon waveguide are defined by lithography and dry etching and, therefore, might exhibit a substantial degree of roughness. The following formula can be used to approximate the scattering losses:

$$\alpha_{sc} = \frac{\sigma^2 k_0^2 h}{\beta} \frac{E_s^2}{\int E^2 dx} \Delta n^2 \quad (\text{A.2})$$

where σ is the interface roughness, β is the propagation constant, k_0 is the free space wavenumber, $\Delta n = (n_1^2 - n_0^2)/(2n_1^2) \approx (n_1 - n_0)/(n_1)$ [158] is the difference in the refractive index between the core and the cladding, h is the transverse propagation constant and $E_s^2/\int E^2 dx$ is the normalised electric field.

Reducing the surface roughness is essential because of its quadratic impact on the propagation losses. Also, it is worth noting the quadratic dependence of the losses on the difference in the refractive index between the core and the cladding. This implies that a reduction of modal confinement has a substantial impact on the losses.

A.1.2 Absorption Losses

The absorption losses are also divided into two categories, the band absorption and the free carrier absorption. The band absorption occurs when the energy of the photons exceeds the bandgap energy of the semiconductor. Because the bandgap of silicon is around $1.1\mu\text{m}$ the absorption losses at the $1.55\mu\text{m}$ telecom wavelength is entirely negligible (0.004 dB/cm [159]). Two-photon absorption (TPA) becomes an important loss mechanism only for power levels of several tens of milliwatts.

The interaction of photons with free carriers in the semiconductor gives an additional contribution to the absorption losses. These losses become critical in the presence of pin junctions that are typically used as fast modulators or for high levels of powers that generate free carriers through two-photon absorption processes. For the material under investigation, these losses are low due to the low doping of the material. This phenomenon is adequately described by the DrudeLorenz equation [160].

$$\Delta\alpha = \frac{e^3\lambda_0^2}{4\pi^2c^3\epsilon_0n} \left(\frac{N_e}{\mu_e(m_{ce}^*)^2} + \frac{N_h}{\mu_h(m_{ch}^*)^2} \right) \quad (\text{A.3})$$

where λ_0 is the free space wavelength, ϵ_0 is the permittivity of free space, c is the velocity of light in vacuum, e is the electronic charge, m_{ch} and m_{ce} are the effective masses of holes and electrons respectively, μ_h and μ_e are the hole and electron mobility respectively, N_h is the free-hole concentration and N_e is the free-electron concentration.

A.1.3 Radiation Losses

The radiation losses originate from the coupling of the guided modes to radiation modes. Usually, these losses are low. However, they need to be taken into account in ring resonators with small curvature radii (i.e. bending losses) or in very narrow waveguides that operate close to cut-off. Also, the thickness of the lower cladding plays an essential role in the radiation losses as the mode can radiate into the substrate if the cladding thickness is below $2 \mu\text{m}$ [158, 161].

A.2 Extraction of Propagation losses

As stated before, the assessment of the waveguide losses is key to optimise the fabrication parameters and evaluate the performance of the device. Many methods have been proposed to extract the propagation losses from experimental data.

A.2.1 Cut-back Technique

The simplest method is the cut back technique [14]. The output optical power from a known length waveguide is first measured. Then the sample is reduced in length, and the output optical power is measured again. If this is repeated a few times, a graph of the power against the length can be plotted, the gradient of which provides the value for the propagation losses. The requirement for successive cleaving of the sample makes this technique effective only for waveguides with low propagation losses where very long samples can be used. Also, the accuracy of the method strongly relies on having the same input power coupling between successive

measurements. Depending on the quality of the cleaved facets and on the stability of the setup this might not always be the case.

In order to avoid the problem of multiple cleaving and the variability in coupling depending on that, spiral waveguides with a length of 2.1 cm to 7.1 cm were designed and fabricated. The fabricated devices are shown in figure ??.

A.2.2 Fabry-Perot method

An alternative method is based on the evaluation of the transmission fringes formed by the Fabry-Perot cavity when scanning the wavelength of the input optical signal [162]. This technique uses the Fourier transforms of the transmitted optical signal to extract the losses. Compared to the cut-back, the Fabry-Perot approach is more robust as it is independent of the coupled optical power but does not yield accurate results in the presence of very low losses. Although many theoretical studies have been presented for improving this method [163] with low losses, its accuracy quickly degrades for propagation losses below 1dB/cm.

Because typical loss values in silicon waveguides vary between 1dB/cm and 3-4 dB/cm, both techniques can be used. As part of this work, both methods were implemented.

A.3 Optical set-up

The assessment of the losses as well as the evaluation of the transfer function of a photonic integrated circuit requires an experimental setup that consists of a tunable laser emitting in the range of 1550nm, a lensed fibre, a photodiode, a lock-in amplifier and very stable mechanical micro-positioners to align the waveguides to the fibre or lens. The full experimental set up can be seen in Figure A.1.

An in-line polariser was used to polarise the laser light with a minimum extinction ratio of 20 dB between the TE/TM mode as shown in Figure A.2. The light was coupled through a lens fibre into the chip placed onto a mechanical positioner with sub-micron resolution. The output light was collected by a lens and collimated into the photodiode which is connected to a lock-in amplifier and a computer to record the data. The output of the laser was modulated at a few hundreds of

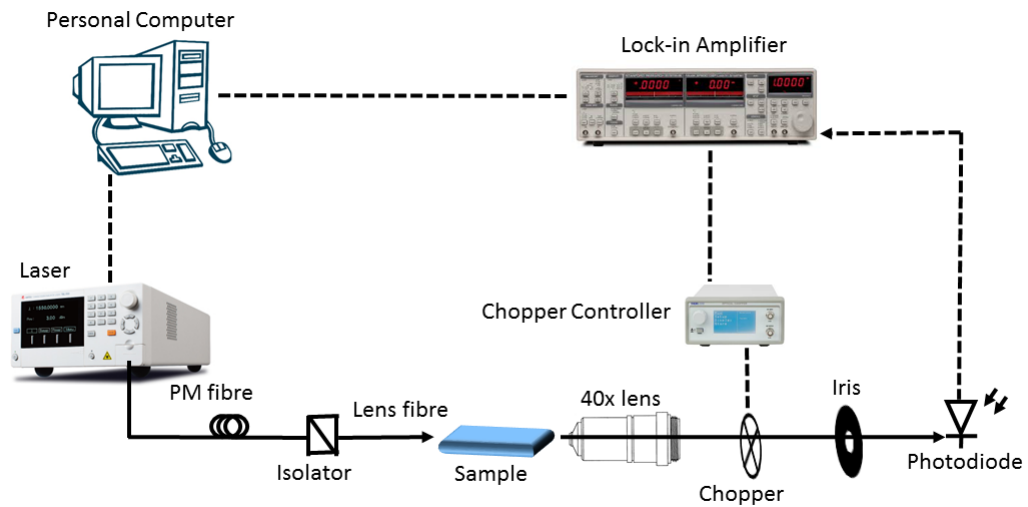


FIGURE A.1: Sketch of the experimental set-up employed for the end-fire characterisation of devices fabricated in SOI.

Hz using a chopper. The whole set-up was controlled by a program written in LabView that sets the laser parameters (power, wavelength, scanning range, step size, etc.), the lock-in (integration time, dynamic range, etc.) and collects the data. The output power usually used for the measurements was 1 mW.

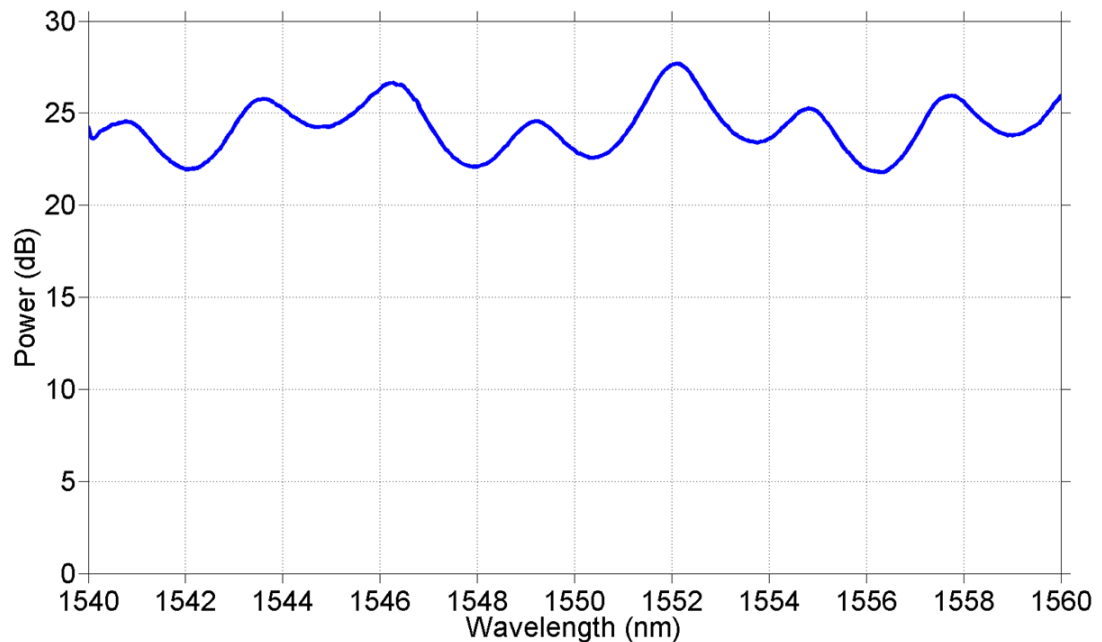


FIGURE A.2: The extinction ratio between the TE and TM measured after the polariser.

Appendix B

Simulation Techniques

As part of this work, several optical components had to be designed and optimised. In order to define the optimum design to be fabricated, the components were optimised through theoretical models and simulations.

Here, the methods used for these simulations will be presented and discussed.

B.1 Solvers

In order to simulate and theoretically examine optical components, several solvers have been developed over the years. In this section, solvers from three commercial software companies (Lumerical [164], BeamProp [165] and Comsol [166]) will be presented and explained.

Finite-Difference Eigenmode (FDE) is a mode calculator solver available on the commercial software Lumerical Mode solutions [112], which uses Yee's 2D mesh and an index averaging technique as described by Zhu and Brown [167] to calculate the spatial profile and the mode frequency by solving Maxwell's equations on a cross-sectional mesh of the waveguide. The mode profile, effective index, losses, dispersion and group delay of the waveguide can be calculated with this mode solver. Also, the solver has the ability to simulate bent waveguides.

An alternative method for calculating the mode profile and the effective index of the waveguide based on finite difference method is described by Fallahkhair [113].

The technique is based upon the transverse magnetic field components, and it is available as a toolbox in Matlab [168].

Beam Propagation Method (BPM) is based on a fast Fourier Transform method applied on the Helmholtz equation under a slowly varying envelope approximation. The model assumes a stationary field at plane A ($z = z_k$) and uses it to determine the field at plane B ($z = z_k + \Delta z$), where z is the propagation axis [169].

By implementing a stepwise propagation, it is possible to minimise the simulation requirements. On the other hand, the stepwise method and the slowly varying envelope approximation are the main limitations of the technique. In fact, the simulations assume only forward propagation and any reflected waves are neglected from the calculations. Also, the second order differential quotient is neglected with the assumption of a small refractive index difference.

A BPM developed by BeamProp from RSoft [165] was initially used in this work, however, due to the limitation of the techniques and the high index contrast nature of the SOI material, this method was abandoned.

2/3D Finite-Difference Time-Domain (FDTD) [170–172] solves the Maxwell's curl equations (B.1, B.2, B.3) in non-magnetic materials on a discrete spatial and temporal grid.

$$\frac{\partial \mathbf{D}}{\partial t} = \nabla \times \mathbf{H} \quad (\text{B.1})$$

$$\mathbf{D}(\omega) = \varepsilon_0 \varepsilon_r(\omega) \mathbf{E}(\omega) \quad (\text{B.2})$$

$$\frac{\partial \mathbf{H}}{\partial t} = -\frac{1}{\mu_0} \nabla \times \mathbf{E} \quad (\text{B.3})$$

The electromagnetic field components (E_x , E_y , E_z and H_x , H_y and H_z in three dimensions) are solved at a given instant in time for a given volume of space. This is followed by solving the equations for the next instant in time, and the process is

repeated until the desired transient, or steady-state electromagnetic field is fully evolved.

Being a direct space and time solution of the Maxwell equation, it can offer a very deep insight into a number of parameters and quantities, such as the complex Poynting vector and the transmission/reflection of light as well as frequency-domain solutions by exploiting Fourier transforms [164]. On the drawback, a high-resolution mesh is required for obtaining accurate simulations, which increases the computational requirements. As a result, only small areas can be simulated to keep the simulation time at reasonable levels.

In the University of Glasgow, an FDTD solver was offered through the commercial software "Lumerical FDTD" [173]. As part of this work, FDTD was used for the initial simulations for the design of the Bragg grating filters and OAM emitters.

2.5 FDTD (varFDTD) is based on collapsing 3D geometries into a 2D set of effective indices which can be solved with 2D FDTD [164]. The vertical slab modes are identified, and the effective index of them is calculated before the 3rd dimension of the waveguide is collapsed, and the problem is solved as a 2D FDTD based on a variational method proposed by Hammer and Ivanova [174]. The only assumption of the process is that there is a little coupling between different supported slab modes (i.e. the profile of the waveguide does not substantially change in the 3rd dimension). In SOI materials with only two different modes with TE and TM polarisation supported by a single mode waveguide, this is an excellent assumption.

With this method, long simulation areas can be simulated in a short timescale with high accuracy as described in the white-paper published by Lumerical [175].

VarFDTD was available for this work through the commercial software "Lumerical Mode solutions" [112] and has been used for simulating the ring resonators and to estimate the optimal design for the waveguide couplers.

Eigenmode Expansion (EME) is a bidirectional fully vectorial frequency domain method for solving Maxwell's equation. The method is based on a base set of eigenmodes from the modal decomposition of electromagnetic fields. The geometry is divided into multiple cells, and these modes are calculated at the

interface between the adjacent cells. By matching the tangential H and E fields at the boundaries, scattering matrices for each section can be formulated. Finally, the S matrix for the entire device can be calculated, and the internal field can be reconstructed [176].

After the initial calculations, the distance between each section can arbitrarily change without having to repeat the precedent simulations. These offer a significant advantage over FDTD as the simulation requirements scale well with distance contrary to FDTD, which is very demanding in computational memory and time requirements. Compared to the BPM; EME is a bidirectional method which does not make the approximation of slowly varying envelope. As a consequence, EME accuracy is not compromised in simulations with light propagating at large angles and for materials with high refractive index differences. As such, it is ideal for simulations of silicon photonic devices.

The classical EME method uses a staircase approximation to resolve material or geometrical variation in the direction of propagation for continuously varying structures. This leads potentially to calculation inaccuracies and non-physical reflections. The typical solution to address this issue is to increase the number of cells but, as a result, the simulation requirements increase. A better solution is to use a Continuously Varying Cross-sectional Subcell (CVCS) method which avoids the staircasing effect.

EME method, available through the commercial software "Lumerical Mode solutions" [112], was extensively used for the design of the polymer couplers, Bragg gratings and inverse tapers.

Finite Element Method (FEM) is used to compute approximations (numerical model equations) of the real solution to the partial differential equations. FEM benefits from a great freedom in the selection of the discretisation of both the basic functions and the elements used to discretise the space [177].

By dividing the simulation area into discrete units cells, it is possible to find the exact solution for each unit cell and translate it to an approximate solution of the general differential equation. The size and the shape of the unit cells vary depending on the shape of the simulated structure.

FEM, available through the commercial software "Comsol" [166], was used for optimising the heating elements for the waveguide tuning.

B.2 Boundary conditions

An essential parameter for each simulation independent on the solver used is the choice of the boundary condition applied to the model. Depending on the boundary conditions, the accuracy of the results as well as the simulation requirements in terms of time and memory can be substantially affected. In this section, the boundary conditions available on the Lumerical products will be briefly explained.

Perfectly matched layer (PML) Boundaries are designed in such a way that an incident wave from a non-PML to a PML medium is not reflected by the interface. As a result, PMLs are used to strongly absorb any incident wave [178].

Metal Some boundaries behave as Perfect Electric Conductor (PCE), in which the component of the E field parallel to the boundary, and the H field perpendicular to the boundary is zero. These boundaries do not allow any energy to escape the simulation volume being perfect reflecting.

Periodic This boundary is used when both the electromagnetic field and the structure are periodic, and it can be used in one or more directions.

Bloch This boundary can be used when both the structure and the electromagnetic fields are periodic, but a phase shift exists between each period. It can be used when plane waves are launched at an angle with respect to a periodic structure or for calculating the band structure of a periodic object (such as a Bragg grating).

Perfect Magnetic Conductor (PMC) This boundary is the magnetic equivalent of the PCE. In this case, the E field perpendicular to the boundary and the H field parallel to the boundary are zero.

Symmetric / Anti-Symmetric These boundaries are used when the system exhibits at least one plane of symmetry. Symmetric boundaries are mirrors for the E field, anti mirrors for the H field. The anti-symmetric boundaries are the opposite with mirrors for the H fields and anti mirrors for the E fields. For a correct result, the source should have the same symmetry than that of the boundaries. Great care has to be taken when these boundaries are used, and more details can be found on the Lumerical website [179].

Appendix C

Silicon Waveguides for Second Harmonic Generation

C.1 Introduction

Even though silicon is a well-established material for photonic integrated circuits, it lacks key functionalities such as light emission and fast modulation capabilities [185]. This is a direct consequence of the indirect silicon bandgap and centrosymmetry of its crystal lattice [186]. The latter is of particular relevance for optical modulators due to the absence of the second-order nonlinear susceptibility ($\chi^{(2)}$), which prevents the development of electro-optic modulators. Current phase modulators in silicon are either built on the thermo-optic effect with the use of metal heaters [96] (see Chapter 3) or make use of the refractive index change induced by the plasma effect in forward biased pin junctions. The first approach is technically simpler but only offers slow modulation (of the orders of a few μs [187]); the second is substantially faster (below the ns) but adds losses to the waveguide and complexity in the fabrication process. Both approaches are power hungry and therefore cannot be scaled up to circuits containing hundreds of devices.

Recently, Jacobsen et. al. have proposed the use of strained claddings such as silicon nitride to break the symmetry of the silicon crystal lattice [188] and induce a sizable $\chi^{(2)}$ in the material. The first attempt led to $\chi^{(2)}$ values of 15pmV^{-1} [188]. As a comparison the lithium niobate (LiNbO_3), which is a widely used material for the fabrication of electro-optic modulators, has a $\chi^{(2)} = 36\text{pmV}^{-1}$ [189]. Over

the years higher values of $\chi^{(2)} = 122\text{pmV}^{-1}$ [189] have been reported by Chmielak et. al and $\chi^{(2)} = 190\text{pmV}^{-1}$ [190] at a later time. The highest value of 336pmV^{-1} [191] was reported by Pedro Damas et. al in a Mach-Zehnder geometry with a push-pull electrode configuration. Although the reported values are comparable with the best electro-optic materials, the need for high electrical potential (30 V) remains a limiting factor, which requires further development.

Also, in some of the reported experiments, non-convincing evidence was given for the origin of this $\chi^{(2)}$. It has been long suspected that any second-order non-linearity measured in silicon is due to the weak $\chi^{(2)}$ on the surface of the waveguides and not to the stress. The additional contribution to the $\chi^{(2)}$ might originate from carrier accumulation at the interfaces between silicon and silicon nitride.

In this Appendix, a theoretical discussion for non-linear optics will be made followed by the designs of the two different waveguides presented in Section 3.3.

C.2 Non-Linear Optics

The interaction of electron and phonons with the optical field leads to a plethora of non-linearities in silicon [192–194]. Polarisation is caused by the resonance of the optical field with the electrons in the outer shell of the silicon atoms. An electron's orbital gets displaced from the nucleus by an oscillating photon at a frequency ω . By assuming a dielectric response in an isotropic material, the relation between the electric field ($E(t)$) and the induced polarisation ($P(t)$) is expressed:

$$P(t) = \epsilon_0(\chi^{(1)}E(t) + \chi^{(2)}E^2(t) + \chi^{(3)}E^3(t) + \dots) \quad (\text{C.1})$$

where $\chi^{(i)}$ is the i^{th} order optical susceptibilities and ϵ_0 is the vacuum permittivity. The susceptibilities terms are tensors. The consequence of this is that waves at new frequencies are generated. In this work we are only interested in the second-harmonic generation, a phenomenon induced by the second order non-linear susceptibility ($\chi^{(2)}$).

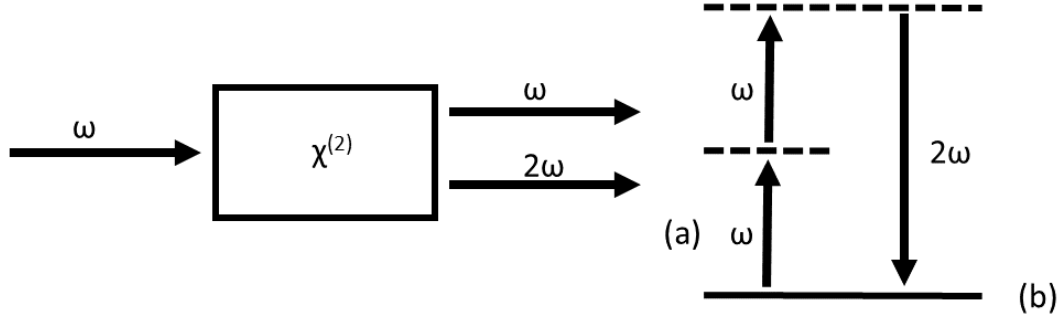


FIGURE C.1: (a) Schematic of a second-harmonic generation experiment. (b) Energy-level diagram for second-harmonic generation.

C.2.1 Second-Harmonic Generation

Figure C.1 shows the process of second-harmonic generation, where two photons with frequency ω are destroyed to create a photon with frequency 2ω as shown in Figure C.1b.

When a laser beam with electric field strength:

$$\tilde{E}(t) = E \exp(-i\omega t) + c.c. \quad (\text{C.2})$$

is incident onto a crystal with nonzero $\chi^{(2)}$, the non-linear polarisation created in the crystal is given by:

$$\tilde{P}^{(2)} = \chi^{(2)} \tilde{E}^2(t) = 2\chi^{(2)} E E^* + (\chi^{(2)} E^2 \exp(-2\omega t) + c.c.) \quad (\text{C.3})$$

The first term of the second order polarisation consists of a contribution at zero frequency. This term does not contribute to the generation of electromagnetic radiation due to the vanishing of its second derivative, rather it leads to optical rectification, which is a process where static electric field is created inside the non-linear crystal. The second term of the second order polarisation contribute at frequency 2ω . Following the equation:

$$\nabla^2 \tilde{E} - \frac{n^2}{c^2} \frac{\partial^2 \tilde{E}}{\partial t^2} = \frac{4\pi}{c^2} \frac{\partial^2 \tilde{P}^{NL}}{\partial t^2} \quad (\text{C.4})$$

The later contribution can lead to the generation of radiation at the second-harmonic frequency, where n is the linear refractive index, c is the speed of light in vacuum and \tilde{P}^{NL} is the non-linear polarisation.

Under the proper experimental condition, nearly all the power of the incident radiation with frequency ω is converted to radiation with frequency 2ω . The most common application is the conversion of a laser frequency to a different spectral region. In our case, our goal is to convert a $3 \mu\text{m}$ laser to the telecommunication wavelength of $1.5 \mu\text{m}$.

C.2.2 Straight waveguides

The first design was to optimise a standard straight waveguide for SHG.

For the second harmonic generation to take place, the width of the waveguide has to be engineered in order to have a phase matching between the two modes. To identify the phase matching condition, the effective index of the waveguide with widths between 500 nm and $2 \mu\text{m}$ was calculated as shown in Figure C.2.

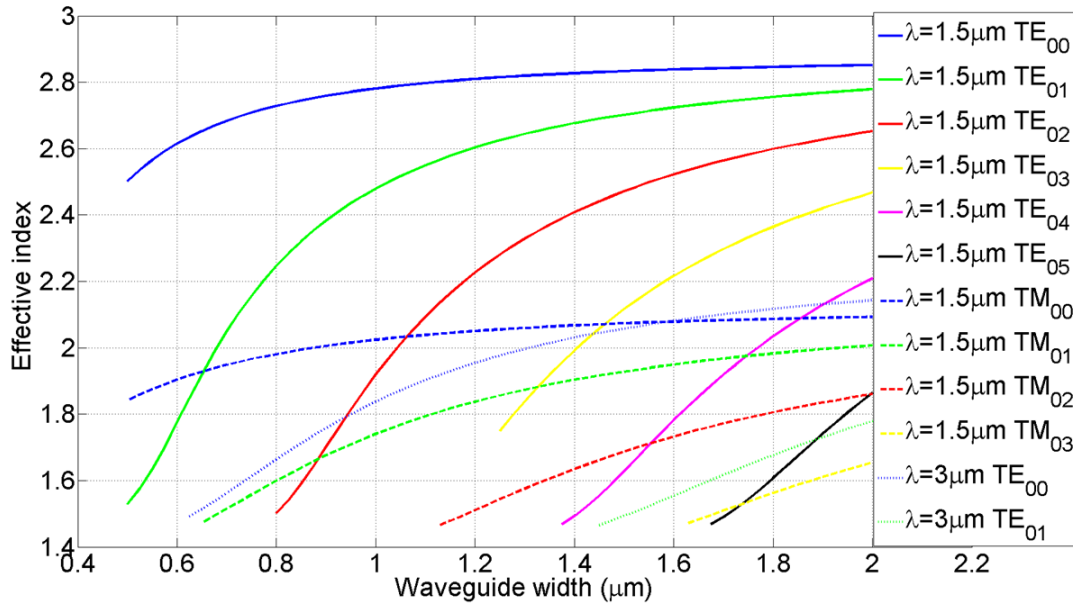


FIGURE C.2: The effective index against the width of the waveguide, for wavelengths of $\lambda=1.5 \mu\text{m}$ and $\lambda=3 \mu\text{m}$.

Four widths where phase matching occurs were found for a straight waveguide between the wavelength of $\lambda=1.5 \mu\text{m}$ and the fundamental TE mode at $\lambda=3 \mu\text{m}$ (Figure C.2). Three of them are between the fundamental TE mode at $3 \mu\text{m}$ and

higher order modes of the TE polarisation at $1.5 \mu\text{m}$ (TE_{02} , TE_{03} and TE_{04}). The fourth phase matching width is between the TE fundamental mode at $3 \mu\text{m}$ and the TM fundamental mode at $1.5 \mu\text{m}$.

Even though the geometry is well studied at a wavelength $\lambda = 1.5 \mu\text{m}$, and the losses have been quantified in several works [68], less data are available on the losses at a wavelength of $3 \mu\text{m}$ for a silicon waveguide with a height of 220 nm . To evaluate the losses at a wavelength of $3 \mu\text{m}$, simulations were performed to extract the losses against the width of the waveguide. As it can be seen in Figure C.3, the theoretical losses for any waveguide smaller than $1 \mu\text{m}$ are too high for any real propagation to take place.

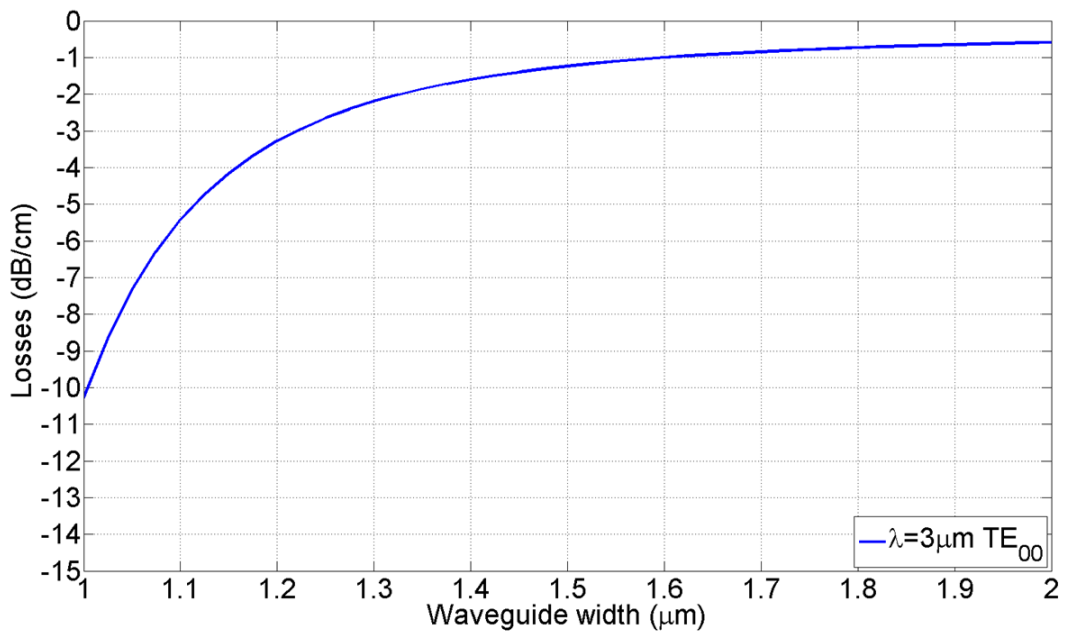


FIGURE C.3: The losses at a $3 \mu\text{m}$ wavelength against the width of the waveguide.

Bibliography

- [1] David A. B. Miller. Device Requirement for Optical Interconnects to Silicon Chips. *Proc. of IEEE Special Issue on Silicon Photonics*, 97(7):1166–1185, 2009. ISSN 0018-9219. doi: 10.1109/JPROC.2009.2014298.
- [2] Breck Hitz. Intel turns to photonics to extend moore’s law. *Physics World*, 22(07):12, 2009.
- [3] ePIXfab. URL <http://epixfab.eu/>.
- [4] David Thomson, Aaron Zilkie, John E Bowers, Tin Komljenovic, Graham T Reed, Laurent Vivien, Delphine Marris-Morini, Eric Cassan, Lopold Virot, Jean-Marc Fdli, Jean-Michel Hartmann, Jens H Schmid, Dan-Xia Xu, Frdric Boeuf, Peter OBrien, Goran Z Mashanovich, and M Nedeljkovic. Roadmap on silicon photonics. *Journal of Optics*, 18(7), 2016.
- [5] R. Soref. The past, present, and future of silicon photonics. *IEEE Journal of Selected Topics in Quantum Electronics*, 12(6):1678–1687, Nov 2006. ISSN 1077-260X. doi: 10.1109/JSTQE.2006.883151.
- [6] Michel Bruel, Bernard Aspar, and Andre-Jacques Auberton-Herv. Smart-cut: A new silicon on insulator material technology based on hydrogen implantation and wafer bonding. *Japanese Journal of Applied Physics*, 36(3S): 1636, 1997.
- [7] L Pavesi. Will silicon be the photonic material of the third millenium? *Journal of Physics: Condensed Matter*, 15(26):R1169, 2003.
- [8] B. Jalali and S. Fathpour. Silicon photonics. *Journal of Lightwave Technology*, 24(12):4600–4615, 2006. doi: 10.1109/JLT.2006.885782.
- [9] Graham T. Reed. Device physics: The optical age of silicon. *Nature*, 427 (6975):595–596, 2004. ISSN 0028-0836. doi: 10.1038/427595b.

- [10] Michal Lipson. Guiding, modulating, and emitting light on silicon—challenges and opportunities. *J. Lightwave Technol.*, 23(12):4222, Dec 2005.
- [11] Di Liang, Gunther Roelkens, Roel Baets, and John E. Bowers. Hybrid integrated platforms for silicon photonics. *Materials*, 3(3):1782–1802, 2010. ISSN 1996-1944. doi: 10.3390/ma3031782.
- [12] G. Roelkens, L. Liu, D. Liang, R. Jones, A. Fang, B. Koch, and J. Bowers. Iii-v/silicon photonics for on-chip and intra-chip optical interconnects. *Laser and Photonics Reviews*, 4(6):751–779, 2010. ISSN 1863-8899. doi: 10.1002/lpor.200900033.
- [13] Richard J. Bojko, Jing Li, Li He, Tom Baehr-Jones, Michael Hochberg, and Yukinori Aida. Electron beam lithography writing strategies for low loss, high confinement silicon optical waveguides. *Journal of Vacuum Science and Technology B, Nanotechnology and Microelectronics: Materials, Processing, Measurement, and Phenomena*, 29(6):06F309, 2011. doi: 10.1116/1.3653266.
- [14] M. Gnan, S. Thoms, D. S. Macintyre, R. m. D. La Rue, and M. Sorel. Fabrication of low-loss photonic wires in silicon-on-insulator using hydrogen silsesquioxane electron-beam resist. *Electronics Letters*, 44(2):115–116, January 2008. ISSN 0013-5194. doi: 10.1049/el:20082985.
- [15] Jaime Cardenas, Carl B. Poitras, Jacob T. Robinson, Kyle Preston, Long Chen, and Michal Lipson. Low loss etchless silicon photonic waveguides. *Opt. Express*, 17(6):4752–4757, Mar 2009. doi: 10.1364/OE.17.004752.
- [16] Po Dong, Wei Qian, Hong Liang, Roshanak Shafiiha, Ning-Ning Feng, Dazeng Feng, Xuezhe Zheng, Ashok V Krishnamoorthy, and Mehdi Asghari. Low power and compact reconfigurable multiplexing devices based on silicon microring resonators. *Opt. Express*, 18(10):9852–9858, 2010.
- [17] Vilson R. Almeida, Roberto R. Panepucci, and Michal Lipson. Nanotaper for compact mode conversion. *Opt. Lett.*, 28(15):1302–1304, Aug 2003. doi: 10.1364/OL.28.001302.
- [18] F. Van Laere, T. Claes, J. Schrauwen, S. Scheerlinck, W. Bogaerts, D. Tailaert, L. O’Faolain, D. Van Thourhout, and R. Baets. Compact focusing grating couplers for silicon-on-insulator integrated circuits. *IEEE Photonics Technology Letters*, 19(23):1919–1921, Dec 2007. ISSN 1041-1135. doi: 10.1109/LPT.2007.908762.

- [19] Yurii a. Vlasov and Sharee J. McNab. Losses in single-mode silicon-on-insulator strip waveguides and bends. *Optics Express*, 12(8):1622, 2004. ISSN 1094-4087. doi: 10.1364/OPEX.12.001622.
- [20] R. A. Soref, J. Schmidtchen, and K. Petermann. Large single-mode rib waveguides in gesi-si and si-on-sio₂. *IEEE Journal of Quantum Electronics*, 27(8):1971–1974, Aug 1991. ISSN 0018-9197. doi: 10.1109/3.83406.
- [21] Daoxin Dai and Sailing He. Analysis of characteristics of bent rib waveguides. *J. Opt. Soc. Am. A*, 21(1):113–121, Jan 2004. doi: 10.1364/JOSAA.21.000113.
- [22] L Vivien, S Laval, B Dumont, S Lardenois, A Koster, and E Cassan. Polarization-independent single-mode rib waveguides on silicon-on-insulator for telecommunication wavelengths. *Optics Communications*, 210(1):43 – 49, 2002. ISSN 0030-4018. doi: [https://doi.org/10.1016/S0030-4018\(02\)01681-4](https://doi.org/10.1016/S0030-4018(02)01681-4).
- [23] Daoxin Dai and Sailing He. Analysis of the birefringence of a silicon-on-insulator rib waveguide. 43(5):1156–1161, Feb 2004. doi: 10.1364/AO.43.001156.
- [24] Seong Phun Chan, Ching Eng Png, Soon Thor Lim, Graham T. Reed, and Vittorio M. N. Passaro. Single-mode and polarization-independent silicon-on-insulator waveguides with small cross section. *J. Lightwave Technol.*, 23(6):2103, Jun 2005.
- [25] G Z Mashanovich, M Milosevic, P Matavulj, S Stankovic, B Timotijevic, P Y Yang, E J Teo, M B H Breese, A A Bettiol, and G T Reed. Silicon photonic waveguides for different wavelength regions. *Semiconductor Science and Technology*, 23(6):064002, 2008.
- [26] M. M. Milosevic, P. S. Matavulj, B. D. Timotijevic, G. T. Reed, and G. Z. Mashanovich. Design rules for single-mode and polarization-independent silicon-on-insulator rib waveguides using stress engineering. *Journal of Lightwave Technology*, 26(13):1840–1846, July 2008. ISSN 0733-8724. doi: 10.1109/JLT.2008.922193.
- [27] D.-X. Xu, P. Cheben, D. Dalacu, A. Del age, S. Janz, B. Lamontagne, M.-J. Picard, and W. N. Ye. Eliminating the birefringence in silicon-on-insulator

- ridge waveguides by use of cladding stress. *Opt. Lett.*, 29(20):2384–2386, Oct 2004. doi: 10.1364/OL.29.002384.
- [28] W. N. Ye, D. X. Xu, S. Janz, P. Cheben, M. J. Picard, B. Lamontagne, and N. G. Tarr. Birefringence control using stress engineering in silicon-on-insulator (soi) waveguides. *Journal of Lightwave Technology*, 23(3):1308–1318, March 2005. ISSN 0733-8724. doi: 10.1109/JLT.2005.843518.
- [29] A. G. Rickman and G. T. Reed. Silicon-on-insulator optical rib waveguides: loss, mode characteristics, bends and y-junctions. *IEE Proceedings - Optoelectronics*, 141(6):391–393, Dec 1994. ISSN 1350-2433. doi: 10.1049/ip-opt:19941468.
- [30] Isa Kiyat, Atilla Aydinli, and Nadir Dagli. High-q silicon-on-insulator optical rib waveguide racetrack resonators. *Opt. Express*, 13(6):1900–1905, Mar 2005. doi: 10.1364/OPEX.13.001900.
- [31] I. Kiyat, A. Aydinli, and N. Dagli. Polarization characteristics of compact soi rib waveguide racetrack resonators. *IEEE Photonics Technology Letters*, 17(10):2098–2100, Oct 2005. ISSN 1041-1135. doi: 10.1109/LPT.2005.856410.
- [32] D. X. Xu, S. Janz, and P. Cheben. Design of polarization-insensitive ring resonators in silicon-on-insulator using mmi couplers and cladding stress engineering. *IEEE Photonics Technology Letters*, 18(2):343–345, Jan 2006. ISSN 1041-1135. doi: 10.1109/LPT.2005.861973.
- [33] Andre Delage Jeffrey W. Fraser Siegfried Janz Paul E. Jessop Dan-Xia Xu Matthew R.T. Pearson, Andrew Bezinger. Arrayed waveguide grating demultiplexers in silicon-on-insulator, 2000.
- [34] P. D. Trinh, S. Yegnanarayanan, F. Coppinger, and B. Jalali. Silicon-on-insulator (soi) phased-array wavelength multi/demultiplexer with extremely low-polarization sensitivity. *IEEE Photonics Technology Letters*, 9(7):940–942, July 1997. ISSN 1041-1135. doi: 10.1109/68.593358.
- [35] Z. Sheng, D. Dai, and S. He. Comparative study of losses in ultrasharp silicon-on-insulator nanowire bends. *IEEE Journal of Selected Topics in Quantum Electronics*, 15(5):1406–1412, Sept 2009. ISSN 1077-260X. doi: 10.1109/JSTQE.2009.2013360.

- [36] Hiroshi Fukuda, Koji Yamada, Tai Tsuchizawa, Toshifumi Watanabe, Hiroyuki Shinojima, and Sei ichi Itabashi. Silicon photonic circuit with polarization diversity. *Opt. Express*, 16(7):4872–4880, Mar 2008. doi: 10.1364/OE.16.004872.
- [37] D. Dai, L. Liu, L. Wosinski, and S. He. Design and fabrication of ultra-small overlapped awg demultiplexer based on alpha;-si nanowire waveguides. *Electronics Letters*, 42(7):400–402, March 2006. ISSN 0013-5194. doi: 10.1049/el:20060157.
- [38] W. Bogaerts, S. K. Selvaraja, P. Dumon, J. Brouckaert, K. De Vos, D. Van Thourhout, and R. Baets. Silicon-on-insulator spectral filters fabricated with cmos technology. *IEEE Journal of Selected Topics in Quantum Electronics*, 16(1):33–44, Jan 2010. ISSN 1077-260X. doi: 10.1109/JSTQE.2009.2039680.
- [39] Yaocheng Shi, Srinivasan Anand, and Sailing He. Design of a polarization insensitive triplexer using directional couplers based on submicron silicon rib waveguides. *J. Lightwave Technol.*, 27(11):1443–1447, Jun 2009.
- [40] Daoxin Dai and Sailing He. Design of a polarization-insensitive arrayed waveguide grating demultiplexer based on silicon photonic wires. *Opt. Lett.*, 31(13):1988–1990, Jul 2006. doi: 10.1364/OL.31.001988.
- [41] Shen Ao, Qiu Chen, Hu Ting, Xu Chao, Jiang Xiao-Qing, Li Yu-Bo, and Yang Jian-Yi. An eight-channel 400 ghz-spacing etched diffraction grating multi/demultiplexer on a nanophotonic silicon-on-insulator platform. *Chinese Physics Letters*, 30(8):084204, 2013.
- [42] Francesco Morichetti, Antonio Canciamilla, Carlo Ferrari, Matteo Torregiani, Andrea Melloni, and Mario Martinelli. Roughness induced backscattering in optical silicon waveguides. *Physical Review Letters*, 104(3):1–4, 2010. ISSN 00319007. doi: 10.1103/PhysRevLett.104.033902.
- [43] Z. Tu, Y. W. Huang, H. X. Yi, X. J. Wang, Y. P. Li, L. Li, and W. W. Hu. A compact soi polarization beam splitter based on multimode interference coupler. In *2011 Asia Communications and Photonics Conference and Exhibition (ACP)*, pages 1–6, Nov 2011. doi: 10.1117/12.905589.

- [44] Aleksandr Biberman, Benjamin G. Lee, Amy C. Turner-Foster, Mark A. Foster, Michal Lipson, Alexander L. Gaeta, and Keren Bergman. Wavelength multicasting in silicon photonic nanowires. *Opt. Express*, 18(17):18047–18055, Aug 2010. doi: 10.1364/OE.18.018047.
- [45] Yanqiao Xie, Ying Gao, Shiming Gao, Xudong Mou, and Sailing He. All-optical multiple-channel logic xor gate for nrz-dpsk signals based on nondegenerate four-wave mixing in a silicon waveguide. *Opt. Lett.*, 36(21):4260–4262, Nov 2011. doi: 10.1364/OL.36.004260.
- [46] Shiming Gao, Zhiqiang Li, En-Kuang Tien, Sailing He, and Ozdal Boyraz. Performance evaluation of nondegenerate wavelength conversion in a silicon nanowire waveguide. *J. Lightwave Technol.*, 28(21):3079–3085, Nov 2010.
- [47] S. Gao, X. Zhang, Z. Li, and S. He. Polarization-independent wavelength conversion using an angled-polarization pump in a silicon nanowire waveguide. *IEEE Journal of Selected Topics in Quantum Electronics*, 16(1):250–256, Jan 2010. ISSN 1077-260X. doi: 10.1109/JSTQE.2009.2034755.
- [48] Soitec. URL <https://www.soitec.com/en>.
- [49] Xi-Qiao Feng and Y. Huang. Mechanics of smart-cut technology. *International Journal of Solids and Structures*, 41(16-17):4299–4320, 2004.
- [50] W. R. Thurber. Resistivity-Dopant Density Relationship for Phosphorus-Doped Silicon. *Journal of The Electrochemical Society*, 127(8):1807, 1980. ISSN 00134651. doi: 10.1149/1.2129394.
- [51] Zheng Cui. *Nanofabrication: Principles, capabilities and limits*. 2009. ISBN 9780387755762. doi: 10.1007/978-0-387-75577-9.
- [52] Mentor. URL <https://www.mentor.com/tannereda/1-edit>.
- [53] James Watt Nanofabrication Centre. URL <http://www.jwnc.gla.ac.uk/>.
- [54] R. M. De La Rue M. GnanD. S. Macintyre, M. Sorel and S. Thoms. Enhanced stitching for the fabrication of photonic structures by electron beam lithography. *J. Vac. Sci. Technol. B*, 25(6):2034, 2007. ISSN 10711023. doi: 10.1116/1.2800325.
- [55] a. Samarelli, D. S. Macintyre, M. J. Strain, R. M. De La Rue, M. Sorel, and S. Thoms. Optical characterization of a hydrogen silsesquioxane lithography

- process. *Journal of Vacuum Science & Technology B: Microelectronics and Nanometer Structures*, 26(6):2290, 2008. ISSN 10711023. doi: 10.1116/1.2998694.
- [56] Product Information. Electronics Dow Corning FOx-1x and FOx-2x Flowable Oxides. pages 1–3.
- [57] Chang-Chung Yang and Wen-Chang Chen. The structures and properties of hydrogen silsesquioxane (HSQ) films produced by thermal curing. *Journal of Materials Chemistry*, 12(4):1138–1141, 2002. ISSN 09599428. doi: 10.1039/b107697n.
- [58] Y. K. Siew, G. Sarkar, X. Hu, J. Hui, a. See, and C. T. Chua. Thermal Curing of Hydrogen Silsesquioxane. *Journal of The Electrochemical Society*, 147(1):335, 2000. ISSN 00134651. doi: 10.1149/1.1393196.
- [59] Dong Hyun Kim, Se Koo Kang, Geun Young Yeom, and Jae Hyung Jang. Nanometer-scale fabrication of hydrogen silsesquioxane (HSQ) films with post exposure baking. 13(3):1918–1922, 2013. ISSN 15334880. doi: 10.1166/jnn.2013.6986.
- [60] ZEP520 Series EB Resists. URL <http://www.zeonchemicals.com/ElectronicMaterials/>.
- [61] MicroChem NANO PMMA and Copolymer. URL http://microchem.com/pdf/PMMA_Data_Sheet.pdf.
- [62] MicroChem SU8 3000. URL <http://www.microchem.com/pdf/SU-8%203000%20Data%20Sheet.pdf>.
- [63] SPTS, . URL <http://www.spts.com/>.
- [64] Oxford Instruments. URL <https://www.oxford-instruments.com/>.
- [65] Sergi Gomez, Rodolfo Jun Belen, Mark Kiehlbauch, and Eray S. Aydil. Etching of high aspect ratio structures in Si using SF₆/O₂ plasma. *Journal of Vacuum Science & Technology A: Vacuum, Surfaces, and Films*, 22(2004):606, 2004. ISSN 07342101. doi: 10.1116/1.1710493.
- [66] H V Jansen, M J de Boer, K Ma, M Girones, S Unnikrishnan, M C Louwerse, and M C Elwenspoek. Black silicon method XI: oxygen pulses in SF₆ plasma.

- Journal of Micromechanics and Microengineering*, 20(7):75027, 2010. ISSN 0960-1317. doi: 10.1088/0960-1317/20/7/075027.
- [67] R. F. Figueroa, S. Spiesshoefer, S. L. Burkett, and L. Schaper. Control of sidewall slope in silicon vias using SF₆O₂ plasma etching in a conventional reactive ion etching tool. *Journal of Vacuum Science & Technology B: Microelectronics and Nanometer Structures*, 23(5):2226, 2005. ISSN 0734211X. doi: 10.1116/1.2041654.
- [68] Jun Young Lee and Sun Nam Hwang. A high-gain boost converter using voltage-stacking cell. *Transactions of the Korean Institute of Electrical Engineers*, 57(6):982–984, 2008. ISSN 19758359. doi: 10.1049/el.
- [69] Zihao Ouyang, D. N. Ruzic, Mark Kiehlbauch, Alex Schrimsky, and Kevin Torek. Etching mechanism of the single-step through-silicon-via dry etch using SF₆/C₄F₈ chemistry. *Journal of Vacuum Science & Technology A: Vacuum, Surfaces, and Films*, 32:041306, 2014. ISSN 0734-2101. doi: 10.1116/1.4885500.
- [70] Henri Jansen, Meint de Boer, Remco Wiegerink, Niels Tas, Edwin Smulders, Christina Neagu, and Miko Elwenspoek. Rie lag in high aspect ratio trench etching of silicon. *Microelectronic Engineerin*, 35(1):45 – 50, 1997. ISSN 0167-9317. doi: [https://doi.org/10.1016/S0167-9317\(96\)00142-6](https://doi.org/10.1016/S0167-9317(96)00142-6). Micro- and Nano- Engineering 96.
- [71] Plasma Enhanced Chemical Vapour Deposition (PECVD) Oxford instruments, . URL <https://www.oxford-instruments.com/products/etching-deposition-and-growth/plasma-etch-deposition/pecvd>.
- [72] Inductively Coupled Plasma Chemical Vapour Deposition (ICP-CVD) Oxford instruments, . URL <https://www.oxford-instruments.com/products/etching-deposition-and-growth/plasma-etch-deposition/icp-cvd>.
- [73] A. Khanna, A. Z. Subramanian, M. Häyrynen, S. Selvaraja, P. Verheyen, D. Van Thourhout, S. Honkanen, H. Lipsanen, and R. Baets. Impact of ALD grown passivation layers on silicon nitride based integrated optic devices for very-near-infrared wavelengths. *Optics Express*, 22(5):5684, 2014. ISSN 1094-4087. doi: 10.1364/OE.22.005684.

- [74] LPCVD / Diffusion SPTS, . URL <http://www.spts.com/products/lpcvd-diffusion>.
- [75] Payam Alipour, Ali Asghar Eftekhari, Amir Hossein Atabaki, Qing Li, Siva Yegnanarayanan, Christi K. Madsen, and Ali Adibi. Fully reconfigurable compact rf photonic filters using high-q silicon microdisk resonators. *Opt. Express*, 19(17):15899–15907, Aug 2011.
- [76] A. Melloni, A. Canciamilla, C. Ferrari, F. Morichetti, L. O’Faolain, T. F. Krauss, R. De La Rue, A. Samarelli, and M. Sorel. Tunable delay lines in silicon photonics: Coupled resonators and photonic crystals, a comparison. *IEEE Photonics Journal*, 2(2):181–194, April 2010.
- [77] William M. J. Green, Michael J. Rooks, Lidija Sekaric, and Yurii A. Vlasov. Ultra-compact, low rf power, 10 gb/s silicon mach-zehnder modulator. *Opt. Express*, 15(25):17106–17113, Dec 2007.
- [78] Min Yang, William M. J. Green, Solomon Assefa, Joris Van Campenhout, Benjamin G. Lee, Christopher V. Jahnes, Fuad E. Doany, Clint L. Schow, Jeffrey A. Kash, and Yurii A. Vlasov. Non-blocking 4x4 electro-optic silicon switch for on-chip photonic networks. *Opt. Express*, 19(1):47–54, Jan 2011.
- [79] M R Watts, J Sun, C DeRose, D C Trotter, R W Young, and G N Nielson. Adiabatic thermo-optic Mach-Zehnder switch. *Optics Letters*, 38(5):733–735, 2013.
- [80] Tymon Barwicz, Miloš A. Popovic, Fuwan Gan, Marcus S. Dahlem, Charles W. Holzwarth, Peter T. Rakich, Erich P. Ippen, Franz X. Kartner, Henry I. Smith, Miloš a. Popović, and Franz X. Kärtner. Reconfigurable silicon photonic circuits for telecommunication applications. *Proceedings of SPIE*, 6872:68720Z–68720Z–12, 2008.
- [81] Amir H. Atabaki, Ali a. Eftekhari, Siva Yegnanarayanan, and Ali Adibi. Sub-microsecond thermal reconfiguration of silicon photonic devices. *Conference Proceedings - Lasers and Electro-Optics Society Annual Meeting-LEOS*, 21(13):495–496, 2009.
- [82] Daoxin Dai, Liu Yang, and Sailing He. Ultrasmall thermally tunable microring resonator with a submicrometer heater on Si nanowires. *Journal of Lightwave Technology*, 26(6):704–709, 2008.

- [83] A H Atabaki, E Shah Hosseini, A A Eftekhari, S Yegnanarayanan, and A Adibi. Optimization of metallic microheaters for high-speed reconfigurable silicon photonics. *Optics express*, 18(17):18312–18323, 2010.
- [84] Ciyuan Qiu, Jie Shu, Zheng Li, Xuezhi Zhang, and Qianfan Xu. Wavelength tracking with thermally controlled silicon resonators. *Optics express*, 19(6):5143–5148, 2011.
- [85] Junfeng Song, H Zhao, Q Fang, S H Tao, T Y Liow, M B Yu, G Q Lo, and D L Kwong. Effective thermo-optical enhanced cross-ring resonator MZI interleavers on SOI. *Optics express*, 16(26):21476–21482, 2008.
- [86] Nicholas C. Harris, Yangjin Ma, Jacob Mower, Tom Baehr-Jones, Dirk Englund, Michael Hochberg, and Christophe Galland. Efficient, compact and low loss thermo-optic phase shifter in silicon. *Optics Express*, 22(9):10487, 2014.
- [87] Qing Fang, Junfeng Song, Xianshu Luo, Lianxi Jia, Mingbin Yu, Guoqiang Lo, and Yuliang Liu. High efficiency ring-resonator filter with NiSi heater. *IEEE Photonics Technology Letters*, 24(5):350–352, 2012.
- [88] John E Cunningham, Ivan Shubin, Xuezhe Zheng, Thierry Pinguet, Attila Mekis, Ying Luo, Hiren Thacker, Guoliang Li, Jin Yao, Kannan Raj, and Ashok V Krishnamoorthy. Highly-efficient thermally-tuned resonant optical filters. *Optics express*, 18(18):19055–19063, 2010.
- [89] Adam Densmore, Siegfried Janz, Rubin Ma, Jens H. Schmid, Dan-Xia Xu, André Delâge, Jean Lapointe, Martin Vachon, and Pavel Cheben. Compact and low power thermo-optic switch using folded silicon waveguides. *Optics Express*, 17(13):10457, 2009.
- [90] Salah Ibrahim, Nicolas K Fontaine, Stevan S Djordjevic, Binbin Guan, Tiehui Su, Stanley Cheung, Ryan P Scott, Andrew T Pomerene, Liberty L Seaford, Craig M Hill, Steve Danziger, Zhi Ding, K Okamoto, and S J B Yoo. Demonstration of a fast-reconfigurable silicon CMOS optical lattice filter. *Optics express*, 19(14):13245–56, 2011.
- [91] Viktoriia E. Babicheva, Nathaniel Kinsey, Gururaj V. Naik, Marcello Ferrera, Andrei V. Lavrinenko, Vladimir M. Shalaev, and Alexandra Boltasseva. Towards CMOS-compatible nanophotonics: Ultra-compact modulators using alternative plasmonic materials. *Optics Express*, 21(22):27326, 2013.

- [92] A Masood, M Pantouvaki, D Goossens, G Lepage, P Verheyen, and P Absil. CMOS-compatible Tungsten Heaters for Silicon Photonic Waveguides. *Proceedings of the IEEE*, 3(Figure 2):234–236, 2012.
- [93] G. T. Reed, G. Mashanovich, F. Y. Gardes, and D. J. Thomson. Silicon optical modulators. *Nature Photonics*, 4:518 – 526, 2010. ISSN 0167-9317. doi: 10.1038/nphoton.2010.179.
- [94] G. Ghosh. *Handbook of Thermo-optic Coefficients of Optical Materials with Applications*. Number v. 4 in Handbook of Optical Constants of Solids Series. Academic Press, 1998.
- [95] A. Bejan and A.D. Kraus. *Heat Transfer Handbook*. Number v. 1 in Heat Transfer Handbook. Wiley, 2003.
- [96] Piero Orlandi, Francesco Morichetti, Michael John Strain, Marc Sorel, Andrea Melloni, and Paolo Bassi. Tunable silicon photonics directional coupler driven by a transverse temperature gradient. *Optics letters*, 38(6):863–5, 2013.
- [97] Ning Zhang, Kenan Cicek, Jiangbo Zhu, Shimao Li, Huanlu Li, Marc Sorel, Xinlun Cai, and Siyuan Yu. Manipulating optical vortices using integrated photonics. *Frontiers of Optoelectronics*, 9(2):194–205, 2016.
- [98] Dirk Taillaert, Peter Bienstman, and Roel Baets. Compact efficient broadband grating coupler for silicon-on-insulator waveguides. *Optics letters*, 29(23):2749–2751, 2004.
- [99] Dirk Taillaert, Frederik Van Laere, Melanie Ayre, Wim Bogaerts, Dries Van Thourhout, Peter Bienstman, and Roel Baets. Grating couplers for coupling between optical fibers and nanophotonic waveguides. *Japanese Journal of Applied Physics, Part 1: Regular Papers and Short Notes and Review Papers*, 45(8 A):6071–6077, 2006.
- [100] Roman Holly and Kurt Hingerl. Fabrication of silicon vertical taper structures using KOH anisotropic etching. *Microelectronic Engineering*, 83(4-9 SPEC. ISS.):1430–1433, 2006.

- [101] Thorsten Wahlbrink, Wan Shao Tsai, Michael Waldow, Michael Först, Jens Bolten, Thomas Mollenhauer, and Heinrich Kurz. Fabrication of high efficiency SOI taper structures. *Microelectronic Engineering*, 86(4-6):1117–1119, 2009.
- [102] Kai Ning Ku and Ming Chang M Lee. Wide-band optical mode converters for coupling between fibers and silicon photonic wires with large misalignment tolerance. *Journal of Lightwave Technology*, 31(10):1616–1620, 2013.
- [103] Minhao Pu, Liu Liu, Haiyan Ou, Kresten Yvind, and Jørn M. Hvam. Ultra-low-loss inverted taper coupler for silicon-on-insulator ridge waveguide. *Optics Communications*, 283(19):3678–3682, 2010.
- [104] Francesco Dell’Olio and Vittorio M. N. Passaro. Optical sensing by optimized silicon slot waveguides. *Opt. Express*, 15(8):4977–4993, Apr 2007. doi: 10.1364/OE.15.004977.
- [105] B. Troia, V. M. N. Passaro, and F. De Leonardis. High performance optical sensing in group iv slot optical waveguides at $2.883 \mu\text{m}$. pages 778–781, Nov 2011. doi: 10.1109/TELFOR.2011.6143660.
- [106] Zhechao Wang, Ning Zhu, Yongbo Tang, Lech Wosinski, Daoxin Dai, and Sailing He. Ultracompact low-loss coupler between strip and slot waveguides. *Optics letters*, 34(10):1498–1500, 2009. doi: 10.1364/OL.34.001498.
- [107] P Cheben, P J Bock, R Halir, J Lapointe, S Janz, a Dela, J Fe, B Lamontagne, and R Ma. Refractive Index Engineering With Subwavelength Gratings in Silicon Refractive Index Engineering With Subwavelength Gratings in Silicon. *IEEE Photonics Journal*, 3(3), 2011. doi: 10.1109/JPHOT.2011.2139198.
- [108] Valentina Donzella, Ahmed Sherwali, Jonas Flueckiger, Sahba Talebi Fard, Samantha M. Grist, and Lukas Chrostowski. Sub-wavelength grating components for integrated optics applications on SOI chips. *Optics Express*, 22(17):21037, 2014. doi: 10.1364/OE.22.021037.
- [109] J Gonzalo Wangüemert-pérez, Pavel Cheben, Alejandro Ortega-mo nux, Carlos Alonso-ramos, Diego Pérez-galacho, Robert Halir, Iñigo Molina-fernández, Dan-xia Xu, and Jens H Schmid. Evanescent field waveguide sensing with subwavelength grating structures in silicon-on-insulator. *Optics Letter*, 39(15):4442–4445, 2014. doi: 10.1364/OL.39.004442.

- [110] Xu Wang, Yun Wang, Jonas Flueckiger, Richard Bojko, Amy Liu, Adam Reid, James Pond, Nicolas a F Jaeger, and Lukas Chrostowski. Precise control of the coupling coefficient through destructive interference in silicon waveguide Bragg gratings. *Optics letters*, 39(19):5519–22, 2014.
- [111] Pavel Cheben, Przemek J Bock, Jens H Schmid, Jean Lapointe, Siegfried Janz, Dan-Xia Xu, Adam Densmore, André Delâge, Boris Lamontagne, and Trevor J Hall. Refractive index engineering with subwavelength gratings for efficient microphotonic couplers and planar waveguide multiplexers. *Optics letters*, 35(15):2526–2528, 2010. doi: 10.1364/OL.35.002526.
- [112] Lumerical Mode. URL <https://www.lumerical.com/tcad-products/mode/>.
- [113] Arman B. Fallahkhair, Kai S. Li, and Thomas E. Murphy. Vector finite difference modesolver for anisotropic dielectric waveguides. *Journal of Lightwave Technology*, 26(11):1423–1431, 2008. ISSN 07338724. doi: 10.1109/JLT.2008.923643.
- [114] C. Batten, A. Joshi, J. Orcutt, C. Holzwarth, M. Popovic, J. Hoyt, F. Kartner, R. Ram, V. Stojanovic, and K. Asanovic. Building manycore processor-to-dram networks with monolithic cmos silicon photonics. *IEEE Micro*, PP (99):1–1, 2016. ISSN 0272-1732. doi: 10.1109/MM.2009.51.
- [115] J. Chan, G. Hendry, A. Biberman, and K. Bergman. Architectural design exploration of chip-scale photonic interconnection networks using physical-layer analysis. In *2010 Conference on Optical Fiber Communication (OFC/NFOEC), collocated National Fiber Optic Engineers Conference*, pages 1–3, March 2010. doi: 10.1109/JLT.2010.2044231.
- [116] Shiyang Zhu, G. Q. Lo, and D. L. Kwong. Low-loss amorphous silicon wire waveguide for integrated photonics: effect of fabrication process and the thermal stability. *Opt. Express*, 18(24):25283–25291, Nov 2010. doi: 10.1364/OE.18.025283.
- [117] Timo Lipka, Melanie Kiepsch, Hoc Khiem Trieu, and Jörg Müller. Hydrogenated amorphous silicon photonic device trimming by uv-irradiation. *Opt. Express*, 22(10):12122–12132, May 2014. doi: 10.1364/OE.22.012122.
- [118] Taha M. Ben Masaud, Antulio Tarazona, Ehsan Jaberansary, Xia Chen, Graham T. Reed, Goran Z. Mashanovich, and H. M. H. Chong. Hot-wire

- polysilicon waveguides with low deposition temperature. *Opt. Lett.*, 38(20): 4030–4032, Oct 2013. doi: 10.1364/OL.38.004030.
- [119] SPTS HF release tool. URL <http://www.spts.com/Products/hf-release-etch/uEtch>.
- [120] D T H Tan, K Ikeda, R E Saperstein, B Slutsky, and Y Fainman. Chip-scale dispersion engineering using chirped vertical gratings. *Optics letters*, 33(24): 3013–3015, 2008.
- [121] Yannick de Koninck, Fabrice Raineri, Alexandre Bazin, Rama Raj, Gunther Roelkens, and Roel Baets. Experimental demonstration of a hybrid III-V-on-silicon microlaser based on resonant grating cavity mirrors. *Optics letters*, 38(14):2496–8, 2013.
- [122] Shahram Keyvaninia, Gunther Roelkens, Dries Van Thourhout, Christophe Jany, Marco Lamponi, Alban Le Liepvre, Francois Lelarge, Dalila Make, Guang-Hua Duan, Damien Bordel, and Jean-Marc Fedeli. Demonstration of a heterogeneously integrated III-V/SOI single wavelength tunable laser. *Optics Express*, 21(3):3784–92, 2013.
- [123] Chaotan Sima, J.C. Gates, B.D. Snow, H.L. Rogers, C. Holmes, M.N. Zervas, and P.G.R. Smith. Simple planar Bragg grating devices for photonic Hilbert transform. 012089, 2010.
- [124] L M Rivas, M J Strain, D Duchesne, a Carballar, M Sorel, R Morandotti, and J Azana. Picosecond linear optical pulse shapers based on integrated waveguide Bragg gratings. *Optics Letters*, 33(21):2425–2427, 2008.
- [125] M J Collins, C Xiong, I H Rey, T D Vo, J He, S Shahnia, C Reardon, T F Krauss, M J Steel, A S Clark, and B J Eggleton. Integrated spatial multiplexing of heralded single-photon sources. *Nature communications*, 4 (May):2582, 2013.
- [126] S. Azzini, D. Grassani, M.J. Strain, M. Sorel, L.G. Helt, J.E. Sipe, M. Liscidini, M. Galli, and D Bajoni. Ultra-low power generation of twin photons in a compact silicon ring resonator. 20(21):325–331, 2012.
- [127] Jun Rong Ong, Ranjeet Kumar, and Shayan Mookherjea. Ultra-high-contrast and tunable-bandwidth filter using cascaded high-order silicon microring filters. *IEEE Photonics Technology Letters*, 25(16):1543–1546, 2013.

- [128] Jun Rong Ong, Ranjeet Kumar, and Shayan Mookherjea. Silicon microring-based wavelength converter with integrated pump and signal suppression. *Optics letters*, 39(15):4439–41, 2014.
- [129] M Yamada and K Sakuda. Analysis of almost-periodic distributed feedback slab waveguides via a fundamental matrix approach. *Applied optics*, 26(16):3474–3478, 1987.
- [130] M. Gnan, G. Bellanca, H. M H Chong, P. Bassi, and R. M. De La Rue. Modelling of photonic wire Bragg gratings. *Optical and Quantum Electronics*, 38 (1-3 SPEC. ISS.):133–148, 2006.
- [131] Michael J Strain, Stephen Thoms, Douglas S MacIntyre, and Marc Sorel. Multi-wavelength filters in silicon using superposition sidewall Bragg grating devices. *Optics letters*, 39(2):413–6, 2014.
- [132] Alexandre D Simard, Michael J Strain, Laura Meriggi, Marc Sorel, and Sophie LaRochelle. Bandpass integrated Bragg gratings in silicon-on-insulator with well-controlled amplitude and phase responses. *Optics letters*, 40(5):736–9, 2015.
- [133] Ivano Giunttoni, Andrzej Gajda, Michael Krause, Ralf Steingrüber, Jürgen Bruns, and Klaus Petermann. Tunable Bragg reflectors on silicon-on-insulator rib waveguides. *Optics express*, 17(21):18518–18524, 2009.
- [134] Giuseppe Coppola, Andrea Irace, Antonello Cutolo, and Mario Iodice. Effect of fabrication errors in channel waveguide bragg gratings. *Appl. Opt.*, 38(9):1752–1758, Mar 1999.
- [135] Michael J. Strain and Marc Sorel. Integrated chirped bragg gratings with control over complex reflectivity. volume 70, page 4244, 2009.
- [136] Michael John Strain and Marc Sorel. Design and fabrication of integrated chirped bragg gratings for on-chip dispersion control. *IEEE Journal of Quantum Electronics*, 46(5):774–782, 2010.
- [137] C. Klitis, G. Cantarella, M. J. Strain, and M. Sorel. Polarisation selective bragg filters on silicon-on-insulator. In *2015 11th Conference on Ph.D. Research in Microelectronics and Electronics (PRIME)*, pages 353–356, June 2015.

- [138] C. Klitis, G. Cantarella, M. J. Strain, and M. Sorel. Integrated te/tm grating filters with high extinction ratio. In *2016 Photonics North (PN)*, pages 1–1, May 2016.
- [139] Mateusz Piekarek, Damien Bonneau, Shigehito Miki, Taro Yamashita, Mikio Fujiwara, Masahide Sasaki, Hirotaka Terai, Michael G. Tanner, Chandra M. Natarajan, Robert H. Hadfield, Jeremy L. O’Brien, and Mark G. Thompson. High-extinction ratio integrated photonic filters for silicon quantum photonics. *Opt. Lett.*, 42(4):815–818, Feb 2017.
- [140] L. Allen, M. W. Beijersbergen, R. J. C. Spreeuw, and J. P. Woerdman. Orbital angular momentum of light and the transformation of laguerre-gaussian laser modes. *Phys. Rev. A*, 45:8185–8189, Jun 1992. doi: 10.1103/PhysRevA.45.8185.
- [141] David G Grier. A revolution in optical manipulation. *Nature*, 424(6950):810–816, 2003.
- [142] Severin Fürhapter, Alexander Jesacher, Stefan Bernet, and Monika Ritsch-Marte. Spiral interferometry. *Opt. Lett.*, 30(15):1953–1955, Aug 2005.
- [143] Graham Gibson, Johannes Courtial, Miles J. Padgett, Mikhail Vasnetsov, Valeriy Pas’ko, Stephen M. Barnett, and Sonja Franke-Arnold. Free-space information transfer using light beams carrying orbital angular momentum. *Opt. Express*, 12(22):5448–5456, Nov 2004. doi: 10.1364/OPEX.12.005448.
- [144] Alois Mair, Alipasha Vaziri, Gregor Weihs, and Anton Zeilinger. Entanglement of the orbital angular momentum states of photons. *Nature*, 412(6844):313–316, 2001. doi: 10.1038/35085529.
- [145] Gabriel Molina-Terriza, Juan P. Torres, and Lluís Torner. Twisted photons. *Nature Physics*, 3(5):305–310, 2007. doi: 10.1038/nphys607.
- [146] M.W. Beijersbergen, R.P.C. Coerwinkel, M. Kristensen, and J.P. Woerdman. Helical-wavefront laser beams produced with a spiral phaseplate. *Optics Communications*, 112(5):321–327, 1994.
- [147] Gabriel Biener, Avi Niv, Vladimir Kleiner, and Erez Hasman. Formation of helical beams by use of pancharatnam–berry phase optical elements. *Opt. Lett.*, 27(21):1875–1877, Nov 2002.

- [148] L. Marrucci, C. Manzo, and D. Paparo. Optical spin-to-orbital angular momentum conversion in inhomogeneous anisotropic media. *Phys. Rev. Lett.*, 96:163905, Apr 2006.
- [149] Nanfang Yu, Patrice Genevet, Mikhail A. Kats, Francesco Aieta, Jean-Philippe Tetienne, Federico Capasso, and Zeno Gaburro. Light propagation with phase discontinuities: Generalized laws of reflection and refraction. *Science*, 334(6054):333–337, 2011.
- [150] N. R. Heckenberg, R. McDuff, C. P. Smith, and A. G. White. Generation of optical phase singularities by computer-generated holograms. *Opt. Lett.*, 17(3):221–223, Feb 1992.
- [151] Xinlun Cai, Jianwei Wang, Michael J. Strain, Benjamin Johnson-Morris, Jiangbo Zhu, Marc Sorel, Jeremy L. O’Brien, Mark G. Thompson, and Siyuan Yu. Integrated compact optical vortex beam emitters. *Science*, 338(6105):363–366, 2012. doi: 10.1126/science.1226528.
- [152] N. K. Fontaine, C. R. Doerr, and L. L. Buhl. Efficient multiplexing and demultiplexing of free-space orbital angular momentum using photonic integrated circuits. In *OFC/NFOEC*, pages 1–3, March 2012.
- [153] P. Baues. Huygens’ principle in inhomogeneous, isotropic media and a general integral equation applicable to optical resonators. *Opto-electronics*, 1(1):37–44, Feb 1969. ISSN 1572-817X. doi: 10.1007/BF01476791.
- [154] Jeffrey B Driscoll, Xiaoping Liu, Saam Yasseri, Iwei Hsieh, Jerry I Dadap, and Richard M Osgood. Large longitudinal electric fields (E_z) in silicon nanowire waveguides. *Optics Express*, 17(4):2797–2804, 2009. doi: 10.1364/OE.17.002797.
- [155] Jiangbo Zhu, Xinlun Cai, Yujie Chen, and Siyuan Yu. Theoretical model for angular grating-based integrated optical vortex beam emitters. *Optics letters*, 38(8):1343–5, 2013. doi: 10.1364/OL.38.001343.
- [156] Rui Li, Xue Feng, Dengke Zhang, Kaiyu Cui, Fang Liu, and Yidong Huang. Radially Polarized Orbital Angular Momentum Beam Emitter Based on Shallow-Ridge Silicon Microring Cavity. *IEEE Photonics Journal*, 6(3), 2014. doi: 10.1109/JPHOT.2014.2321757.

- [157] Fabrizio Gambini, Philippe Velha, Claudio J. Oton, and Stefano Faralli. Orbital Angular Momentum Generation with Ultra-Compact Bragg-Assisted Silicon Microrings. *IEEE Photonics Technology Letters*, 28(21):2355–2358, 2016. doi: 10.1109/LPT.2016.2594030.
- [158] Katsunari Okamoto. *Fundamentals of Optical Waveguides*. 2006. ISBN 9780125250962. doi: 10.1016/B978-0-12-525096-2.X5000-4.
- [159] Emis. *Data Review Series no 4. Properties of Silicon*.
- [160] Geoffrey John Burrell and Ellis Brian. *Semiconductor opto-electronics*. 1973.
- [161] G T Reed, A G Rickman, B L Weiss, F Namavar, E Cortesi, and R A Soref. Optical characteristics of planar waveguides in simox structures. *MRS Proceedings*, 244, 1991. doi: 10.1557/PROC-244-387.
- [162] T. Feuchter and C. Thirstrup. High precision planar waveguide propagation loss measurement technique using a fabry-perot cavity. *IEEE Photonics Technology Letters*, 6(10):1244–1247, Oct 1994. ISSN 1041-1135. doi: 10.1109/68.329652.
- [163] Daniel Hofstetter and Robert L. Thornton. Theory of loss measurements of fabry-perot resonators by fourier analysis of the transmission spectra. *Opt. Lett.*, 22(24):1831–1833, Dec 1997. doi: 10.1364/OL.22.001831.
- [164] Lumerical. URL <https://www.oxford-instruments.com/>.
- [165] Synopsys. URL <https://optics.synopsys.com/rsoft/rssoft-passive-device-beamprop.html>.
- [166] Comsol. URL <https://www.comsol.com/>.
- [167] Zhaoming Zhu and Thomas G. Brown. Full-vectorial finite-difference analysis of microstructured optical fibers. *Opt. Express*, 10(17):853–864, Aug 2002.
- [168] MathWorks code by Thomas Murphy. URL <http://uk.mathworks.com/matlabcentral/fileexchange/12734-waveguide-mode-solver>.
- [169] R. Pregla, W. von Reden, H. J. W. M. Hoekstra, and H. V. Baghdasaryan. *Beam propagation methods*, pages 35–65. Springer Berlin Heidelberg, Berlin, Heidelberg, 1999. ISBN 978-3-642-59889-0. doi: 10.1007/978-3-642-59889-0_2.

- [170] Dennis M Sullivan. *Electromagnetic Simulation Using the FDTD Method*, 2000.
- [171] Allen Taflove and Susan C. Hagness. *Computational Electrodynamics: The Finite-Difference Time-Domain Method*, Third Edition, 2005.
- [172] Stephen D. Gedney. *Introduction to the Finite-Difference Time-Domain (FDTD) Method for Electromagnetics*, volume 6. 2011. ISBN 9781608455225. doi: 10.2200/S00316ED1V01Y201012CEM027.
- [173] Lumerical FDTD. URL <https://www.lumerical.com/tcad-products/fdtd/>.
- [174] Manfred Hammer and Olena V. Ivanova. Effective index approximations of photonic crystal slabs: a 2-to-1-d assessment. *Optical and Quantum Electronics*, 41(4):267–283, 2009. ISSN 1572-817X. doi: 10.1007/s11082-009-9349-3.
- [175] Lumerical varFDTD white paper. URL https://www.lumerical.com/support/whitepaper/2.5d_fDTD_propagation_method.html.
- [176] Dominic F G Gallagher and Thomas P Felici. Eigenmode Expansion Methods for Simulation of Optical Propagation in Photonics -Pros and Cons. *Proceedings of SPIE*, 4987:69–82, 2003.
- [177] Comsol The Finite Element Method. URL <https://www.comsol.com/multiphysics/finite-element-method>.
- [178] Jean-Pierre Berenger. *Perfectly Matched Layer (PML) for Computational Electromagnetics*. Morgan and Claypool, 2007. ISBN 9781598290837. doi: 10.2200/S00030ED1V01Y200605CEM008.
- [179] Lumerical Symmetric and anti-symmetric BCs. URL https://kb.lumerical.com/en/ref_sim_obj_symmetric_anti-symmetric.html.
- [180] M. K. Smit, E. C. M. Pennings, and H. Blok. A normalized approach to the design of low-loss optical waveguide bends. *Journal of Lightwave Technology*, 11(11):1737–1742, Nov 1993. ISSN 0733-8724. doi: 10.1109/50.251169.
- [181] L. H. Spiekman, Y. S. Oei, E. G. Metaal, F. H. Groen, P. Demeester, and M. K. Smit. Ultrasmall waveguide bends: the corner mirrors of the future?

- IEE Proceedings - Optoelectronics*, 142(1):61–65, Feb 1995. ISSN 1350-2433. doi: 10.1049/ip-opt:19951664.
- [182] Sangin Kim and A. Gopinath. Vector analysis of optical dielectric waveguide bends using finite-difference method. *Journal of Lightwave Technology*, 14(9):2085–2092, Sep 1996. ISSN 0733-8724.
- [183] W. Bogaerts and S. K. Selvaraja. Compact single-mode silicon hybrid rib/strip waveguide with adiabatic bends. *IEEE Photonics Journal*, 3(3):422–432, 2011. ISSN 19430655. doi: 10.1109/JPHOT.2011.2142931.
- [184] Huynh Ngoc Phien and Nattawit Dejdumrong. Efficient algorithms for Bézier curves. *Computer Aided Geometric Design*, 17(3):247–250, 2000. ISSN 01678396. doi: 10.1016/S0167-8396(99)00048-5.
- [185] J. Schilling R.B. Wehrspohn, C. Schriever. Inhomogeneous strain in Silicon Photonics. *ECS Transactions*, 61(5):161–173, 2014.
- [186] Clemens Schriever, Federica Bianco, Massimo Cazzanelli, Mher Ghulinyan, Christian Eisenschmidt, Johannes de Boor, Alexander Schmid, Johannes Heitmann, Lorenzo Pavesi, and Jörg Schilling. Second-Order Optical Non-linearity in Silicon Waveguides: Inhomogeneous Stress and Interfaces. *Advanced Optical Materials*, 3(1):129–136, 2015. doi: 10.1002/adom.201400370.
- [187] Antonio Samarelli. Micro ring resonators in silicon-on-insulator.
- [188] Rune S Jacobsen, Karin N Andersen, Peter I Borel, Jacob Fage-Pedersen, Lars H Frandsen, Ole Hansen, Martin Kristensen, Andrei V Lavrinenko, Gaid Moulin, Haiyan Ou, Christophe Peucheret, Beáta Zsigri, and Anders Bjarklev. Strained silicon as a new electro-optic material. *Nature*, 441(7090):199–202, 2006. doi: 10.1038/nature04706.
- [189] Bartos Chmielak, Michael Waldow, Christopher Matheisen, Christian Ripperda, Jens Bolten, Thorsten Wahlbrink, Michael Nagel, Florian Merget, and Heinrich Kurz. Pockels effect based fully integrated, strained silicon electro-optic modulator. *Optics Express*, 19(18):17212, 2011. doi: 10.1364/OE.19.017212.
- [190] Bartos Chmielak, Christopher Matheisen, and Christian Ripperda. Investigation of local strain distribution and linear electro-optic effect in

- strained silicon waveguides. *Optics Express*, 21(21):25324–25332, 2013. doi: 10.1364/OE.21.025324.
- [191] Pedro Damas, Xavier Le Roux, David Le Bourdais, Eric Cassan, Delphine Marris-Morini, Nicolas Izard, Thomas Maroutian, Philippe Lecoer, and Laurent Vivien. Wavelength dependence of Pockels effect in strained silicon waveguides. *Optics Express*, 22(18):22095, 2014. doi: 10.1364/OE.22.022095.
- [192] Q. Lin, Oskar J. Painter, and Govind P. Agrawal. Nonlinear optical phenomena in silicon waveguides: Modeling and applications. *Opt. Express*, 15(25):16604–16644, Dec 2007. doi: 10.1364/OE.15.016604.
- [193] R. M. Osgood, N. C. Panoiu, J. I. Dadap, Xiaoping Liu, Xiaogang Chen, I-Wei Hsieh, E. Dulkeith, W. M.J. Green, and Y. A. Vlasov. Engineering nonlinearities in nanoscale optical systems: physics and applications in dispersion-engineered silicon nanophotonic wires. *Adv. Opt. Photon.*, 1(1): 162–235, Jan 2009. doi: 10.1364/AOP.1.000162.
- [194] R. W. Boyd. *Nonlinear Optics*. Academic Press, 2003.